Antimony-Based Low-Noise Avalanche Photodiodes

A Dissertation

Presented to

the Faculty of the School of Engineering and Applied Science

University of Virginia

In Partial Fulfillment of

the Requirements for the Degree of

Doctor of Philosophy

By

Bingtian Guo

May 2024

APPROVAL SHEET

This Dissertation
is submitted in partial fulfillment of the requirements
for the degree of
Doctor of Philosophy

Author Signature: Bingtian Guo

This dissertation has been read and approved by the examining committee:

Advisor: Joe C. Campbell

Committee Chair: Andreas Beling

Committee Member: Steven M. Bowers

Committee Member: Kyusang Lee

Committee Member: Stephen J. McDonnell

Accepted for the School of Engineering and Applied Science:

Jennifer L. West, School of Engineering and Applied Science

May 2024

This dissertation is dedicated to my parents.

Contents

Acknowledgment

When I reached this critical point and looked back on my PhD journey, I realized how lucky I am to receive such generous support from so many people along the way. Foremost among them is undoubtedly my advisor, Prof. Joe C. Campbell. I would like to extend my deepest gratitude for his valuable guidance and continuous support on my PhD study. The lessons I have learned from him extend beyond research knowledge, encompassing invaluable life insights that will shape my entire life. I vividly recall numerous treasured moments with him which have brightened my PhD experience, moments I believe will remain with me always. I am deeply thankful to him for providing me with the opportunity to be a part of the JCC group!

I am so grateful to all our group members for their help. In particular, I would like to thank Dr. Keye Sun for his encouragement along the journey and valuable guidance on my research. I would like to thank Dr. Andrew H. Jones for his mentorship and selfless support in my research work. I would like to thank Dr. Dekang Chen, Junwu Bai, Dr. Xiangwen Guo, and Dr. Adam A. Dadey for their fruitful discussion and valuable help in the lab. The numerous support from the JCC group makes it possible to get through many challenges.

I want to express my gratitude to our collaborators at the Ohio State University, University of California, Los Angeles, and the University of Sheffield. Specifically, I would like to thank Prof. Sanjay Krishna for his leadership in managing the LEAPS project. I would like to thank Dr. Baolai Liang for his guidance on my research and growth of various samples. I would like to thank Dr. Xiao Jin for his discussion and collaboration.

I would like to thank my committee members, Prof. Andreas Beling, Prof. Kyusang Lee, Prof. Steven M. Bowers, and Prof. Stephen J. McDonnell for their time and help. I greatly appreciate their feedback on my PhD work.

Last but not the least, I would like to thank my parents and Kuan Liu for their unwavering encouragement and companionship. Their support has always been a source of strength for me. I love you all forever.

Bingtian Guo

University of Virginia

Charlottesville, VA, USA

May 2024

Abstract

High-sensitivity avalanche photodiodes (APDs) are used to detect weak optical signals in a wide range of research, commercial, and military applications, including telecommunications, data centers, spectroscopy, imaging, light detection and ranging (LiDAR), medical diagnostics, and quantum computing. A widely used APD structure has separate absorption, charge, and multiplication (SACM) sections, where two different materials are employed as the multiplier and the absorber, respectively. The advantages of these two materials can be combined. This dissertation focuses on three research areas: (1) investigation of multiplier material with low excess noise and strong temperature stability, (2) investigation of absorber material with improved optical characteristics, and (3) investigation of SACM APDs incorporating the low-noise multiplier and the absorber that operate in the infrared spectral region.

Compared to conventional p-i-n photodiodes, APDs exhibit higher photodetection sensitivity due to their internal gain originating from serial impact ionization. However, the gain, M, is created by impact ionization which is a random process. This gives rise to detector noise expressed as an excess noise factor, $F(M)$, which can degrade the signal-to-noise ratio and gain-bandwidth product. Therefore, a multiplier with low excess noise is always preferable. This dissertation demonstrates $Al_{0.85}Ga_{0.15}As_{0.56}Sb_{0.44}$ (AlGaAsSb) and $Al_{0.79}In_{0.21}As_{0.74}Sb_{0.26}$ (AlInAsSb) materials lattice matched to InP which exhibit low excess noise, comparable to that of silicon (Si) ($k \sim 0.01$). Subsequently, the optical constants of AlGaAsSb and AlInAsSb were extracted via variable-angle spectroscopic ellipsometry, and the impact ionization coefficients of AlGaAsSb were determined in a wide electrical field range via a series of wavelength-dependent multiplication gain curves. The extracted material parameters are necessary for future simulations of APDs using Sb-based multipliers. Additionally, these Sb-based material systems have exhibited significantly enhanced

temperature stability of avalanche breakdown compared to commercially available Si-, InAlAs-, and InP-based APDs, reducing the cost and complexity of optical receiver circuits.

For APDs used in the short-wavelength infrared (SWIR) spectral region (900 – 1700 nm), Si and InGaAs are widely used as the absorption materials with the cut-off wavelengths of 1100 nm and 1680 nm, respectively. However, recent advances in applications such as imaging, optical communications, and LiDAR have created a need for photodetectors that operate in the extended SWIR spectral region (1700 – 2500 nm), which is beyond the cutoff wavelength of random alloy (RA) InGaAs. In this dissertation, a series of digital alloy (DA)-grown InAs/GaAs short-period superlattices were investigated to extend the absorption spectral range. The photoluminescence peak can be effectively shifted from 1690 nm (0.734 eV) for conventional RA InGaAs to 1950 nm (0.636 eV) for eight monolayer DA InGaAs at room temperature. The optical constants of DA InGaAs have been extracted via ellipsometry technique, showing absorption coefficients of 398 cm^{-1}, 831 cm^{-1}, and 1230 cm^{-1} at 2 μm for 6, 8, and 10 monolayer DA InGaAs. As the period thickness increases for DA InGaAs, a redshift at the absorption edge can be observed. These results pave the way for the future utilization of the DA-grown InAs/GaAs short-period superlattices as a promising absorption material choice to extend the photodetector response beyond the cutoff wavelength of RA InGaAs.

After the investigation of multiplication and absorption materials, this dissertation reports three Sb-based SACM APDs on semi-insulating InP substrates, InGaAs/AlInAsSb APDs, GaAsSb/AlGaAsSb APDs, and DA InGaAs/AlGaAsSb APDs. These APDs exhibit low excess noise and weak temperature dependence of avalanche breakdown due to the Sb-based multiplication regions. Using semi-insulating InP substrates removes the limitation on high-speed operation observed with Sb-based APDs on doped GaSb substrates. The InGaAs/AlInAsSb APDs

and GaAsSb/AlGaAsSb APDs have conventional RA absorbers that operate in the SWIR spectral region. The absorber in the DA InGaAs/AlGaAsSb APDs can extend the operating wavelength into the extended SWIR spectral region. These SACM APDs exhibit excellent electrical and optical properties, making them ideal for use in high-sensitivity optical receivers in a wide range of applications within the SWIR and extended SWIR spectral regions.

List of Figures

List of Tables

1. Introduction

1.1. Motivation

Highly sensitive photodetectors are key components in commercial, research, and military applications ranging from thermal imaging, optical communication, biological and chemical agent detection, and light detection and ranging (LiDAR) [1-4]. Avalanche photodiodes (APDs) have been widely deployed in these applications because the low-noise internal gain achieved through impact ionization provides the potential for higher signal-to-noise performance than conventional p-i-n photodiodes. Silicon (Si) APDs have been widely used due to their extremely low excess noise, low cost, and high material quality, but their operation is limited to wavelengths below 1.1 μm. For APDs working at longer wavelengths, $In_{0.53}Ga_{0.47}As/In_{0.52}Al_{0.48}As$ (InGaAs/InAlAs) APDs and InGaAs/InP APDs are commercially available, but their excess noise is much higher than Si APDs, limiting the photodetection sensitivity. Therefore, it is useful to investigate low-noise APDs of different material systems operating at infrared spectral regions.

Many applications use APDs with the separate absorption, charge, and multiplication (SACM) structure. These APDs employ two different materials as the multiplier and the absorber to combine their advantageous electrical and optical properties. The electric field in the multiplier and the absorber is adjusted appropriately in this structure via a charge layer. To obtain low-noise APDs operating at infrared spectral region, the research can be divided into three parts, including (1) the investigation of multiplier materials with low excess noise, low dark current, and strong temperature stability of multiplication gain based on a series of optical and electrical characterizations; (2) the investigation of absorbers capable of absorbing light at infrared spectral region; and (3) the investigation of SACM APDs incorporating the advantages of studied multipliers and absorbers.

Starting from the investigation of the multiplier, APDs are advantageous due to the internal multiplication gain. However, the maximum useful multiplication gain is limited by two factors. First, the stochastic nature of the impact ionization process is a noise source that increases with increasing gain [5]. The figure of merit for this noise is the excess noise factor, F(M), which is treated as a multiplicative of the shot noise. The shot noise current is expressed by [6, 7]

$$\left\langle i_{shot}^2 \right\rangle = 2q\left(I_{photo} + I_{dark}\right)\left\langle M \right\rangle^2 F\left(M\right)\Delta f, \tag{1.1}$$

where q is the electric charge, I_{photo} is the photocurrent, I_{dark} is the dark current, $<M>$ is the average gain, and Δf is the bandwidth. The excess noise factor can be expressed by the local field model as [5]

$$F\left(M\right) = k\left\langle M \right\rangle + \left(1-k\right)\left(2 - \frac{1}{\left\langle M \right\rangle}\right), \tag{1.2}$$

where k is the ratio of the impact ionization coefficients of holes (β) to electrons (α) for the electron-initiated impact ionization process. They represent the mean rate of ionization per unit distance and are equal to the inverse of the mean distance a carrier travels before ionizing. The excess noise factor increases with gain increasing, but the rate of increase is lower for a material with a lower k-value. Second, the avalanche build-up time affects the gain-bandwidth product, which can limit the response time at high gain [8]. Due to these two limiting mechanisms, a lower k-value is always desirable to provide lower excess noise (i.e., higher signal-to-noise ratio) and higher response speed.

There are three approaches to reducing the excess noise factor: scaling the thickness of the multiplication region to take advantage of the non-local characteristic of impact ionization [9], impact ionization engineering by employing heterojunctions [10], and selecting semiconductor

materials with favorable impact ionization coefficients [11]. For most applications, selecting semiconductor materials with preferable parameters wins due to their simpler device structures.

There have been several widely investigated semiconductor materials with low excess noise. In addition to Si with a *k* value of ~ 0.01 [12, 13], $Hg_{0.7}Cd_{0.3}Te$ on CdZnTe substrates [14], InAs on InAs substrates [15], and $Al_xIn_{1-x}As_ySb_{1-y}$ on GaSb substrates [16] have shown extremely low excess noise. $Hg_{0.7}Cd_{0.3}Te$ and InAs show *k* values equal to 0, but the cryogenic temperature is required to solve the issue of inherent high dark current originating from the narrow bandgap, making them not good multiplier options for the commercial applications that cannot accommodate cryogenic cooling. Recently, $Al_xIn_{1-x}As_ySb_{1-y}$ grown as digital alloys (DAs) with x = 0.5, 0.6, 0.7, and 0.8 on GaSb substrates were reported with *k* values as low as 0.01. There are many advantages, including tunable cut-off wavelengths with different Al concentrations, low excess noise comparable to that of Si, high gain, and low dark current at room temperature [17]. However, the employed GaSb substrates have relatively high doping, limiting the high-speed operation [18]. Replacing GaSb with a semi-insulating substrate is advantageous while keeping other properties unchanged for the $Al_xIn_{1-x}As_ySb_{1-y}$ material system.

In this dissertation, I have investigated the antimony-based (Sb-based) material system but on a different substrate, InP. The semi-insulating InP substrate is chosen for the following reasons. InP substrates are more cost-effective, and the size can be 6” large, facilitating the applications requiring the photodetector array. Furthermore, the substrate plays an important role in the absorber options for SACM APDs. Compared to other substrates, high-quality absorbers have been investigated more on InP substrates such as InGaAs and GaAsSb for 1550-nm applications and InGaAs/GaAsSb superlattices for 2.0-μm applications. If multiplier materials on InP exhibit low excess noise, low dark current, and weak temperature dependence of avalanche breakdown, it will

be much easier to incorporate such multipliers with the mature absorbers in SACM APDs on InP substrates.

For the investigation of absorbers on InP substrates, InGaAs is a commercially mature absorber with a cut-off wavelength at 1680 nm used in photodetectors working at the short-wavelength infrared (SWIR) spectral region (900 – 1700 nm). Emerging research and commercial interests such as imaging [19], optical communications [20], and LiDAR [17] at the extended SWIR spectral region (1700 – 2500 nm) have created a need for investigations of the absorbers working at this region. Traditional InGaAs is grown by the random alloy (RA) growth technique with a bandgap of 0.74 eV. If the digital alloy growth technique is employed for the InGaAs material system, the bandgap of DA InGaAs can be tuned accordingly by changing the period thickness. The wider absorption window makes DA InGaAs a promising absorber candidate operating at the extended SWIR spectrum. In this dissertation, I have demonstrated DA InGaAs with tunable bandgap and extracted the corresponding optical constants.

For the investigation of SACM APDs working at the SWIR and extended SWIR spectral regions, the Sb-based materials, including $Al_xIn_{1-x}As_ySb_{1-y}$ and $Al_xGa_{1-x}As_ySb_{1-y}$ lattice matched to InP substrates, were employed as the multiplier to reduce the excess noise and temperature sensitivity, and RA/DA InGaAs and GaAsSb were used as the absorber for the SWIR and extended SWIR photodetection. The combined benefits of the multiplier and the absorber make these APDs promising candidates for photodetection at the SWIR and extended spectral regions under varying ambient conditions compared to other commercially available APDs.

1.2. Dissertation organization

This work focuses on low-noise Sb-based APDs, including investigations of low-noise multipliers, absorbers working at the extended SWIR spectral region, and Sb-based SACM APDs.

Chapter 1 describes the motivation behind the exploration of low-noise APDs. Chapter 2 introduces the fundamental concepts, characterization methods, and fabrication process for APDs. Chapter 3 shows the investigation of Sb-based multipliers, including demonstrating low-noise characteristics, extracting optical constants and impact ionization coefficients, and demonstrating weak temperature dependence of avalanche breakdown. Chapter 4 shows the investigation of the DA InGaAs absorber, including the demonstration of tunable bandgap at the extended SWIR spectral region and the extraction of optical constants. Chapter 5 presents the investigation of RA InGaAs/AlInAsSb, GaAsSb/AlGaAsSb, and DA InGaAs/AlGaAsSb SACM APDs. Chapter 6 describes the future work.

2. Fundamentals of Avalanche Photodiodes

2.1. Dark current

Dark current originates from the thermally generated electron-hole pairs, and it includes the components of the temperature-dependent diffusion current and the temperature-independent trap-assisted tunneling current. The temperature-dependent dark current investigation is usually used to determine whether the tunneling issue exists in the APDs. Dark current is measured under dark conditions with an HP 4145 semiconductor parameter analyzer or a Keithley 2400 source meter.

2.2. Multiplication gain

The multiplication gain originates from the serial impact ionization process, and it can be calculated from the photocurrent curve for p^+-i-n^+ APDs. The multiplication gain is calculated by

$$M(V)=\frac{I_{\text{photo}}(V)}{I_{photo}(V_0)}=\frac{I_{total}(V)-I_{dark}(V)}{I_{total}(V_0)-I_{dark}(V_0)}, \tag{2.1}$$

where V_0 is the bias at the unity gain point, V is the measured voltage, and I_{photo}, I_{dark}, and I_{total} represent the photocurrent, dark current, and total current. Additionally, the multiplication gain of an ideal p^+-i-n^+ APD can be calculated theoretically based on the impact ionization coefficients and the absorption profiles. For the simplest pure electron and hole injection profiles, the multiplication gain can be calculated by [21]

$$M_e=\frac{1}{1-\int_0^w \alpha \exp\left[-\int_0^x(\alpha-\beta)dx'\right]dx}, \tag{2.2}$$

$$M_h=\frac{1}{1-\int_0^w \beta \exp\left[\int_x^w(\alpha-\beta)dx'\right]dx}, \tag{2.3}$$

where M_e is the gain under pure electron injection profile, M_h is the gain under pure hole injection profile, and w is the depletion width. For the multiplication gain determination of SACM APDs,

the unity gain point cannot be easily identified, and the gain is determined by fitting the measured excess noise to the measured photocurrent [22].

2.3. Excess noise

The excess noise originates from the random nature of the serial impact ionizations, and it is evaluated by the excess noise factor, as expressed by Eq. (1.2). As for the excess noise measurement, APDs are DC-biased through a bias tee by a Keithley 2400 source meter, and a temperature-stabilized laser coupled into a lensed fiber is used to illuminate APDs. An Agilent N8973A noise figure analyzer measures the AC component of the output current through the bias tee. The background noise is removed using a calibrated Agilent 346A noise source for system calibration.

2.4. Responsivity and quantum efficiency

The responsivity describes the effectiveness of the photodiode in converting the incident light into the photocurrent, calculated by

$$R = \frac{I_{photo}\left(V_0\right)}{P_{incident}}, \tag{2.4}$$

where $I_{photo}(V_0)$ is the photocurrent at the unity gain point, and $P_{incident}$ is the incident optical power. Quantum efficiency is also used to describe the photoresponse efficiency of the photodiode and the probability of converting the incident photons into electrons. The quantum efficiency includes external quantum efficiency (EQE) and internal quantum efficiency (IQE). EQE can be calculated by

$$EQE = \frac{N_{e-h}}{N_{photon}} = \frac{I_{photo}\left(V_0\right)/q}{P_{incident}/h\nu} = R\frac{h\nu}{q}, \tag{2.5}$$

where $N_{e\text{-}h}$ and N_{photon} are the number of photo-generated electron-hole pairs and incident photons, h is the Planck constant, v is the light frequency, and q is the charge of an electron. EQE can also be calculated by

$$EQE = (1-\Gamma)(1-\eta)\left(1-e^{-\alpha d}\right), \tag{2.6}$$

where Γ is the surface reflectivity, η represents the loss of the photo-generated carriers inside the photodiodes, α is the absorption coefficient, and d is the absorber thickness. Furthermore, IQE can be calculated by

$$IQE = \frac{N_{e-h}}{N_{in-photon}} = \left(1-e^{-\alpha d}\right), \tag{2.7}$$

where $N_{in\text{-}photon}$ is the number of photons entering the semiconductor. To improve the EQE, the anti-reflection coating or the photo-trapping structure [23, 24] can be implemented.

As for the EQE measurement, a stabilized tungsten light source and a monochromator are used to illuminate the devices normally, and the photocurrents are measured by a lock-in amplifier for investigated APDs and a calibrated Si (or strained-layer InGaAs) photodiode with known responsivity/EQE. The EQE of investigated APDs can be calculated based on the EQE of the reference Si (or strained-layer InGaAs) photodiode.

2.5. Bandwidth

The bandwidth describes the operation speed of photodiodes, and the 3-dB bandwidth is defined as the frequency where the output RF power drops by 3 dB in comparison to the power at low frequency range. Considering the impedance matching condition without the loss resulting from the external microwave circuit, the bandwidth is limited by the electron/hole transit time (between the carrier generation stage and collection stage) and the resistance-capacitance (RC)

response time. These constraints give rise to two key parameters: transit-time-limited bandwidth (f_{tr}) and RC-limited bandwidth (f_{RC}).

As for the transit-time-limited bandwidth, the carrier transit time is primarily determined by the material-dependent drift velocity of electrons and holes and the thickness of the depletion region. The transit-time-limited bandwidth can be approximately calculated by [25]

$$f_{\mathrm{tr}} = \frac{3.5\bar{v}}{2\pi d}, \tag{2.8}$$

$$\bar{v} = \sqrt{2\left(\frac{1}{v_e^4} + \frac{1}{v_h^4}\right)^{-1}}, \tag{2.9}$$

where $\bar{v}$ is the effective average drift velocity, d is the depletion region thickness, v_e is the drift velocity of electrons, and v_h is the drift velocity of holes.

As for the RC-limited bandwidth, the RC response time is determined by the circuit parameters in the equivalent circuit model of a photodiode. Figure 2.1 shows the equivalent circuit model of a photodiode, where C_j, R_j, R_s, and R_L represent junction capacitance, junction resistance, series resistance, and load resistance (generally at 50 Ω). Based on the assumption that $R_j >> R_s + R_L$, the RC-limited bandwidth can be approximately calculated by

$$f_{\mathrm{RC}} = \frac{1}{2\pi C_j \left(R_s + R_L\right)}, \tag{2.10}$$

$$C_j = \frac{\varepsilon_0 \varepsilon_r S}{d}, \tag{2.11}$$

where ε_0 and ε_r are vacuum permittivity and relative permittivity (i.e., dielectric constant), S is the device area, and d is the depletion region thickness.

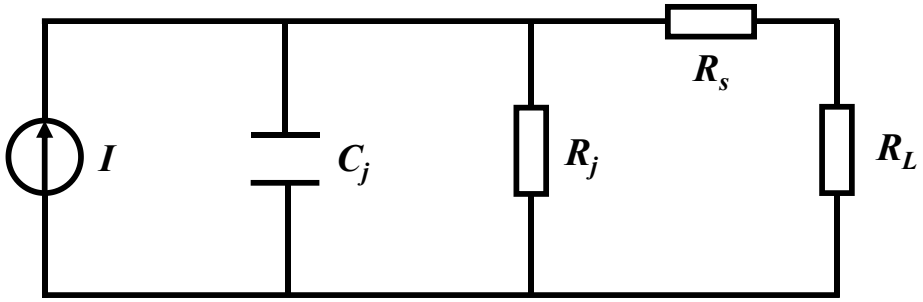

Figure 2.1. Fabrication flow of avalanche photodiodes.

Without considering the build-up time limitation for APDs, the 3-dB bandwidth at the unity gain point can be calculated by

$$f_{3dB} = \sqrt{\frac{1}{\frac{1}{f_{tr}^2} + \frac{1}{f_{RC}^2}}}. \tag{2.12}$$

To obtain a higher 3-dB bandwidth, there is a trade-off between transit-time-limited bandwidth and RC-limited bandwidth. A thinner depletion region decreases the transit time, leading to higher transit-time-limited bandwidth. However, a thinner depletion region increases the junction capacitance, leading to lower RC-limited bandwidth. Therefore, the balance between these two bandwidth limit mechanisms must be considered. Additionally, the responsivity (absorber thickness) plays an important role in the design consideration.

The setup for measuring bandwidth using the vector network analyzer (VNA) is illustrated in Fig. 2.2. The continuous-wave (CW) optical signal from a 1550-nm laser passes through a polarization controller (PC), and it is then externally modulated by a $LiNbO_3$ Mach-Zehnder modulator (MZM). The MZM is DC-biased at the quadrature point by a source meter, and a VNA is used to provide the RF signal for the MZM. The modulated optical signal is then focused on the investigated photodetectors via a lensed fiber. The photocurrent is collected through an RF ground-signal (GS) or ground-signal-ground (GSG) probe. The source meter reads the DC signal, and the

VNA reads the RF signal. After the system calibration, the *S*-parameters can be measured by the VNA. The measured transmission coefficient, S_{21}, is used to determine the 3-dB bandwidth, and the measured reflection coefficient, S_{11}, is used to determine the circuit parameters included in the equivalent circuit model. The VNA determines the maximum measurement bandwidth of this setup, and it is usually below 120 GHz. The widely reported heterodyne setup [26] could be used for higher bandwidth measurement.

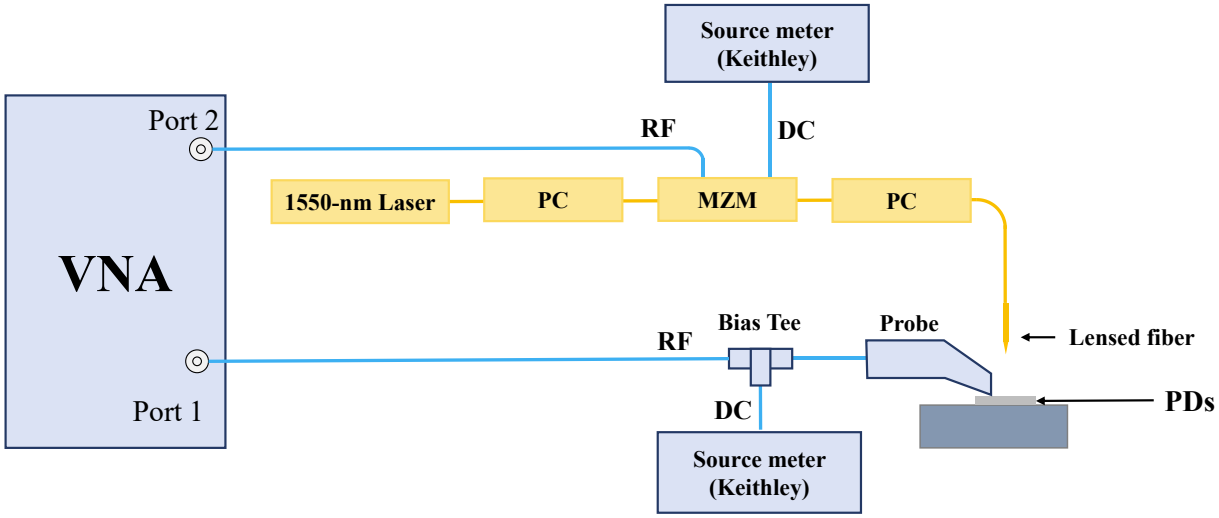

Figure 2.2. Setup for measuring bandwidth utilizing a vector network analyzer and a Mach-Zehnder modulator for external modulation of incident light.

2.6. Device fabrication

The fabrication flow is shown in Fig. 2.3. The circular mesas are defined by conventional photolithography, and the structures are formed via chemical etching. The solution of H_3PO_4, H_2O_2, and H_2O is used to etch InGaAs layers, and the solution of citric acid, H_3PO_4, H_2O_2, and H_2O is used to etch the other Al-containing layers. The Ti/Au contacts are then deposited on InGaAs contact layers via electron-beam evaporation, and the SU-8 is spun on the sidewall to suppress the surface leakage current. For high-speed photodiodes, a smaller device diameter is required to improve the RC-limited bandwidth, and the dry etch technique is utilized to prevent undercut

issues. Additionally, a 50-Ω coplanar waveguide (CPW) GSG pad is required for probing while keeping the impedance matching.

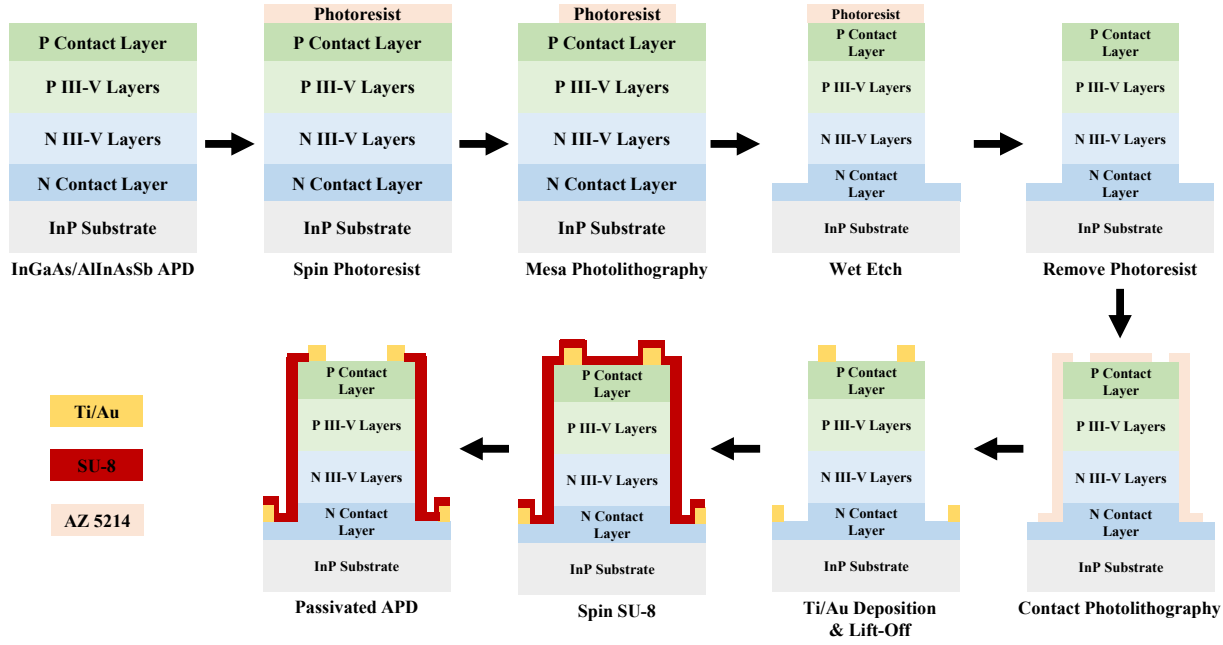

Figure 2.3. Process flow for the fabrication of avalanche photodiodes.

2.7. Digital alloy

The digital alloys (DAs) are essentially a short-period, multicomponent generalization of superlattices, where the superlattice period is reduced sufficiently that charge carrier wavefunctions extend over many periods. They can improve the performance of optoelectronic devices such as circumventing the limitations imposed by miscibility gaps [27, 28], engineering novel band structures [10, 17, 29, 30], and providing a new method to achieve bandgap tunability [31, 32].

The digital alloy growth technique is employed for the Sb-based quaternary material systems ($Al_xGa_{1-x}As_ySb_{1-y}$ and $Al_xIn_{1-x}As_ySb_{1-y}$), and one period of DA $Al_xGa_{1-x}As_ySb_{1-y}$ and $Al_xIn_{1-x}As_ySb_{1-y}$ is composed of binary or ternary materials. For the investigated DA $Al_{0.85}Ga_{0.15}As_{0.56}Sb_{0.44}$ on InP discussed in this dissertation, its growth was undertaken at a

temperature of 500 °C as a short-period (1.3 nm) superlattice with rapidly alternating layers of AlGaAs (0.17 nm) and AlGaSb (1.13 nm) to meet lattice matching conditions on the InP substrate. The investigated DA $Al_{0.7}In_{0.3}As_{0.79}Sb_{0.21}$ on InP discussed in Section 5.2 was grown in a ten monolayer (2.93 nm) period with alternating layers of AlAs, AlSb, and InAs. Additionally, the InGaAs material system can be grown as digital alloys to realize the bandgap tunability, and its growth was undertaken as a short-period superlattice (d ML) with rapidly alternating layers of GaAs (d ML × 47%) and InAs (d ML × 53%) in order to meet lattice matching conditions on the InP substrate.

3. Antimony-Based Multipliers

3.1. Low-noise $Al_{0.85}Ga_{0.15}As_{0.56}Sb_{0.44}$ and $Al_{0.79}In_{0.21}As_{0.74}Sb_{0.26}$ APDs

3.1.1. Motivation

Avalanche multiplication materials with lower *k* values are preferred in order to reduce the deleterious impact on signal-to-noise ratio and bandwidth that result when both electrons and holes make significant contributions to the gain [1]. As discussed in Chapter 1, although Si, $Hg_{0.7}Cd_{0.3}Te$, InAs, and $Al_xIn_{1-x}As_ySb_{1-y}$ lattice matched to GaSb exhibit low noise, there are some inherent limitations associated with these materials. In this dissertation, Sb-based material systems on semi-insulating InP substrates are the investigation focus.

Recently, DA $AlAs_{0.56}Sb_{0.44}$ (AlAsSb) APDs on InP substrate have been reported with a *k* value of 0.005 [33]. This is the first Sb-based multiplier on InP to have a *k* value comparable to that of Si, and this *k*-value is more than one order of magnitude lower than that of commercially available multiplier materials, InP ($k \sim 0.45$) and InAlAs ($k \sim 0.2$). However, AlAsSb APDs have oxidization issues due to the high Al content, leading to a high surface dark current [34]. To mitigate the oxidization issue, Ga was incorporated, resulting in the $Al_{0.85}Ga_{0.15}As_{0.56}Sb_{0.44}$ APDs [28, 34-38] studied in this dissertation.

Low-noise DA $Al_xIn_{1-x}As_ySb_{1-y}$ APDs on doped GaSb substrates has been well investigated, demonstrating excellent electrical properties. It is logical to explore this material system on semi-insulating InP substrate to remove the bandwidth limitation. However, the investigation of $Al_xIn_{1-x}As_ySb_{1-y}$ on InP has been limited by the complicated growth. Recently, $Al_xIn_{1-x}As_ySb_{1-y}$ was successfully grown as a random alloy on an InP substrate for its incorporation in a multijunction solar cell [39]. The improved growth techniques make the investigation of RA $Al_xIn_{1-x}As_ySb_{1-y}$ APDs on InP practical.

In this section, two Sb-based quaternary material systems, $Al_xIn_{1-x}As_ySb_{1-y}$ and $Al_xGa_{1-x}As_ySb_{1-y}$ lattice matched to InP substrate, are presented. The dark current, multiplication gain, and excess noise have been measured for $Al_{0.85}Ga_{0.15}As_{0.56}Sb_{0.44}$ (AlGaAsSb) and $Al_{0.79}In_{0.21}As_{0.74}Sb_{0.26}$ (AlInAsSb) APDs.

3.1.2. Results and discussion

Three wafers were grown as p^+-i-n^+ structures by molecular beam epitaxy (MBE). One of the AlGaAsSb wafers lattice matched to InP was grown as a digital alloy [28] and the other as a random alloy [38]. The AlInAsSb wafer lattice matched to InP was grown as a random alloy [40]. The layer structures are shown in Table 3.1. Both APDs employ InGaAs as p-type and n-type contact layers.

Table 3.1. Epitaxial structures of p^+-i-n^+ Sb-based APDs

Types	Material	Thickness (nm)	Doping (cm^{-3})
DA AlGaAsSb p^+-i-n^+ APD	InGaAs	20	p^{++}: 1×10^{19}
	AlGaAsSb	300	p^+: 2×10^{18}
	AlGaAsSb	890	UID
	AlGaAsSb	100	n^+: 2×10^{18}
	InGaAs	400	n^{++}: 1×10^{19}
	Semi-insulating InP substrate		
RA AlGaAsSb p^+-i-n^+ APD	InGaAs	20	p^{++}: 1×10^{19}
	AlGaAsSb	300	p^+: 2×10^{18}
	AlGaAsSb	1020	UID
	AlGaAsSb	100	n^+: 2×10^{18}
	InGaAs	500	n^{++}: 1×10^{19}
	Semi-insulating InP substrate		
RA AlInAsSb p^+-i-n^+ APD	InGaAs	20	p^{++}: 1×10^{19}
	AlInAsSb	300	p^+: 2×10^{18}
	AlInAsSb	1100	UID
	AlInAsSb	100	n^+: 2×10^{18}
	InGaAs	500	n^{++}: 1×10^{19}
	Semi-insulating InP substrate		

Random alloy growth technique is the one most frequently used to grow commercial III-V compounds such as InGaAs, InAlAs, and InP, where all the required growth parameters have been thoroughly developed. This growth method results in atoms being randomly distributed along the

growth direction. In contrast, a digital alloy consists of a periodic short-period superlattice structure consisting of binary or ternary materials. The $Al_xIn_{1-x}As_ySb_{1-y}$ material system lattice matched to GaSb substrate has been grown as digital alloys to solve the issue of the miscibility gap [2]. Given the challenges in growing $Al_xIn_{1-x}As_ySb_{1-y}$-based APDs on GaSb as random alloys, past comparisons between digital and random alloys have excluded Sb-based III-V materials. In this section, the AlGaAsSb APDs have been grown as digital alloys and random alloys, respectively, and the characteristics of digital alloy and random alloy Sb-based quaternary III-V materials on InP can be compared directly.

As shown in Fig. 3.1, the current-voltage (I-V) characteristics of 100-μm-diameter p^+-i-n^+ DA AlGaAsSb, RA AlGaAsSb, and RA AlInAsSb APDs were measured under dark and illuminated conditions at room temperature, and the gain was calculated from the corresponding photocurrent curves. A 445-nm semiconductor laser was used to illuminate these three devices. The dark current of these three APDs is more than two orders of magnitude lower than previously reported AlAsSb-based APDs [28, 38, 40], and the avalanche gain can reach around 20. Furthermore, the excess noise characteristics of these APDs were measured at room temperature, and the same 445-nm semiconductor laser was used to provide a nearly pure electron injection profile. Assuming that McIntyre's local field model [5] is valid as expressed in Eq. (1.2), the excess noise factor curves with effective k values of 0 to 0.1 in steps of 0.02 and 0.1 to 0.5 in steps of 0.1 are plotted in Fig. 3.2 as dash lines. The commonly used multiplication materials, Si, InAlAs, and InP, with effective k values of ~ 0.01 [12, 13], ~ 0.2 [41, 42], and ~ 0.45 [43, 44], are labeled as reference lines. As shown in Fig. 3.2, measured p^+-i-n^+ DA AlGaAsSb, RA AlGaAsSb, and RA AlInAsSb APDs exhibit similar low excess noise factor under 445-nm illumination with an effective k value of ~ 0.01, which is more than an order of magnitude lower than that of InAlAs and InP and comparable

to that of Si. In summary, AlGaAsSb- and AlInAsSb-based APDs exhibit low dark current and excess noise under room temperature, making them competitive multiplier candidates on InP substrates.

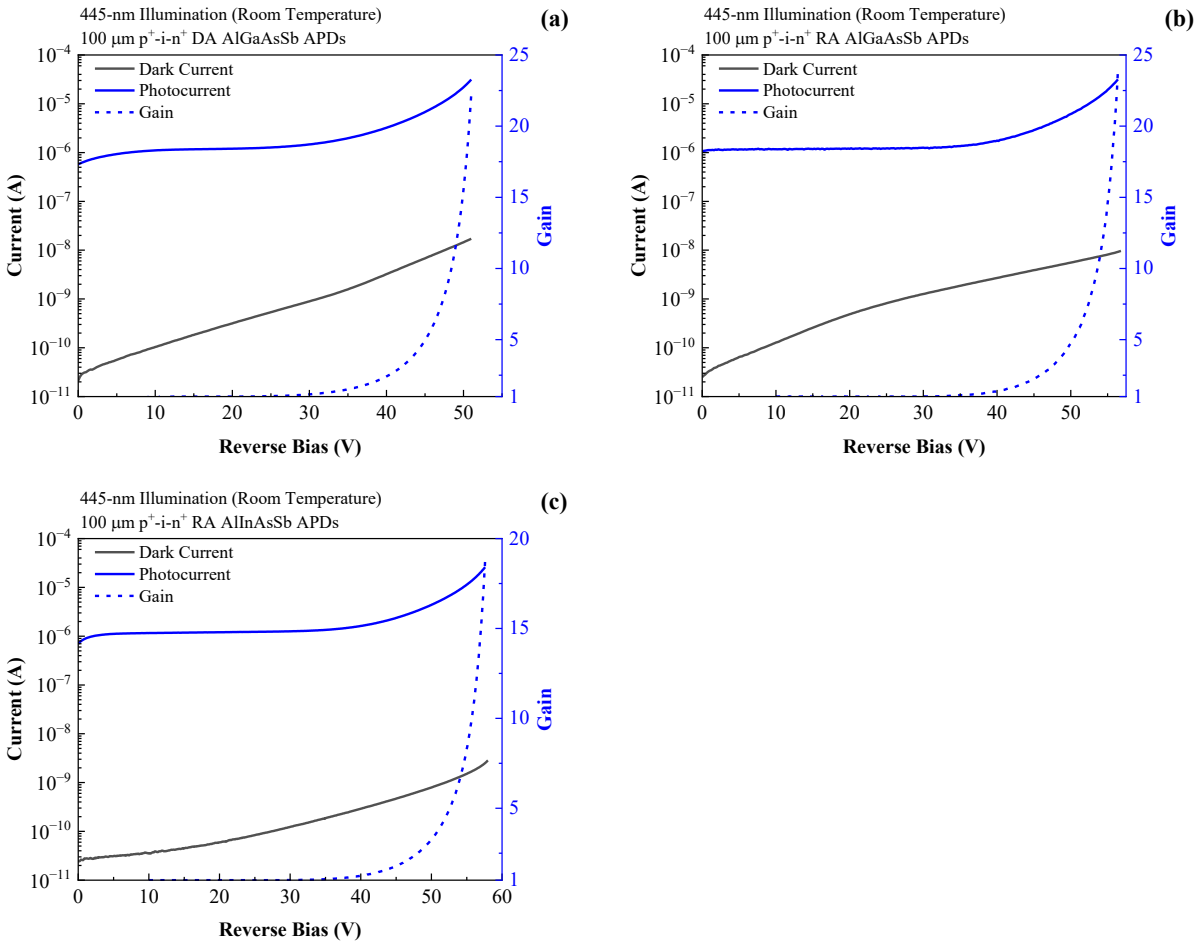

Figure 3.1. Dark current, photocurrent, and gain under 445-nm illumination for 100-µm-diameter p^+-i-n^+ (a) digital alloy AlGaAsSb, (b) random alloy AlGaAsSb, and (c) random alloy AlInAsSb APDs.

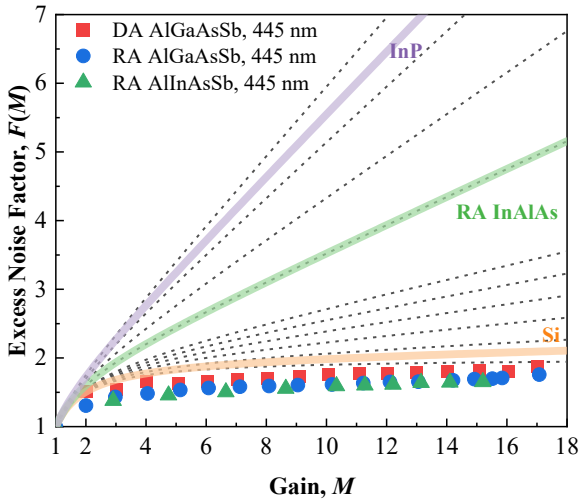

Figure 3.2. Excess noise characteristics of p^+-i-n^+ digital alloy AlGaAsSb, random alloy AlGaAsSb, and random alloy AlInAsSb APDs with thick multipliers in comparison to these of Si, random alloy InAlAs [41, 42], and InP [43, 44]. Dash lines indicate the excess noise predicted by McIntyre's local model for effective k values of 0 to 0.1 in steps of 0.02 and 0.1 to 0.5 in steps of 0.1.

3.2. Optical constants of $Al_{0.85}Ga_{0.15}As_{0.56}Sb_{0.44}$ and $Al_{0.79}In_{0.21}As_{0.74}Sb_{0.26}$

3.2.1. Motivation

Optical material parameters such as refractive indices and absorption coefficients play an important role in designing and optimizing optoelectronic devices [45]. For example, refractive indices are required to calculate the reflectivity, an important aspect of the optoelectronic device design [45]. For APDs the determination of the carrier injection profile requires knowledge of the absorption coefficients [36]. The extraction of impact ionization coefficients through the mixed injection method [46-48] also requires knowledge of the absorption coefficients for different wavelengths. Investigation of the optical constants of optoelectronic materials is beneficial for the design and characterization of the corresponding optoelectronic devices.

As noted in Section 3.1, two Sb-based quaternary materials, AlGaAsSb and AlInAsSb have been reported with low excess noise comparable to that of Si (k ~ 0.01) [12, 13]. Consequently,

these Sb-based materials have the potential to significantly impact applications which require high-sensitivity photodetectors. To date, however, the optical properties of these materials have not been reported. Previously, the interpolation of the absorption coefficients of the four binary materials was used to estimate those of AlGaAsSb [35], but the calculated optical constants determined by the interpolation method may not be highly accurate, since this approach neglects the complicated mixing methods in actual growth. Therefore, it is important to do optical characterizations of these two materials for optical constant extraction.

This study used variable-angle spectroscopic ellipsometry (VASE) to study the complex refractive indices and the absorption coefficients for DA AlGaAsSb and RA AlInAsSb APD wafers. The epitaxial structures are listed in Table 3.1. High-resolution XRD, cross-section SEM, and a contact profiler have verified the layer thicknesses.

A Kramers-Kronig-consistent basis spline function was chosen due to its flexibility and accuracy in approximating quaternary materials' optical constants. The external quantum efficiency has been calculated based on the extracted absorption coefficients and agrees well with the measured external quantum efficiency.

3.2.2. Ellipsometry measurements

Due to its non-destructive and accurate extraction nature [49], ellipsometry is widely employed to measure material optical properties. It measures the state of polarization change after the interaction between the incident polarized light and the material. The polarization change (ρ) of the reflected beam can be written as the ratio of parallel (r_p) and perpendicular (r_s) components along the light propagation,

$$\rho = \frac{r_p}{r_s} = \tan(\psi) e^{i\Delta}, \tag{3.1}$$

where ψ is the amplitude ratio, and Δ is the phase difference of p-polarized and s-polarized components. Since ellipsometry measures the amplitude ratio and phase difference for different wavelengths under various incident angles, the incident light intensity is less important, and the extracted optical properties are more accurate compared to the reflectometry [50].

Here, the sample optical constants were extracted from VASE measurements using an M-2000 ellipsometer. The measured wavelength range of AlGaAsSb and AlInAsSb was 400 nm – 850 nm and 400 nm – 950 nm, with incident angles from 50° to 65° and 5° steps. Different spectral ranges were chosen due to the different bandgaps for AlGaAsSb [28] and AlInAsSb [40]. The extracted absorption coefficients can only be verified through the measured external quantum efficiency up to the cut-off wavelength. The spectroscopic ellipsometry data was analyzed using CompleteEASE software (J.A. Woollam Co.).

As shown in Fig. 3.3, the red and green solid curves are measured ψ and Δ obtained from ellipsometry. To extract the optical constants of AlGaAsSb or AlInAsSb layers sandwiched by InGaAs contact layers, a multilayer model was built to analyze the interaction between the incident polarized light and unfabricated APD wafers in CompleteEASE simulation. The InP substrate and InGaAs contact layers' optical constants were defined using the literature-based CompleteEASE library. The layer thickness was determined to be as-grown with small variation. Therefore, the unknown parameters were only the optical constants of the p^+-i-n^+ AlGaAsSb or AlInAsSb layers, which were approximated to fit the measured ψ and Δ curves. The fit quality is quantitatively evaluated by Mean-Squared Error (MSE) [50], and an expression for MSE is

$$MSE_{NCS} = \sqrt{\frac{1}{3n_\lambda - m_f}\sum_{i=1}^{n_\lambda}\left[\left(\frac{N_{E_i} - N_{G_i}}{0.001}\right)^2 + \left(\frac{C_{E_i} - C_{G_i}}{0.001}\right)^2 + \left(\frac{S_{E_i} - S_{G_i}}{0.001}\right)^2\right]}, \tag{3.2}$$

where n_λ is the number of measurement wavelengths, m_f is the number of fitting parameters, $N = cos(2\psi)$, $C = sin(2\psi)cos(\Delta)$, and $S = sin(2\psi)sin(\Delta)$ are ellipsometry parameters to represent ψ and Δ by convention. The subscripts E and G stand for measured and generated data, respectively. A built-in nonlinear regression algorithm (the Levenberg–Marquardt method [51]) was employed to minimize the MSE by sweeping the fitting parameters in the multilayer model.

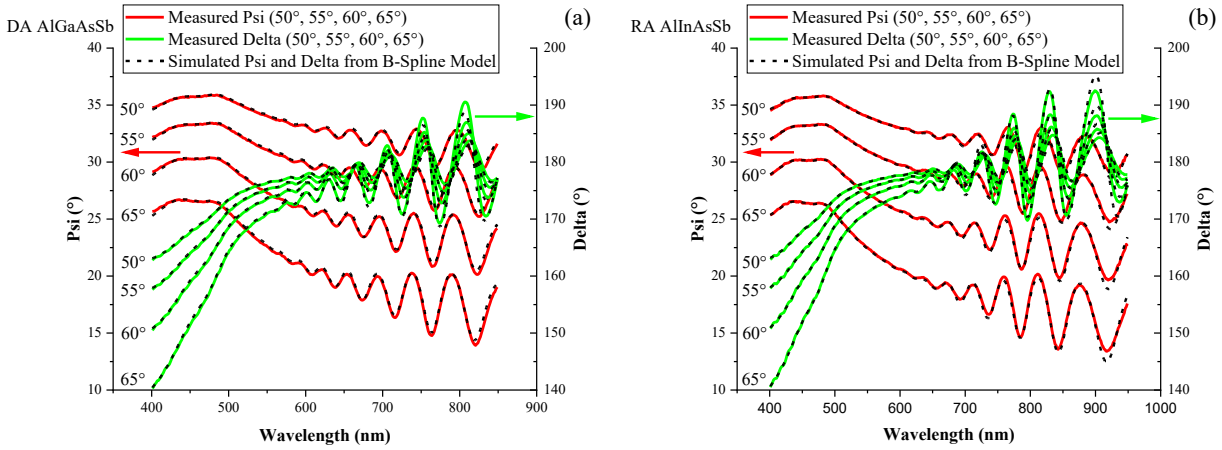

Figure 3.3. VASE data with 50° - 65° incident angle of (a) DA AlGaAsSb APD wafer ranging from 400 nm to 850 nm, and (b) RA AlInAsSb APD wafer ranging from 400 nm to 950 nm.

In this study, the investigated wavelength range stays inside the absorbing region of AlGaAsSb or AlInAsSb, and unknown layers can be modeled by an EMA (effective medium approximation), B-Spline (basis spline), and Gen-OSC (general oscillator).

The EMA approach approximates unknown layers by mixing two or three materials to generate optical constants. Standard mixing options are linear EMA, Bruggeman EMA, and Maxwell-Garnett EMA [52]. The Bruggeman EMA was utilized previously to fit measured ψ and Δ curves of $Al_{0.7}In_{0.3}As_{0.3}Sb_{0.7}$ [46] and $Al_{0.8}In_{0.2}As_{0.23}Sb_{0.77}$ [47] grown on GaSb substrate. As for $Al_{0.7}In_{0.3}As_{0.3}Sb_{0.7}$, acceptable ψ and Δ fitting was obtained and the extracted absorption coefficients from the EMA layer were utilized to fit the measured EQE up to 900 nm. However, the mismatch between the calculated and measured EQE was increasingly large after 900 nm,

which could be explained by the deviation of ψ and Δ values between the measurement and the layer model near the cut-off wavelength. If the physics-based EMA approach is chosen to model a quaternary material, the constituents of the EMA layer might be much different from the actual growth constituents, and different constituent combinations need to be tried to obtain better fitting results. At the same time, ψ and Δ values are sensitive to the ratio of constituents, and the expected content of four elements might vary from the actual growth. Furthermore, the flexibility of EMA fitting is restricted by three material mixing methods, and these methods can sometimes not depict the optical properties of quaternary materials. This study initially used the EMA approach to fit ψ and Δ curves of the AlGaAsSb and AlInAsSb layers. However, a similar mismatch issue between calculated and measured EQE near the cut-off wavelength occurred due to the fitting limitation of ψ and Δ.

The Gen-OSC approach approximates unknown layers by combining different physics-based oscillator lineshapes [53]. However, the Gen-OSC layer requires manually choosing the lineshape function, oscillator position, and number of oscillators. Proper starting parameters are also needed to implement the regression algorithm. Therefore, the Gen-OSC approach is strongly limited by the initial information and rough estimation of the unknown material. Due to the lack of previous data for the optical properties of AlGaAsSb and AlInAsSb on InP, this approach was not used.

Compared with the former approaches, the B-Spline approach has more flexibility in analyzing spectroscopic ellipsometry data since it implements curve fitting by connecting basis functions at specified nodes [54] rather than mixing different materials or summing various oscillator functions along the whole wavelength range. Adjusting a B-Spline function at a node does not influence the fitting of other nodes, and every specified region is relatively independent. Therefore, the B-Spline approach was chosen to build the AlGaAsSb or AlInAsSb layer models. Moreover, the B-Spline

layer was built to be Kramers-Kronig (KK) consistent [55], and a positive imaginary dielectric constant was enforced. The dash lines in Fig. 3.3 are simulated ψ and Δ from the B-Spline model. AlGaAsSb and AlInAsSb results show good fits for different incident angles, which indicates the robustness of the as-built B-Spline layer model.

Figure 3.4 shows the refractive index, n, and extinction coefficient, κ, as a function of the wavelength of AlGaAsSb and AlInAsSb. The absorption coefficient, α, can be extracted from the extinction coefficient, κ, using the relation $\alpha = 4\pi\kappa/\lambda$, where λ is the wavelength. The extracted absorption coefficients of AlGaAsSb and AlInAsSb are shown in Fig. 3.5. We note that these coefficients are much lower than the absorption coefficients of InGaAs. The strong absorption of the top InGaAs layer may influence the magnitude of absorption for the AlGaAsSb and AlInAsSb layers. However, the thickness of the top InGaAs layer is only 20 nm, and the ellipsometry measures the change of polarization states between the incident and reflected beams rather than the light intensity. The interaction between the light and the top InGaAs layer has also been included in the multilayer model. Therefore, the top InGaAs layer does not influence the extraction of absorption coefficients for AlGaAsSb and AlInAsSb.

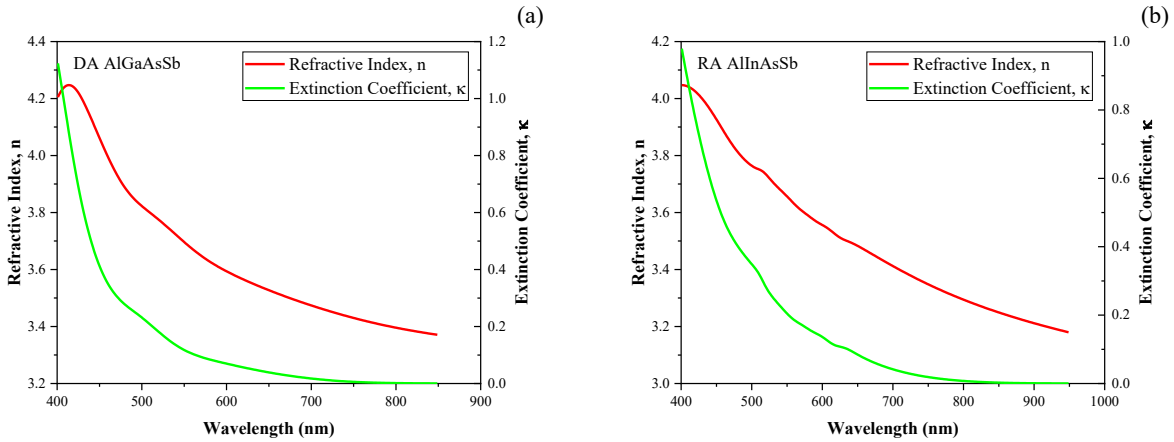

Figure 3.4. Refractive index and extinction coefficient versus wavelength for (a) DA AlGaAsSb within 400 nm - 850 nm, and (b) RA AlInAsSb within 400 nm - 950 nm.

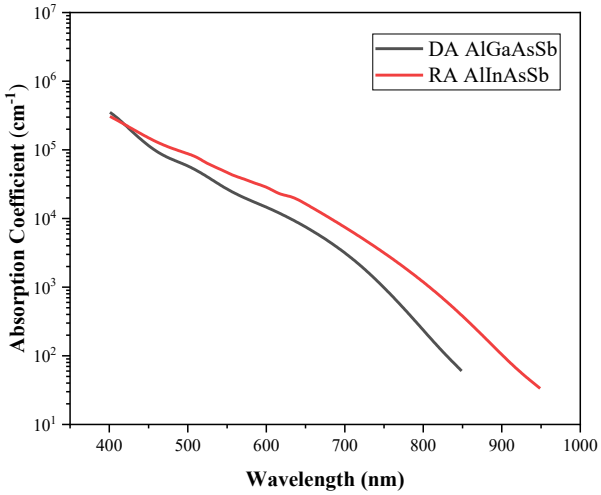

Figure 3.5. Absorption coefficients versus wavelength of DA AlGaAsSb (black) and RA AlInAsSb (red).

The calculated EQE was compared to measurements to estimate the absorption coefficients' accuracy. The EQE of 200-µm, 250-µm, and 350-µm AlGaAsSb and AlInAsSb APDs were measured at unity gain as illustrated in Fig. 3.6. The EQE for different diameters (≥ 200 µm) exhibits the same shape and magnitude, which means that the light spot is entirely inside the device. The EQE was calculated based on the extracted absorption coefficients of AlGaAsSb and AlInAsSb under the ideal normal incidence condition. Moreover, when the measurement wavelength goes below 450 nm, the photocurrent of both measured devices and commercialized Si photodiodes is low, producing more differences between calculated and measured EQE. Although the discrepancy is larger at the shorter wavelength, the calculated and measured EQE still agrees well inside the whole measurement range for both AlGaAsSb and AlInAsSb APDs.

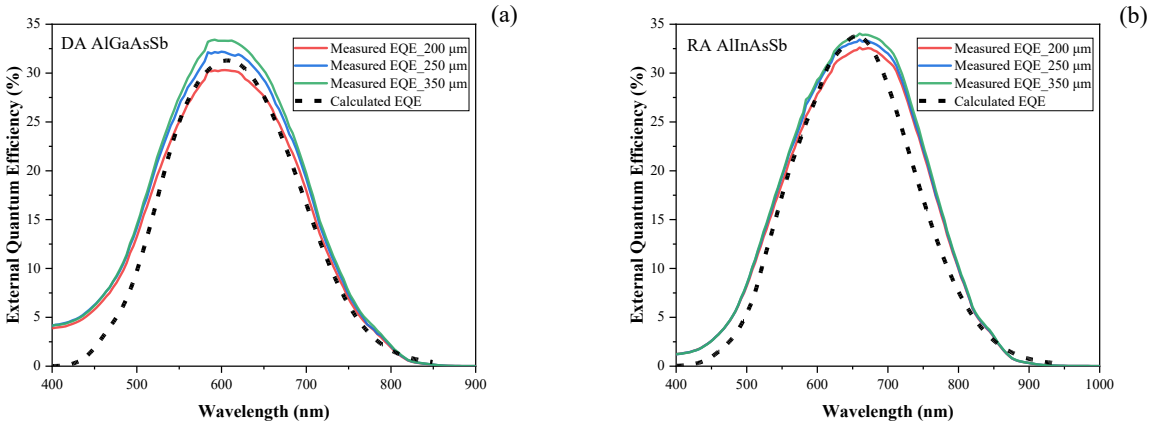

Figure 3.6. Measured and calculated EQE versus wavelength at the unity gain point of (a) DA AlGaAsSb and (b) RA AlInAsSb. The solid lines represent the measured EQE of 200-µm, 250-µm, and 350-µm devices, and the dashed line is the calculated EQE based on the extracted absorption coefficients.

3.2.3. Conclusion

Different fitting methods for spectroscopic ellipsometry data have been discussed, and a Kramers-Kronig-consistent B-Spline approach provides more flexibility and accuracy to approximate quaternary materials than EMA and Gen-OSC approaches do. The absorption coefficients and complex refractive indices of AlGaAsSb (400 nm - 850 nm) and AlInAsSb (400 nm - 950 nm) have been determined, and EQE measurements verified the extracted absorption coefficients. These optical constants are important for optoelectronic device simulation.

3.3. Impact ionization coefficients of DA and RA $Al_{0.85}Ga_{0.15}As_{0.56}Sb_{0.44}$

3.3.1. Motivation

The impact ionization coefficients of electrons (α) and holes (β) are key factors describing the mean ionization rate per unit distance in a random ionization process. Characterizing the impact ionization coefficients plays an important role in the simulation of multiplication gain, and the knowledge of impact ionization coefficients is beneficial for the future utilization of the

investigated material system. The impact ionization coefficients of commercially available multiplication materials including InP [43], InAlAs [56], and Si [57] have been already extracted, and the corresponding multiplication gain simulations have contributed much to the optimization of SACM APD designs.

As mentioned in Section 3.1, APDs based on $Al_xIn_{1-x}As_ySb_{1-y}$ and $Al_xGa_{1-x}As_ySb_{1-y}$ materials systems [2] have exhibited low excess noise. As for the $Al_xIn_{1-x}As_ySb_{1-y}$ material system, DA $Al_xIn_{1-x}As_ySb_{1-y}$ APDs on GaSb with x = 0.5, 0.6, 0.7, and 0.8 exhibited *k* values as low as 0.01 [16, 47], and the impact ionization coefficients of $Al_{0.7}In_{0.3}As_ySb_{1-y}$ and $Al_{0.8}In_{0.2}As_{0.23}Sb_{0.77}$ on GaSb have been extracted based on the mixed injection method [46, 47]. As for the $Al_xGa_{1-x}As_ySb_{1-y}$ material system lattice matched to InP, AlAsSb shows an effective *k* value at 0.005, and its impact ionization coefficients have been extracted based on the pure carrier injection method [11].

Likewise, AlInAsSb and AlGaAsSb APDs on InP have shown a *k* value comparable to that of Si, making them promising multiplier candidates for SACM APDs. It is essential to follow a similar approach to determine the impact ionization coefficients of these two materials. In this study, the extraction focuses on the $Al_{0.85}Ga_{0.15}As_{0.56}Sb_{0.44}$ APDs on InP substrates. The determination of impact ionization coefficients for $Al_{0.85}Ga_{0.15}As_{0.56}Sb_{0.44}$ is not only beneficial for the future design of high gain-bandwidth-product and low-noise SACM APDs [58] but also advantageous for the understanding of the physical mechanisms that contribute to low noise for Sb-based APDs.

In this work, the gain characteristics of two DA and six RA AlGaAsSb APDs with different multiplier thicknesses were used to determine the electron and hole ionization coefficients of the AlGaAsSb over a wide electric field range. Two different methods of impact ionization coefficient

extraction were employed. For the first approach, the electric-field-dependent impact ionization coefficients were extracted from the gain characteristics using a "local" model where the carrier ionization is assumed to be only a function of the electric field at that point [59-61], and no allowance is made for any "dead-space" [62]. The experimental gain curves of p^+-i-n^+ and n^+-i-p^+ APDs under pure electron and hole injection profiles were respectively compared to simulations of the multiplication gain using these impact ionization coefficients. As for the second approach, the impact ionization coefficients were extracted through a mixed injection method [48], an extraction approach that was used for $Al_{0.7}In_{0.3}As_ySb_{1-y}$ and $Al_{0.8}In_{0.2}As_{0.23}Sb_{0.77}$ on GaSb [46, 47], where the multiplication occurs due to the creation of electrons and holes within the depletion region of the p^+-i-n^+ APDs. The extracted impact ionization coefficients from these two approaches have minor differences.

3.3.2. Epitaxial crystal growth

The APDs were grown as p^+-i-n^+ and n^+-i-p^+ structures with different multiplier thicknesses on semi-insulating InP substrates by molecular beam epitaxy. The epitaxial structures are shown in Table 3.2, and APDs with symmetrical p^+-i-n^+ and n^+-i-p^+ structures are listed in the same row.

The multiplier thickness ranges from 87 nm to 1 μm with the growth details of some layers provided previously [28, 36-38]. With the exception of the 890-nm thick p^+-i-n^+ and n^+-i-p^+ multiplier structures, which were grown as digital alloys [16, 28, 33], other samples in this study were grown as random alloys [34-38]. The gain characteristics of the thinner structures have been reported previously [36, 37], so data from the literature was used in the analysis. For the three thickest samples, the gain characteristics were measured in this study.

Table 3.2. Epitaxial structures of p^+-i-n^+ and n^+-i-p^+ AlGaAsSb APDs

Types	Material	Doping (cm^{-3})	Thickness (nm)
Random alloy p^+-i-n^+ (n^+-i-p^+) APDs [36]	InGaAs	p^{++} (n^{++})	100 (100)
	AlGaAsSb	p^+: 1.5×10^{18} (n^+: 2.4×10^{18})	300 (300)
	AlGaAsSb	UID	87 (98)
	AlGaAsSb	n^+: 1.5×10^{18} (p^+: 2.4×10^{18})	200 (200)
	InGaAs	n^{++} (p^{++})	1000 (1000)
	Semi-insulating InP substrate		
Random alloy p^+-i-n^+ (n^+-i-p^+) APDs [36]	InGaAs	p^{++} (n^{++})	100 (100)
	AlGaAsSb	p^+: 1.25×10^{18} (n^+: 2.4×10^{18})	300 (300)
	AlGaAsSb	UID	170 (193)
	AlGaAsSb	n^+: 1.25×10^{18} (p^+: 2.4×10^{18})	200 (200)
	InGaAs	n^{++} (p^{++})	1000 (1000)
	Semi-insulating InP substrate		
Digital alloy p^+-i-n^+ [28] (n^+-i-p^+) APDs	InGaAs	p^{++} (n^{++})	20 (20)
	AlGaAsSb	p^+: 1×10^{18} (n^+: 1×10^{18})	300 (300)
	AlGaAsSb	UID [1.5×10^{16} (1.9×10^{16})]	890 (890)
	AlGaAsSb	n^+: 1×10^{18} (p^+: 1×10^{18})	100 (100)
	InGaAs	n^{++} (p^{++})	400 (400)
	Semi-insulating InP substrate		
Random alloy p^+-i-n^+ APDs [37]	InGaAs	p^{++}	50
	AlGaAsSb	p^+: 1×10^{18}	300
	AlGaAsSb	UID [5×10^{15}]	608
	AlGaAsSb	n^+: 1×10^{18}	200
	InGaAs	n^{++}	500
	Semi-insulating InP substrate		
Random alloy p^+-i-n^+ APDs [38]	InGaAs	p^{++}	20
	AlGaAsSb	p^+: 1×10^{18}	300
	AlGaAsSb	UID [1×10^{15}]	1020
	AlGaAsSb	n^+: 1×10^{18}	100
	InGaAs	n^{++}	500
	Semi-insulating InP substrate		

3.3.3. Experiments and results

3.3.3.1. Random path length simulation

The current-voltage (I-V) characteristics of the three thickest AlGaAsSb p^+-i-n^+ and n^+-i-p^+ APDs measured at room temperature under dark and illuminated conditions were used to determine the gain curves. A 450 nm semiconductor laser was used to illuminate the devices to provide a pure carrier injection profile [63], and the multiplication gain was determined from the

photocurrent [64]. These gain results are plotted as log (M – 1) verse reverse bias to show the full range of multiplication obtained in Fig. 3.7.

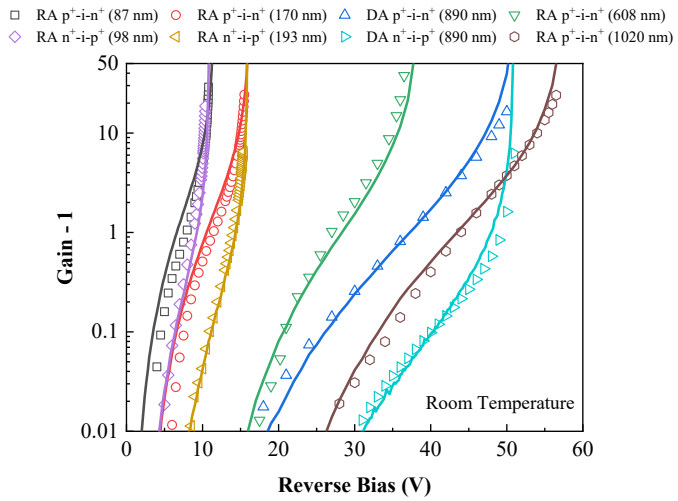

Figure 3.7. Comparison between measured gain (symbols) under 450-nm illumination and simulated gain (solid lines) from the random path length model for p^+-i-n^+ and n^+-i-p^+ AlGaAsSb APDs with different multiplier thickness at room temperature.

Our collaborators at the University of Sheffield extracted the impact ionization coefficients from the gain curves using an iterative numerical technique based on a random path length (RPL) model [59-61] for all eight structures. As shown in Fig. 3.7, a good agreement is obtained between the measured and simulated gain curves. The extracted impact ionization coefficients for electrons and holes are shown in Fig. 3.8. The corresponding analytical expressions cover a wide electric field range from 260 – 1000 kV/cm for impact ionization coefficients of electrons and 200 – 1000 kV/cm for impact ionization coefficients of holes, and they are given by

$$\alpha = \begin{cases} 5.5\times10^5 \exp\left(-\left(\dfrac{1.21\times10^6}{E}\right)^{1.43}\right) cm^{-1}, \; when \; 260\; kV/cm < E < 500\; kV/cm \\ 8.0\times10^5 \exp\left(-\left(\dfrac{1.30\times10^6}{E}\right)^{1.43}\right) cm^{-1}, \; when \; 500\; kV/cm < E < 1000\; kV/cm \end{cases}, \quad (3.3)$$

$$\beta = \begin{cases} 2.5\times10^{5}\exp\left(-\left(\dfrac{1.70\times10^{6}}{E}\right)^{1.44}\right) cm^{-1}, \; when \; 200\; kV/cm < E < 500\; kV/cm \\ 4.5\times10^{5}\exp\left(-\left(\dfrac{1.92\times10^{6}}{E}\right)^{1.38}\right) cm^{-1}, \; when \; 500\; kV/cm < E < 1000\; kV/cm \end{cases}, \quad (3.4)$$

where E is the electric field in V/cm.

The impact ionization coefficients of electrons in AlGaAsSb were found to be similar to AlAsSb [11] except at very high electric fields (> 500 kV/cm) as shown in Fig. 3.8. The bandgap changes slightly from AlAsSb to AlGaAsSb, with the X-valley bandgap changing from 1.64 eV to 1.56 eV and the Γ-valley bandgap changing from 1.95 eV to 1.77 eV [34]. This explains the similar impact ionization coefficients of electrons to AlAsSb but not the larger hole impact ionization coefficients. Similar behavior has been reported in $Al_xGa_{1-x}As$ and $(Al_xGa_{1-x})_{0.52}In_{0.48}P$ lattice matched to GaAs [60], and for high Al composition, the breakdown voltage and impact ionization coefficients do not change much with Al variations. Figure 3.8 shows that the α in AlGaAsSb is not only similar to that of AlAsSb [11] over much of the electric field range but also similar to α seen in InAlAs [56] and InP [43] (not shown for clarity). While the α at a typical electric field of 350 kV/cm in these four semiconductors is effectively identical at 1648 cm^{-1}, β shows orders of magnitude difference with β = 3300 cm^{-1} in InP, 167 cm^{-1} in InAlAs, 19 cm^{-1} in AlGaAsSb and 1.5 cm^{-1} in AlAsSb.

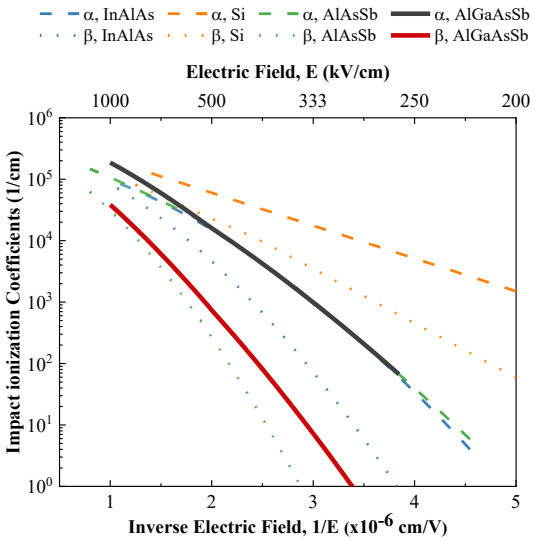

Figure 3.8. Comparison of impact ionization coefficients of electrons and holes for AlGaAsSb, AlAsSb [11], Si [57], and InAlAs [56]. α of AlGaAsSb is similar to that of AlAsSb and InAlAs, and these lines overlap at low electric fields.

3.3.3.2. Mixed injection method

Determining the impact ionization coefficients of electrons and holes from multiplication gain under pure electron injection profile (M_e) and under pure hole injection profile (M_h) taken on different p^+-i-n^+ and n^+-i-p^+ structures has the risk that small changes in the electric field profiles in the structures or the Al:Ga composition can introduce errors. Therefore, a mixed injection [48] was employed to initiate the multiplication by both electrons and holes in the same structure, extracting the impact ionization coefficients for the DA AlGaAsSb APD with the 890-nm multiplier. The only requirement with this technique is the accurate knowledge of absorption coefficients of this material. This mixed injection method has been used to successfully extract the impact ionization coefficients for InGaAs [48], $Al_{0.7}In_{0.3}As_{0.3}Sb_{0.7}$ [46], and $Al_{0.8}In_{0.2}As_{0.23}Sb_{0.77}$ [47].

To obtain pure electron injection and mixed injection profiles, the light sources included a semiconductor laser to provide the 445-nm illumination and a He-Ne laser to provide the 543- and

633-nm illumination. Multiplication gain under three different carrier injection profiles was then calculated from the photocurrent, as shown in Fig. 3.9(a). With the illumination wavelength increasing, the pure electron injection profile transitions to the mixed injection profile, and a lower gain is obtained, an indication that the impact ionization coefficients of holes (β) are lower than those of electrons (α) [11].

The gain for an electron-hole pair created at position x of an ideal p^+-i-n^+ APD can be expressed by the local field model as [21]

$$M(x) = \frac{(\alpha - \beta)e^{-(\alpha-\beta)x}}{\alpha e^{-(\alpha-\beta)w} - \beta}, \tag{3.5}$$

where w is the depletion width. Combining the injection profile with the location-dependent gain, the mixed injection multiplication M_{mix} is expressed by [48]

$$M_{mix} = \frac{\int_0^w M(x)G(x)dx}{\int_0^w G(x)dx}, \tag{3.6}$$

$$G(x) \propto e^{-\gamma x}, \tag{3.7}$$

where $G(x)$ is the carrier-generation rate, and γ is the absorption coefficient. The absorption coefficients of AlGaAsSb have been extracted via ellipsometry in Section 3.2 [63].

By inserting the absorption coefficients of every layer and the measured gain curves into Eq. (3.6), the impact ionization coefficients of electrons and holes can be extracted [46, 47], and the simulated gain curves agree well with measured gain curves under 445-, 543-, and 633-nm illumination as shown in Fig. 3.9(b). Then, the impact ionization coefficients of electrons and holes extracted from two different methods are compared in Fig. 3.10. These two results of impact ionization coefficients agree well, with the small difference seen possibly due to the assumption of a constant electric field profile in the multiplication region in the mixed injection analysis.

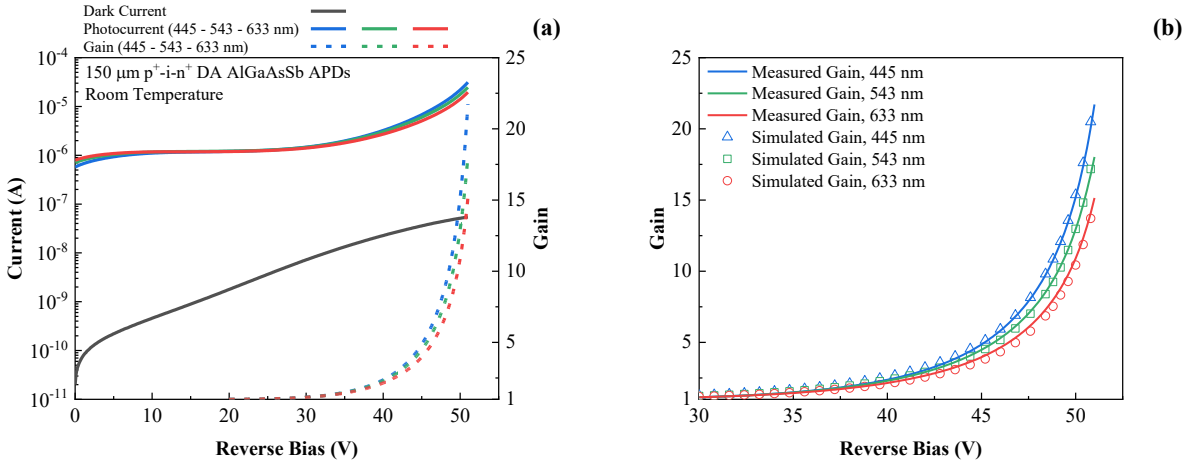

Figure 3.9. (a) Dark current, photocurrent, and gain under 445, 543, 633 nm illumination for a 150-μm-diameter p^+-i-n^+ digital alloy AlGaAsSb APD with the 890-nm multiplier at room temperature. (b) Comparison between measured gain curves (solid lines) and simulated gain curves (points) based on the mixed injection method.

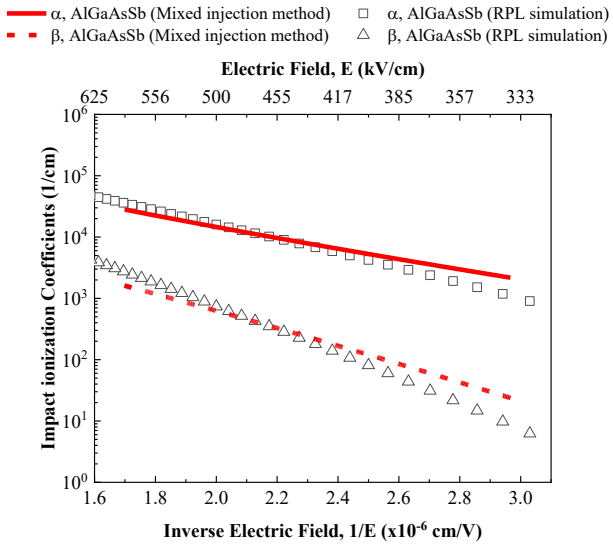

Figure 3.10. Comparison of impact ionization coefficients of electrons and holes for AlGaAsSb extracted by the mixed injection method and by the random path length simulation.

3.3.4. Discussion

As shown in Fig. 3.8, a large impact ionization coefficient ratio has been obtained for the $Al_xGa_{1-x}As_ySb_{1-y}$ material system, and although the electron ionization coefficients are similar to other materials like InAlAs, the hole ionization coefficient appears to be significantly reduced.

This reduction in hole ionization coefficient may however be due to the Sb content. Generally, in a semiconductor at high electric fields, holes gain energy and scatter from the heavier heavy/light-hole bands to the lighter split-off band from where they rapidly gain energy until they ionize. The heavier group V Sb atom has high spin-orbit coupling which pushes down the split-off band in the alloy band structure deeper into the valence band. This leads to an increase in the valence band spin-orbit splitting energy (Δ_{so}) [65]. Holes in the heavy/light hole bands may now reach the Brillouin zone edge and not be able to scatter into the split-off band. Consequently, the hole impact ionization rate is significantly reduced. This creates a large asymmetry between the electron and hole ionization coefficients, leading to a lower value of *k*. It has been showed recently in GaAsBi, which also has strong spin-orbit coupling due to the heavy Bi atom, that the increased Δ_{so} makes it harder for holes to scatter from the heavy/light-hole bands into the split-off band where their ionization threshold is gained [66], hence reducing the hole ionization coefficients.

This work also suggests that there is no obvious difference in impact ionization coefficients between DA and RA AlGaAsSb, which is different from the previous report of impact ionization coefficients for InAlAs [67]. Both types of AlGaAsSb alloy contain the heavy Sb atoms which leads to a large Δ_{so}. For the AlGaAsSb system, we have a Δ_{so} of 0.5 eV for the random alloy and 0.44 eV for the digital alloy [65]. The Δ_{so} of this quaternary alloy is much larger than that of other non-Sb-containing alloys (e.g. InP, InAlAs). The slightly smaller value for Δ_{so} in the digital alloy may be compensated for by the presence of small minigaps [29] in these periodic structures that localize holes and prevent hole impact ionization from occurring. As a result, the two alloy types may effectively have similar hole ionization coefficients.

It is interesting to note that the impact ionization coefficients given by Eqs. (3.3) and (3.4) appear to be capable of replicating the avalanche multiplication in all the devices studied as shown

in Fig. 3.7, even those with very narrow avalanche widths. Figure 3.11, plotted so as to expand the voltage axis at low values, however shows that for the two thinnest p^+-i-n^+ structures, the local model actually overestimates the electron initiated multiplication at low values of multiplication. This is a clear indication that the "dead-space", the minimum distance cool carriers injected into the avalanche region need to travel to be in equilibrium with the high electric field, is suppressing the onset of electron impact ionization at low biases in very thin structures as observed in other materials like AlGaAs [68] and InAlAs [56]. This effect is strongest in the thinnest p^+-i-n^+ structure and is negligible by the time the avalanche region width is ~ 600 nm or larger. A more in-depth analysis of the validity of the local model in the determination of avalanche multiplication was undertaken by Plimmer *et al*. [9] on GaAs p^+-i-n^+ structures, where experimental measurements were compared to local and Monte Carlo models. The results showed that the local model worked well for the i-region thicknesses greater than 200 nm.

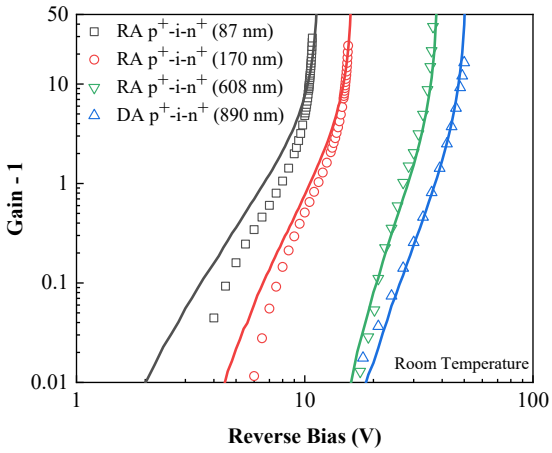

Figure 3.11. Comparison of impact ionization coefficients of electrons and holes for AlGaAsSb extracted by the mixed injection method and by the random path length simulation.

3.3.5. Conclusion

The gain characteristics under different injection profiles have been investigated for DA and RA AlGaAsSb APDs with different multiplier thickness in p^+-i-n^+ and n^+-i-p^+ structures. The impact ionization coefficients of electrons and holes have been determined from multiplication gain curves obtained with pure carrier injection profiles and by also employing a mixed injection method to independently extract the impact ionization coefficients. Both approaches gave effectively identical results. No discernable difference could be seen between the impact ionization coefficients of the structures grown as digital alloys and those grown as random alloys. The results show that the α in AlGaAsSb (85%) is identical to that of AlAsSb for electric fields up to 500 kV/cm while the β is larger, especially at low electric fields. The parameterized impact ionization coefficients can accurately replicate the multiplication characteristics of avalanche region down to approximately 600 nm, but for structures that are < 200 nm, corrections for the "dead-space" are required to accurately predict the low values of electron multiplication.

3.4. Temperature dependence of avalanche breakdown of AlGaAsSb and AlInAsSb APDs

3.4.1. Motivation

Various factors including dark current, excess noise, and the temperature stability of the multiplication gain determine the choice of the multiplier material. The excess noise and dark current characteristics at room temperature have been discussed for $Al_xIn_{1-x}As_ySb_{1-y}$ and $Al_xGa_{1-x}As_ySb_{1-y}$ material systems in Section 3.1. Another parameter to be investigated is the temperature stability of the multiplication gain.

Typically, the carriers in the multiplication region acquire the ionization threshold energy from the high electric field [69], and loss of energy occurs primarily through scattering, with phonon scattering being dominant. Phonon scattering exhibits strong positive temperature dependence. This results in significant variation of the gain with temperature; higher reverse bias is required to maintain the same gain at higher temperature. In practice, in order to maintain a stable gain, an active variable bias circuit or a thermoelectric cooler is required to control either the applied reverse bias or the operating temperature, increasing the cost and the system complexity [61]. The simplest and most straightforward way to simplify the bias or temperature control circuits is to choose a multiplier material with weak temperature dependence of avalanche breakdown.

Previously, thick DA $Al_xIn_{1-x}As_ySb_{1-y}$ lattice matched to GaSb with x = 0.6, 0.7, 0.8, [47, 70, 71] and thin RA $Al_xGa_{1-x}As_{0.56}Sb_{0.44}$ lattice matched to InP with x = 1, 0.95, 0.9, 0.85 [72, 73] have exhibited weak temperature dependence of avalanche breakdown. After demonstrating thick DA $Al_{0.85}Ga_{0.15}As_{0.56}Sb_{0.44}$ APDs [28], and thick RA $Al_{0.85}Ga_{0.15}As_{0.56}Sb_{0.44}$ [38] APDs, and thick RA $Al_{0.79}In_{0.21}As_{0.74}Sb_{0.26}$ APDs [40] lattice matched to InP with low k values in Section 3.1, it follows that it is useful to determine the temperature characteristics of these new materials.

The temperature sensitivity is characterized by the temperature coefficient of breakdown voltage [74], which is expressed as

$$C_{bd} = \frac{\Delta V_{bd}}{\Delta T}, \tag{3.8}$$

where ΔV_{bd} is the change of the breakdown voltage, and ΔT is the change of the temperature. The temperature coefficient of breakdown voltage is determined by the material and the multiplier thickness. As the multiplier thickness increases, C_{bd} increases due to increased temperature-dependent phonon scattering [75].

In this section, I have studied the avalanche breakdown with temperature variation for DA AlGaAsSb, RA AlGaAsSb, and RA AlInAsSb p^+-i-n^+ APDs. An explanation for the weak temperature dependence of avalanche breakdown is provided based on the calculation of alloy disorder potentials and alloy scattering rates. In addition, the variation of the bandgap with temperature was investigated with photoluminescence and quantum efficiency measurements.

3.4.2. Temperature-dependent avalanche breakdown

APDs were placed in a nitrogen-cooled cryogenic chamber, and the current-voltage (I-V) characteristics of 150-µm-diameter APDs were measured under dark and illuminated conditions. A 520-nm fiber-coupled laser source was used to illuminate the device. The gain, M, was calculated from the photocurrent, and the breakdown voltage can be determined by the extrapolation of the inverse gain, $1/M$, to zero. This $1/M$ extrapolation method has been utilized in various $Al_xGa_{1-x}As_ySb_{1-y}$ and $Al_xIn_{1-x}As_ySb_{1-y}$ samples, and a good linear fitting of $1/M$ data has been obtained [47, 70-73]. Finally, the temperature coefficient of breakdown voltage, C_{bd}, is the slope of the linear fitting to the breakdown voltages under different temperatures.

Figure 3.12 shows (a) the gain versus voltage, (b) the inverse gain curves, and (c) the dark current curves in the range of 78 K to 360 K for DA AlGaAsSb APDs. Figure 3.13 shows similar curves for RA AlGaAsSb APDs in the 200 K to 340 K temperature range. The measurements on RA AlInAsSb APDs in the temperature range of 200 K to 320 K are shown in Fig. 3.14. Based on the linear regression approach, the fitting curves of breakdown voltages under different temperatures are calculated in Fig. 3.15, and the C_{bd} is determined to be (4.22 ± 0.08) mV/K, (5.92 ± 0.36) mV/K, and (5.91 ± 0.37) mV/K for DA AlGaAsSb, RA AlGaAsSb, and RA AlInAsSb APDs. Values of C_{bd} for these three materials, commercially available materials (including InP, InAlAs, Si [74, 75]), and recently reported Sb-based materials [47, 61, 70-73] are shown in Fig.

3.16. The temperature coefficient of breakdown voltage of these three materials is significantly lower than InP, InAlAs, or Si [74, 75] with the same multiplier thickness.

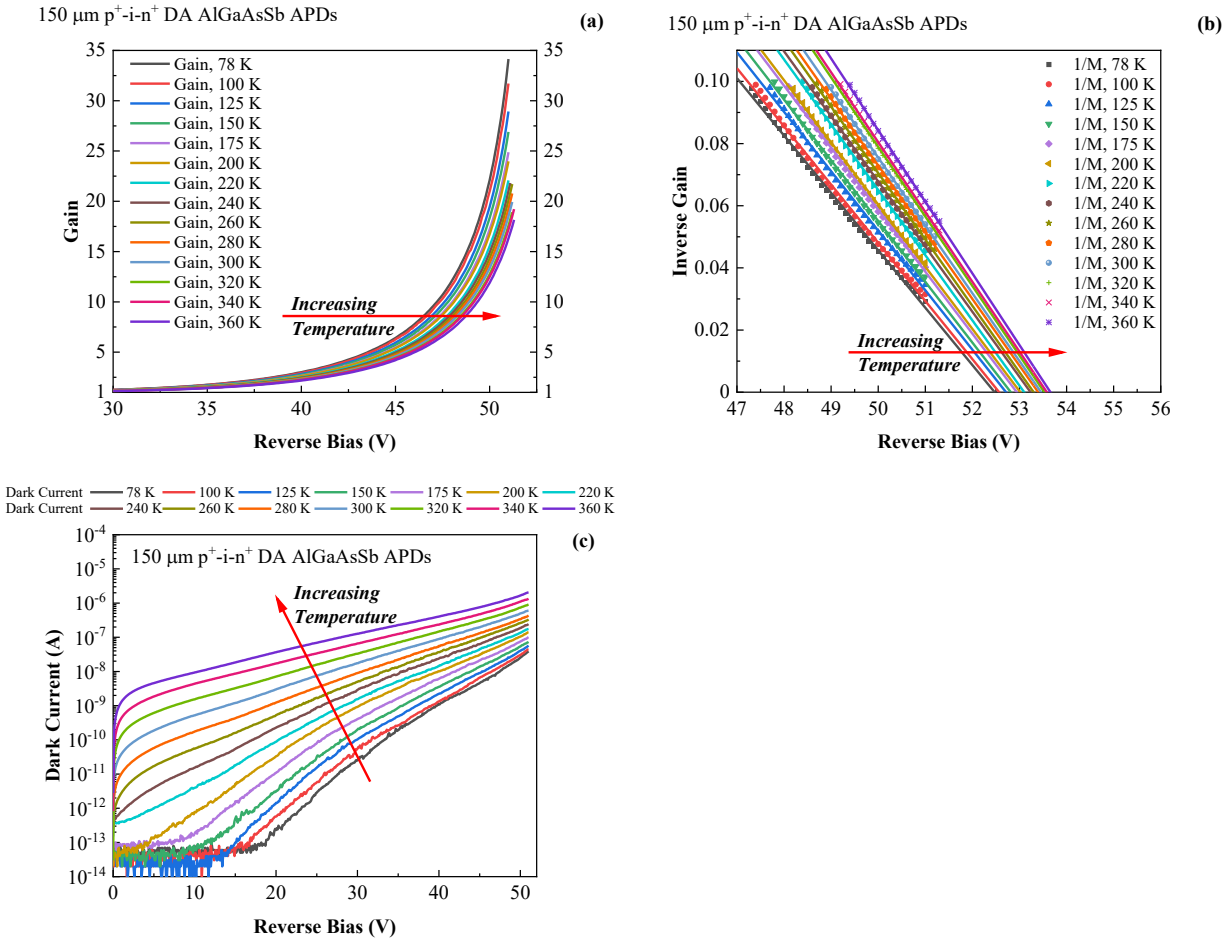

Figure 3.12. (a) Measured gain curves, (b) inverse gain (symbols) and linear fitting (solid lines) under 520-nm illumination, and (c) dark current cruves for 150-μm-diameter p^+-i-n^+ DA AlGaAsSb APDs from 78 K to 360 K.

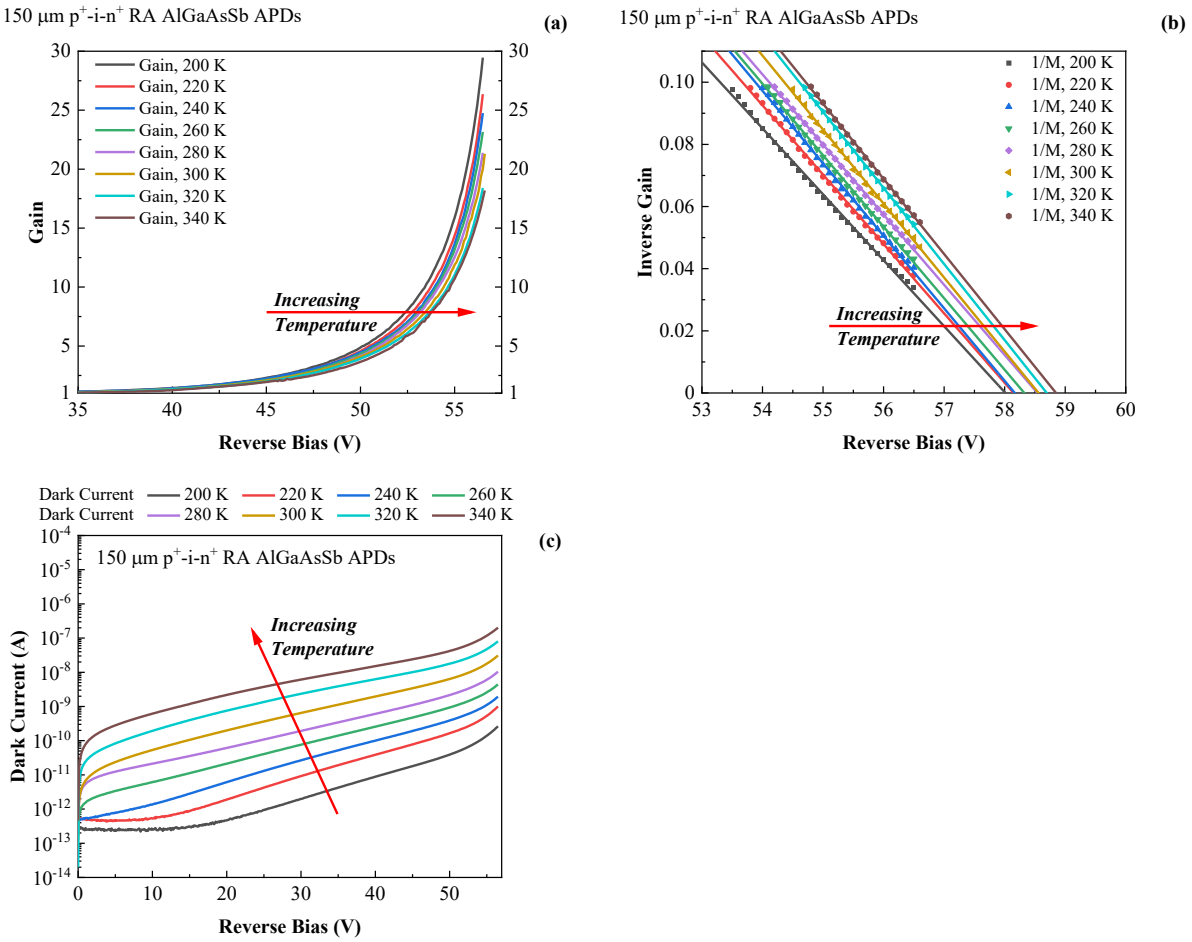

Figure 3.13. (a) Measured gain curves, (b) inverse gain (symbols) and linear fitting (solid lines) under 520-nm illumination, and (c) dark current cruves for 150-μm-diameter p^+-i-n^+ RA AlGaAsSb APDs from 200 K to 340 K.

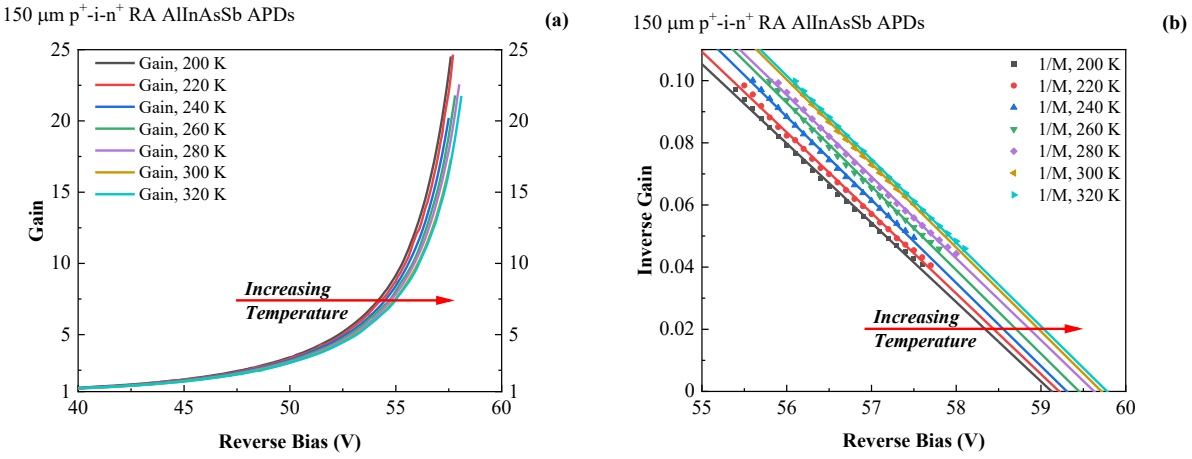

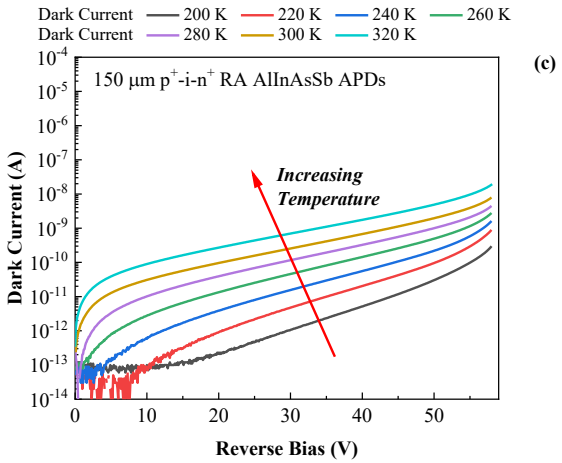

Figure 3.14. (a) Measured gain curves, (b) inverse gain (symbols) and linear fitting (solid lines) under 520-nm illumination, and (c) dark current cruves for 150-μm-diameter p^+-i-n^+ RA AlInAsSb APDs from 200 K to 320 K.

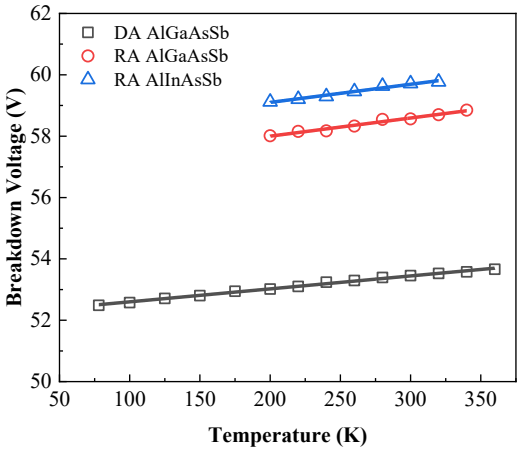

Figure 3.15. Temperature dependence of avalanche breakdown for p^+-i-n^+ DA AlGaAsSb, RA AlGaAsSb, and RA AlInAsSb APDs. Symbols are measured breakdown voltages, and solid lines are linear fitting curves.

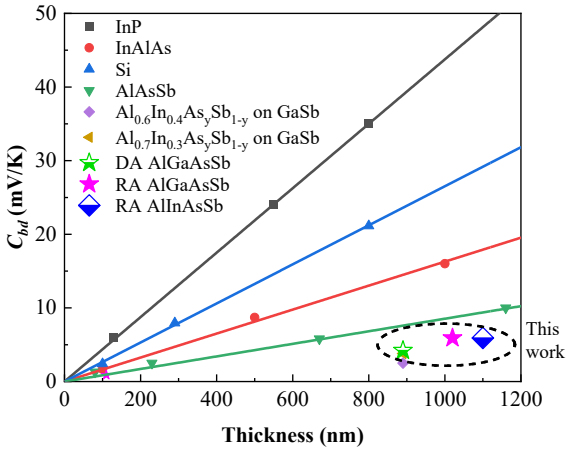

Figure 3.16. Comparison of the temperature coefficient of breakdown voltage between studied DA AlGaAsSb (green star), RA AlGaAsSb (pink star), RA AlInAsSb (blue square), and other materials including InP [74], InAlAs [74], Si [75], AlAsSb [61], thin RA AlGaAsSb lattice matched to InP [73], and thick DA $Al_xIn_{1-x}As_ySb_{1-y}$ lattice matched to GaSb with x = 0.6, 0.7 [70]. Symbols are measured values, and solid lines are linear fits.

3.4.3. Discussion

3.4.3.1. Role of alloy scattering in Sb-based quaternary alloys

Previously, it has been observed that ternary alloys have lower C_{bd} compared to binary compounds. The low C_{bd} of ternary alloys was attributed to the dominance of the temperature-independent alloy scattering over the temperature-dependent phonon scattering [76]. In a random alloy, for example, a ternary alloy, the constituent atoms are distributed randomly, leading to fluctuations in the crystal potential. This fluctuating potential results in an effective scattering process, referred to as alloy scattering, which impacts the movement of electrons through the crystal [77]. In contrast, the small thickness of the binary/ternary layers in digital alloys can create interface roughness, leading to fluctuations of the crystal potential at the interfaces. Thus, the alloy scattering exists in both alloys.

Considering that Sb-based quaternary alloys exhibit even lower C_{bd} compared to both ternary and binary alloys, it appears that alloy scattering also plays a significant role in the temperature dependence of the breakdown voltage for these new materials. To understand the significance of this scattering mechanism in these materials, Dr. Sheikh Ahmed in Prof. Avik Ghosh's group assisted with the calculation of the alloy disorder potentials and alloy scattering rates of these materials.

The alloy scattering rate for a quaternary alloy is given by [78]

$$\frac{1}{\tau}=\frac{3\pi}{8\sqrt{2}}\frac{\left(m^*\right)^{3/2}}{\hbar^4}\gamma\left(E\right)\frac{d\gamma}{dE}\Omega\left|\Delta U_Q\left(x,y\right)\right|^2 S \tag{3.9}$$

with

$$\begin{aligned}\left|\Delta U_Q\left(x,y\right)\right|^2 = {} & x\left(1-x\right)y^2\left|\Delta U_{ABD}\right|^2+x\left(1-x\right)\left(1-y\right)^2\left|\Delta U_{ABC}\right|^2 \\ & +x^2y\left(1-y\right)\left|\Delta U_{BCD}\right|^2+\left(1-x\right)^2y\left(1-y\right)\left|\Delta U_{ACD}\right|^2,\end{aligned}$$

where the ΔU_Q is the alloy disorder potential of the quaternary alloy. The ΔU's on the right-hand side of the equation represent the disorder potentials of ternary alloys. For example, the potential ΔU_{ABD} is for a ternary alloy with composition $A_{1-x}B_xD$, and the potential ΔU_{BCD} is for $BC_{1-y}D_y$. The alloy disorder potential arises due to the potential fluctuations created by the different nuclei sizes of the constituent atoms. In Eq. (3.9), m^* is the carrier effective mass, Ω is the primitive cell volume, and $\gamma\left(E\right)=E\left(1+\sigma E\right)$ describes the non-parabolic nature of the electronic band structure with E representing the carrier energy and σ describing the non-parabolicity. The ordering of atoms is described by the factor S. For completely random systems S = 1, and S = 0 for perfectly ordered systems. In our simulations, we assume S = 1. For a ternary alloy $A_{1-x}B_xC$, the disorder potential can be calculated by

$$\Delta U = \frac{bZ}{4\pi\varepsilon_0}\left(\frac{1}{r_A}-\frac{1}{r_B}\right)\exp\left(-k_s R\right), \tag{3.10}$$

where b accounts for the fact that the Thomas Fermi theory overestimates the screening in the semiconductor and has a value of 1.5 for most zinc blende binary semiconductors. Z is the valence number of A and B, ε_0 is the vacuum permittivity, and the covalent radii of the atoms A, B and C are given by r_A, r_B, and r_C, respectively. $k_s = \sqrt{4k_F / \pi a_B}$ is the Thomas Fermi screening wave number in a three-dimensional system, where a_B is the Bohr radius, and $k_F = \left(3\pi^2 N_{val}\right)^{1/3}$ is the Fermi wave number in a three-dimensional system. The valence electron density $N_{val} = 32 / a^3$, and the bond length of this ternary alloy $R = 0.5\left[xr_A + (1-x)r_B + r_C\right]$.

In Eq. (3.10), it is seen that the alloy disorder potential primarily depends on the difference in the covalent radii of the constituent atoms and their valence number. Figure 3.17 shows C_{bd} versus ΔU^2 for various III-V binary, ternary, and quaternary alloys. To make a valid comparison with quaternary alloy potentials, the ternary alloy potentials are scaled by the factor $x(1-x)$, where x is the mole fraction for atom B in AB_xC_{1-x} [22]. The C_{bd} values for the binary and ternary alloys are obtained from the Ref. [61, 76]. The multiplier thickness is assumed to be 1 μm. A larger radii difference leads to a higher alloy disorder potential. For example, InAlAs has a larger potential in comparison to AlGaAs because there is a large difference in the Al and In covalent radii whereas the Al and Ga covalent radii are similar. Also, alloys with different group V elements have a higher disorder potential in comparison to alloys with varying group III elements due to the larger valence number of group V elements.

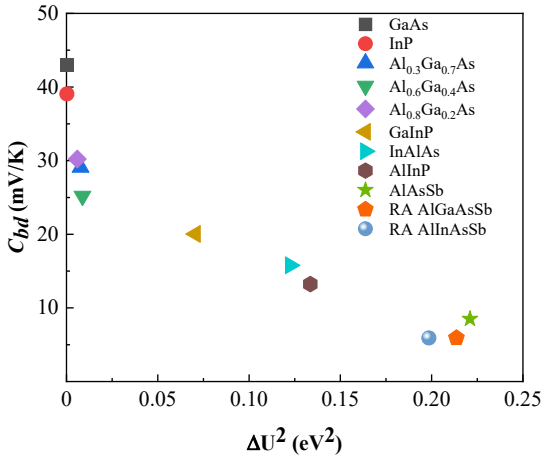

Figure 3.17. Comparison of C_{bd} vs. ΔU^2 for various III-V binary, ternary, and quaternary alloys.

We computed the alloy disorder potentials for the Sb-based quaternary alloys by using Eq. (3.10). $\Delta U = 0.46$ eV for RA AlGaAsSb and $\Delta U = 0.45$ eV for RA AlInAsSb were obtained. The ΔU^2 of the Sb-based ternary and quaternary alloys are significantly larger than other III-V alloys shown in Fig. 3.17. Consequently, the breakdown voltage of the Sb-based alloys has the weakest temperature dependence due to the large difference in the covalent radii of As and Sb atoms, which are also group V elements. The resulting higher disorder potential of these alloys leads to an increased alloy scattering rate, given by Eq. (3.9), which then dominates over the phonon scattering, leading to a weaker temperature dependence of the avalanche breakdown. The underlying factor for the temperature dependence of the avalanche breakdown is phonon scattering which the temperature-dependent phonon population can alter. A more dominant scattering mechanism, like alloy scattering, suppresses the phonon scattering mechanism which ultimately reduces the temperature dependence.

To further highlight the role of Sb atoms in the quaternary alloys, the alloy scattering rates of RA InAlAs, RA AlInAsSb, RA AlGaAsSb and RA AlAsSb are plotted in Fig. 3.18. The quaternary alloys containing Sb demonstrate much higher scattering rates compared to the ternary InAlAs.

The higher scattering rates of the quaternary alloys arise from their higher alloy disorder potentials, and potentially lower electron-phonon coupling. This is consistent with experimental observation that InAlAs has a stronger temperature dependence of avalanche breakdown than the quaternary alloys do. In the simulation, effective masses of $0.072m_0$, $0.11m_0$, $0.15m_0$, and $0.098m_0$ have been used for InAlAs, AlInAsSb, AlGaAsSb, and AlAsSb, respectively. The corresponding bandgaps for these four materials are 1.4 eV, 1.73 eV, 1.59 eV and 1.65 eV. The calculations used the lattice constant of InP (5.9117 Å), which is the substrate for all three alloys. The DA scattering rates cannot be included here since their corresponding value of S is unknown. The values can be extracted by carrying out Monte Carlo simulations with alloy scattering for these alloys and calibrating with experimental results.

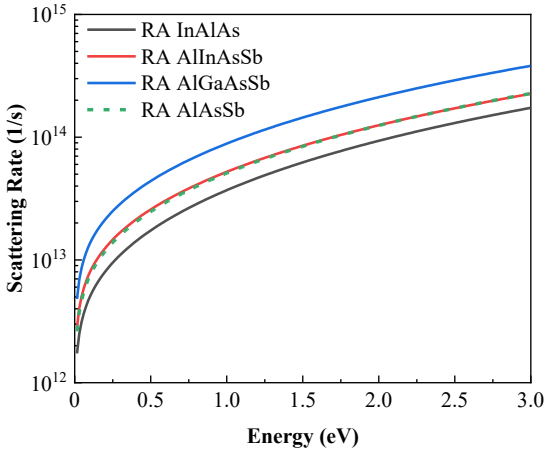

Figure 3.18. Comparison of scattering rates for random alloys of InAlAs, AlInAsSb, AlGaAsSb, and AlAsSb.

The origin of the weak temperature dependence of the quaternary Sb-based digital alloys can also be attributed to the dominance of the alloy scattering mechanism. In short-period digital alloys, the edges of the thin binary layers are not completely abrupt. There is random variation in chemical composition at the interfaces which leads to interface roughness. This results in fluctuations of the

crystal potential. In the Sb-based alloys, the alternating Sb and As binary alloys with large nuclei difference create large potential fluctuations at the interface that lead to a higher disorder potential. Consequently, the resulting higher alloy scattering rate in these quaternary digital alloys leads to their weak temperature dependence of avalanche breakdown. This mechanism potentially causes the Sb-based digital alloys to have a lower C_{bd} compared to random alloys, as shown in Fig. 3.16. This postulate can be confirmed by using Monte Carlo-based simulations in the future. In summary, phonon scattering is the dominant scattering mechanism in materials with high C_{bd}, while alloy scattering is the superior scattering mechanism in low C_{bd} materials.

3.4.3.2. Temperature dependence of bandgap energy

The impact ionization process requires carriers to attain the ionization threshold energy which depends on the bandgap energy, and the bandgap changes with temperature. The threshold energy determines the breakdown voltage of a material. Therefore, the temperature dependence of the material bandgap has a higher order effect on the breakdown voltage. The breakdown voltage temperature dependence is primarily due to the scattering processes, like phonon and alloy scattering, as mentioned earlier. Since the bandgap stability under different temperatures has some impact on the temperature dependence of avalanche breakdown, and it is instructive to investigate variation of the bandgap of Sb-based quaternary materials with temperature.

Temperature-dependent photoluminescence (PL) [79] measurements were used to study the temperature dependence of the bandgap energy for DA $Al_{0.5}In_{0.5}As_ySb_{1-y}$ lattice matched to GaSb [16], RA AlInAsSb lattice matched to InP [40], and DA AlGaAsSb lattice matched to InP [28]. PL measurements were done by our collaborators at Yeungnam University and the University of Texas at Austin. The measured bandgap energy can be fitted by the Varshni equation [80],

$$E(T) = E_0 - \frac{\alpha T^2}{T + \beta}, \tag{3.11}$$

where $E(T)$ is the energy gap at temperature T, E_0 is the energy gap at 0 K, and α and β are constants.

As shown in Figs. 3.19(a) and 3.19(b), the bandgap of DA $Al_{0.5}In_{0.5}As_ySb_{1-y}$ and RA AlInAsSb was determined in the temperature range of 95 K – 295 K and 160 K – 300 K, respectively. The data points were then fitted by the Varshni equation [80]. The temperature-dependent bandgap curves of these two Sb-based quaternary materials were compared with binary materials (including AlAs, AlSb, InAs, and InSb [81]); the Sb-based materials exhibit smaller shifts with temperature. Furthermore, the results show that both digital and random alloy growth can provide the weak temperature dependence of bandgap for $Al_xIn_{1-x}As_ySb_{1-y}$. Therefore, the growth of digital alloy itself cannot explain the bandgap stability. Figure 3.19(c) shows the temperature-dependent bandgap for DA AlGaAsSb in the temperature range of 160 K to 300 K, and the data points were fitted by the Varshni equation [80]. The same conclusion that the temperature dependence of the bandgap of the quaternary material is weaker than binary materials (including AlAs, AlSb, GaAs, GaSb [81]) can be drawn for DA AlGaAsSb.

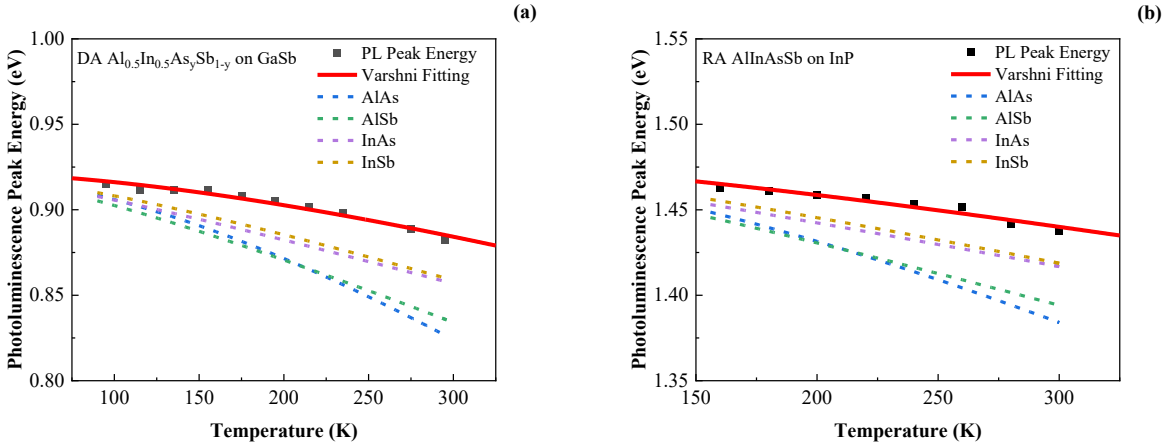

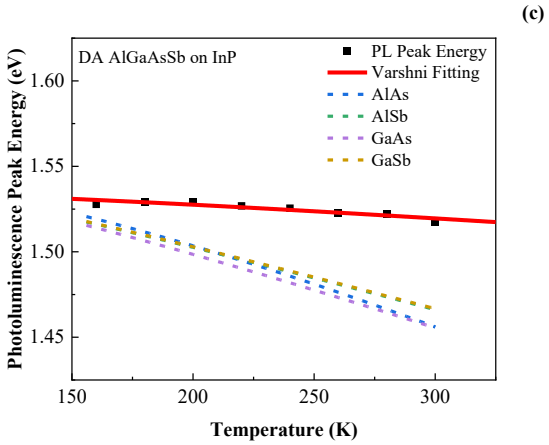

Figure 3.19. Temperature-dependent photoluminescence peaks (points) and the Varshni fitting curves (solid lines) for (a) DA $Al_{0.5}In_{0.5}As_ySb_{1-y}$ lattice matched to GaSb, (b) RA AlInAsSb lattice matched to InP, and (c) DA AlGaAsSb lattice matched to InP. The dash lines represent the Varshni fitting curves for the binary materials, including AlAs, AlSb, InAs, InSb, GaAs, and GaSb [81], and the E_0 of binary materials has been modified accordingly for a better comparison with the investigated quaternary materials.

Temperature-dependent EQE measurements [63] were carried out to investigate spectrum cutoff under different temperatures for DA $Al_{0.7}In_{0.3}As_ySb_{1-y}$ lattice matched to GaSb [44]. As shown in Fig. 3.20, EQE measurements were carried out in the temperature range of 258.15 K to 298.15 K for DA $Al_{0.7}In_{0.3}As_ySb_{1-y}$. Based on shifts in the response near the cutoff, the bandgap variation with temperature was determined to be 0.29 meV/K, consistent with the PL measurements. In summary, temperature-dependent PL and EQE measurements demonstrate weak bandgap variation with temperature for $Al_xIn_{1-x}As_ySb_{1-y}$ and $Al_xGa_{1-x}As_ySb_{1-y}$ material systems, irrespective of growth method. The temperature dependence of the material bandgap is primarily attributed to electron-phonon interactions [82] that broaden the material energy states and result in the creation of energy states within the bandgap. The effect of thermal expansion on the temperature dependence is very small for covalent compounds [83]. The weak temperature dependence of the bandgap of these Sb-based quaternary alloys most likely arises from the weak electron-phonon coupling in these materials. The weak coupling results in a small broadening of

the energy states, and hence, fewer energy levels created within the bandgap. Such weak temperature dependence of the material bandgap may somewhat lower the C_{bd}, primarily due to a higher-order effect. On the other hand, a stronger electron-phonon coupling will most likely cause some increase in C_{bd}. Further investigations are needed to be carried out to determine the exact contribution of electron-phonon interactions on C_{bd}.

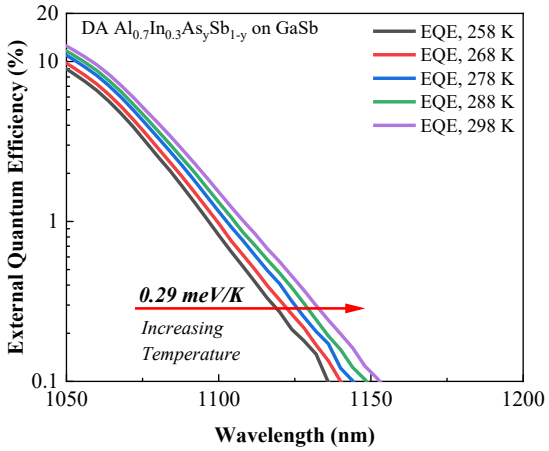

Figure 3.20. Temperature-dependent external quantum efficiency for DA $Al_{0.7}In_{0.3}As_ySb_{1-y}$ lattice matched to GaSb.

3.4.4. Conclusion

Temperature dependence of avalanche breakdown has been investigated for DA $Al_{0.85}Ga_{0.15}As_{0.56}Sb_{0.44}$, RA $Al_{0.85}Ga_{0.15}As_{0.56}Sb_{0.44}$, and RA $Al_{0.79}In_{0.21}As_{0.74}Sb_{0.26}$. I observed weak dependence of the avalanche breakdown voltage on temperature for the Sb-based quaternary materials. Temperature-dependent photoluminescence and external quantum efficiency measurements reveal weak temperature dependence of the bandgap. Modeling supports that these quaternary alloys have high alloy scattering rates dominating phonon scattering mechanisms that reduce the temperature dependence of the avalanche breakdown. This weak temperature

dependence simplifies the temperature or reverse bias control circuits while maintaining a constant multiplication gain in an optical receiver.

4. Digital Alloy InGaAs Absorber for Extended Short-Wavelength Infrared Photodetection

4.1. Motivation

For the photodetectors working in the SWIR spectral region, Si with the cut-off wavelength at 1100 nm and InGaAs with the cut-off wavelength at 1680 nm are commercially available absorption materials. Recently, more work has been done in the extended SWIR spectral region, and conventional Si and InGaAs cannot satisfy the application requirements. There are commercially mature absorption materials such as InAs [15], $Hg_{0.7}Cd_{0.3}Te$ [14], and strained InGaAs, which might be used for extended SWIR applications, but some inherent limitations exist. The operation of InAs and $Hg_{0.7}Cd_{0.3}Te$ photodetectors requires cryogenic cooling due to the high dark current resulting from their narrow bandgaps, making it challenging to develop compact optical receivers based on these two materials. Strained InGaAs photodetectors are limited by the inherent high dark current originating from the lattice mismatch. This chapter demonstrated a material system with the bandgap in the extended SWIR spectral region by utilizing the digital alloy growth technique.

Semiconductor quantum wells and superlattices have been widely used in various electronic and optoelectronic devices [27, 84-86]. With increasingly mature MBE growth techniques, atomic-level control of the epitaxial structure of multiple quantum wells (MQWs) has become achievable. The tuning of width, composition, and asymmetry of the MQW structure enables deterministic optical and electronic material parameters [71, 86, 87]. As mentioned in Chapter 3, digital alloy-grown short-period superlattice structures have been successfully employed for the Sb-based quaternary alloys with high performances. Additionally, the DA growth technique can significantly modify the material characteristics of InAlAs and InGaAs ternary materials lattice

matched to InP. The reduction of the excess noise in DA InAlAs APDs has been experimentally and theoretically demonstrated [31, 67]. Compared to conventional RA InAlAs, wide bandgap tunability is also obtained for DA InAlAs with different periodic structures [32]. These new features of DA InAlAs can potentially enhance the performance of APDs, particularly those used for telecommunications.

Like InAlAs, the ternary alloy InGaAs can be grown lattice matched to InP, and RA InGaAs has a nominal bandgap energy at 0.74 eV. Although Rockwell *et al*. [87] have shown that the cutoff wavelength of 10 monolayer (ML) DA InGaAs APDs can be increased to be greater than 1900 nm. The reported results are primarily limited to the investigation of the single periodic structure at the APD level, and there is no systematic material investigation of DA InGaAs with different periodic structures. Furthermore, the previous growth of DA InGaAs p^+-i-n^+ APDs requires the addition of bismuth (Bi) which is not a necessary composition in the growth of other similar ternary materials such as DA InAlAs [32]. Therefore, it is hard to conclude whether the bandgap engineering of DA InGaAs only results from the digital alloy structure or from both bismuth addition and the digital alloy structure.

The systematic investigation of DA InGaAs without bismuth is necessary due to its photodetection capability at the extended SWIR spectral region. Compared to InAs, $Hg_{0.7}Cd_{0.3}Te$, and strained InGaAs, DA InGaAs exhibits the tunable bandgap and the better lattice-matching condition. It is expected that photodetectors with the DA InGaAs absorber have the potential to achieve high performance in extended SWIR applications.

In this chapter, a series of different DA InGaAs samples were studied without bismuth being used as a surfactant. They were characterized by scanning transmission electron microscopy (STEM), high-resolution X-ray diffraction (HR-XRD), atomic force microscopy (AFM), and

photoluminescence (PL) measurements. The optical constants were then extracted via the ellipsometry based on the Kramers–Kronig consistent basis spline (B-Spline) fitting approach. The band structures were simulated via an environment-dependent tight binding model [31] to provide insights into the bandgap tunability of the DA InGaAs. Increasing research interests in photodetection at the extended SWIR spectral region make such material investigation indispensable [1, 2, 4].

4.2. Results and discussion

4.2.1. Sample structures and characterizations

Our collaborator, Dr. Baolai Liang, at the University of California – Los Angeles, helped with the material growth and characterizations. The structure details of investigated samples are shown in Fig. 4.1(a). Four DA InGaAs samples were grown with period thicknesses of 4.5 ML, 6 ML, 8 ML, and 10 ML, respectively. A 200-nm DA InGaAs layer was grown at 400 ℃ with repeated InAs/GaAs periodic structures for each sample. One control sample with a 200-nm RA InGaAs layer was also grown at 400 ℃ to determine the effect of the digital alloy structure on the bandgap tunability.

The high-angle annular dark-field STEM image for the 6 ML DA InGaAs sample showed well-defined superlattice fringes in the top 200-nm DA layer, as shown in Fig. 4.1(b). The DA InGaAs layer is uniform without dislocations, and the period thickness measured by the STEM is approximately 6 ML.

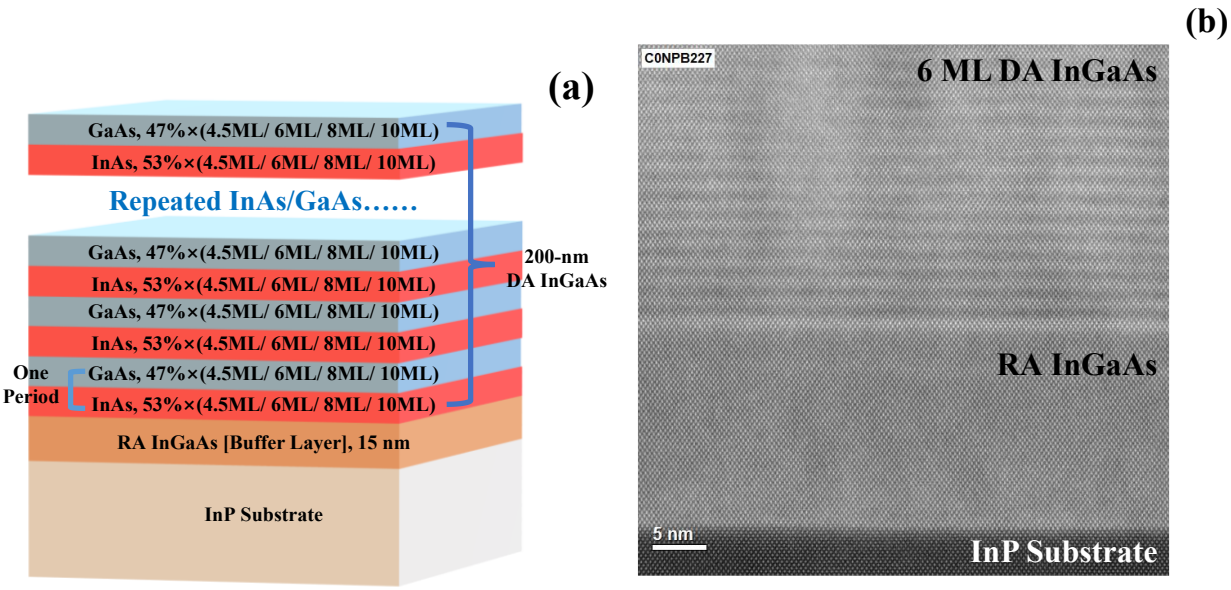

Figure 4.1. (a) Epitaxial structure of DA InGaAs samples with period thicknesses at 4.5 ML, 6 ML, 8 ML, or 10 ML. (b) High-angle annular dark-field STEM image of the 6 ML DA InGaAs sample, where 200-nm 6 ML DA InGaAs layer, 15-nm RA InGaAs layer, and InP substrate are sequentially shown from top to bottom.

The morphology analysis of these samples was carried out using AFM at room temperature via a Bruker Dimension FastScan in tapping mode, as shown in Fig. 4.2. The RA InGaAs (400 °C) sample exhibits a root mean square (RMS) roughness of 0.70 nm, and the DA InGaAs samples exhibit more rough films with spotty, strain-relaxed-like surfaces, as demonstrated in the AFM images with RMS roughness at 0.93 nm, 1.27 nm, 1.65 nm, and 1.78 nm for 4.5 ML, 6 ML, 8 ML, and 10 ML DA InGaAs samples, respectively. The RMS roughness gradually increases as the period thickness increases since the strain mismatch between the InAs and GaAs increases. The rougher surface indicates that the material quality drops when the DA InGaAs sample is grown with a thicker periodic structure.

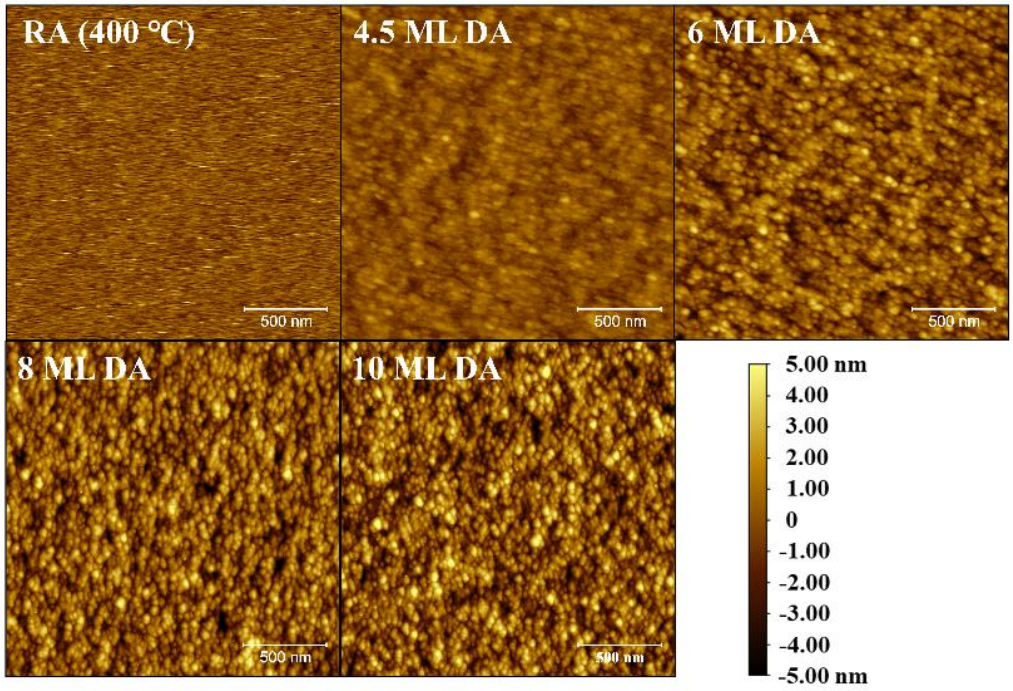

Figure 4.2. AFM images of RA InGaAs (400 ℃), 4.5 ML DA InGaAs, 6 ML DA InGaAs, 8 ML DA InGaAs, and 10 ML DA InGaAs samples.

Figures 4.3(a) and 4.3(b) summarize HR-XRD omega-2theta scans for all RA and DA samples. As for the RA InGaAs (400 ℃) sample, clear thickness fringes can be resolved, and the composition is determined to be $In_{0.535}Ga_{0.465}As$, demonstrating a composition mismatch smaller than 0.5%. As for the DA InGaAs samples, the $+1^{st}$ and -1^{st} satellite peaks can be observed for the 4.5 ML, 6 ML, and 8 ML samples, while the $+2^{nd}$ and -2^{nd} satellite peaks can be observed for the 10 ML sample. These satellite peaks indicate the coherence and interface sharpness of the DA samples.

When the period thickness increases from 4.5 ML to 10 ML, the separation between $+1^{st}$ and -1^{st} satellite peaks decreases, and the intensities of the $+1^{st}$ and -1^{st} satellite peaks increase, indicating enhanced coherence of the XRD diffraction signal for DA InGaAs with larger period thickness. The period thicknesses were estimated based on the satellite peak positions, matching well with the designed values.

Figure 4.3(c) expands the HR-XRD spectra to show the variation of the 0th peak of the DA InGaAs samples with respect to the InP substrate signal. The 0th peaks were measured to be at +200, +80, -180, and -220 arcsec relative to the InP substrate peak for 4.5 ML, 6 ML, 8 ML, and 10 ML DA InGaAs samples, and the average indium compositions were then determined to be 51.9%, 52.7%, 54.1%, 54.4%, respectively. It is concluded that the period thickness impacts the strain and the average indium composition. To obtain thick DA InGaAs films with good material quality, it is necessary to carefully design the period thickness and optimize the growth condition to balance the strain.

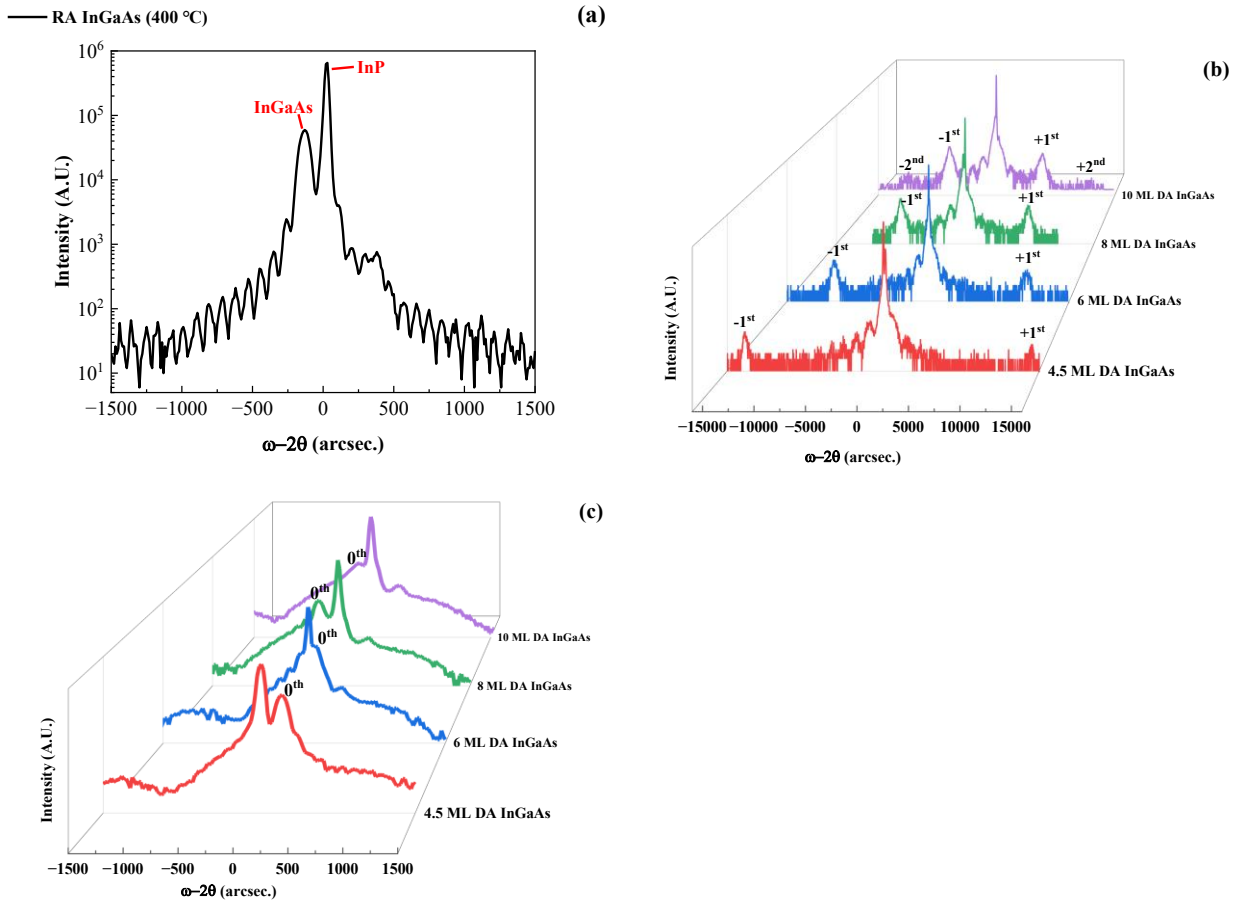

Figure 4.3. HR-XRD omega-2theta scans of (a) RA InGaAs (400 °C), (b) 4.5 ML DA InGaAs, 6 ML DA InGaAs, 8 ML DA InGaAs, and 10 ML DA InGaAs samples at room temperature. (c) Expanded HR-XRD spectra to show the splitting between the 0th peaks of the DA InGaAs samples and the InP substrate.

4.2.2. Photoluminescence spectra

PL measurements have been carried out on the RA InGaAs (400 °C) and DA InGaAs samples at cryogenic and room temperatures. The PL spectra measured at 7 K with an excitation intensity of 3000 W/cm^2 and the PL spectra measured at 293 K with an excitation intensity of 1500 W/cm^2 are shown in Figs. 4.4(a) and 4.4(b), respectively. Due to the high PL peak intensity of the 4.5 ML DA InGaAs, the PL spectra of the 8 ML and 10 ML DA InGaAs cannot be shown clearly. Therefore, the PL spectra at 7 K and room temperature were normalized, as shown in Fig. 4.5. Some features can be obtained after careful analysis of these spectra.

Figure 4.5 indicates that the PL peaks exhibit redshift as the period thickness increases. The PL peaks at 7 K are determined to be 1570 nm (0.790 eV), 1650 nm (0.751 eV), 1710 nm (0.725 eV), and 1820 nm (0.681 eV); and the PL peaks at room temperature are determined to be 1690 nm (0.734 eV), 1750 nm (0.708 eV), 1900 nm (0.653 eV), and 1950 nm (0.636 eV) for RA InGaAs (400 °C), 4.5 ML DA InGaAs, 6 ML DA InGaAs, and 8 ML DA InGaAs samples, respectively. The PL intensity of 10 ML DA InGaAs is too weak to determine the peak position accurately. The PL peak can be effectively shifted from 1690 nm (0.734 eV) for the RA InGaAs (400 °C) to 1950 nm (0.636 eV) for the 8 ML DA InGaAs at room temperature. Such prominent redshift is explained by the band structure engineering originating from the DA growth, and the redshift amplitude depends on the DA period thickness. Therefore, by only changing from RA growth to DA growth, the conventional InGaAs material system has been demonstrated with strong bandgap energy tunability (~ 260 nm) with the emission spectrum extended to ~ 2 μm. It is lattice matched to InP substrates, making it a promising absorber candidate for extended photodetection in the SWIR spectral region.

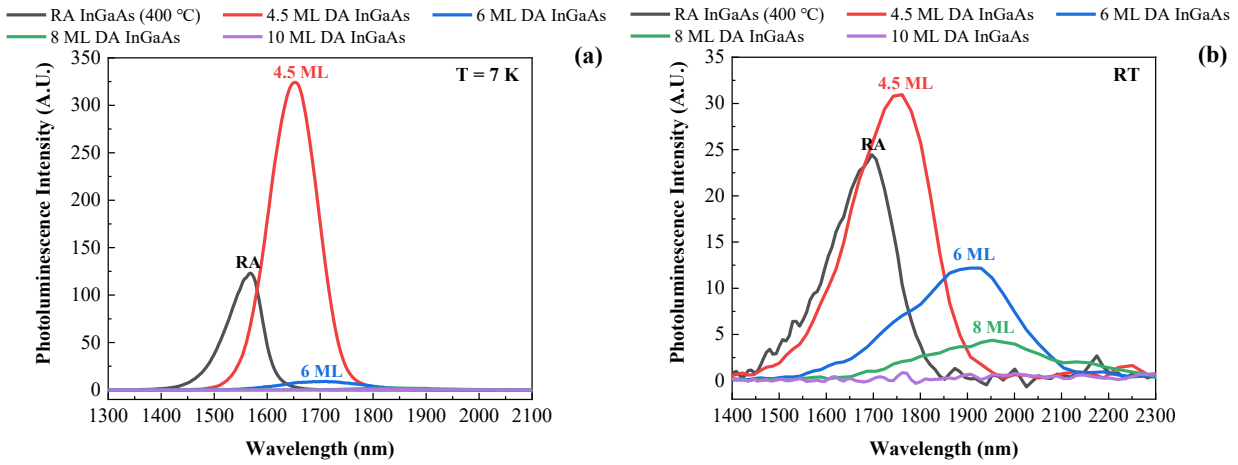

Figure 4.4. PL spectra of RA InGaAs (400 °C), 4.5 ML DA InGaAs, 6 ML DA InGaAs, 8 ML DA InGaAs, and 10 ML DA InGaAs samples at (a) 7 K and (b) room temperature. Normalized PL spectra are shown in Fig. 4.5.

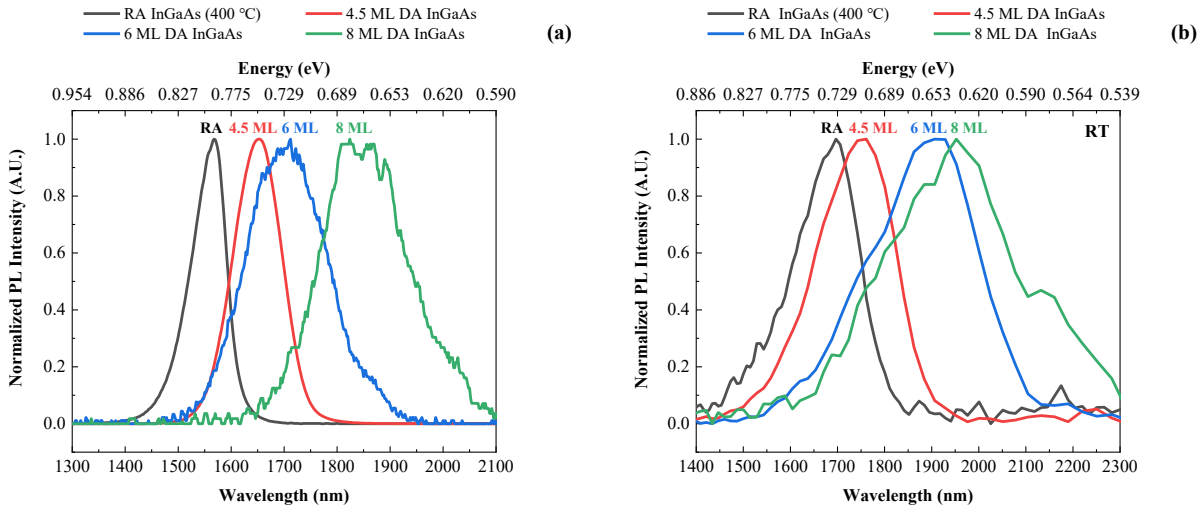

Figure 4.5. Normalized PL spectra of RA InGaAs (400 ℃), 4.5 ML DA InGaAs, 6 ML DA InGaAs, and 8 ML DA InGaAs at (a) 7 K and (b) room temperature.

As shown in Fig. 4.4, the 4.5 ML DA InGaAs sample has a higher PL intensity than the RA InGaAs sample, and the other DA InGaAs samples exhibit dramatically decreased PL intensity as the period thickness increases. In particular, the PL emission from the 10 ML sample is barely discernible, even at 7 K. The DA structure of the 4.5 ML sample likely enhances the quantum confinement of carriers, leading to enhanced carrier recombination and luminescence efficiency.

However, when the period thickness increases from 6 ML to 10 ML, the samples have more defects and non-radiation trap centers, leading to a drop in the PL intensity.

The excitation-intensity-dependent PL spectra were measured and the PL peak energy and full width at half maximum (FWHM) under different excitation intensities were extracted, as shown in Fig. 4.6. For RA InGaAs (400 ℃), 4.5 ML DA InGaAs, and 6 ML DA InGaAs samples, when the excitation intensity increases from 30 W/cm^2 to 3000 W/cm^2, the PL peaks shift 7 meV, 26 meV, and 44 meV, and the linewidth broadens 23 meV, 33 meV, and 39 meV, respectively.

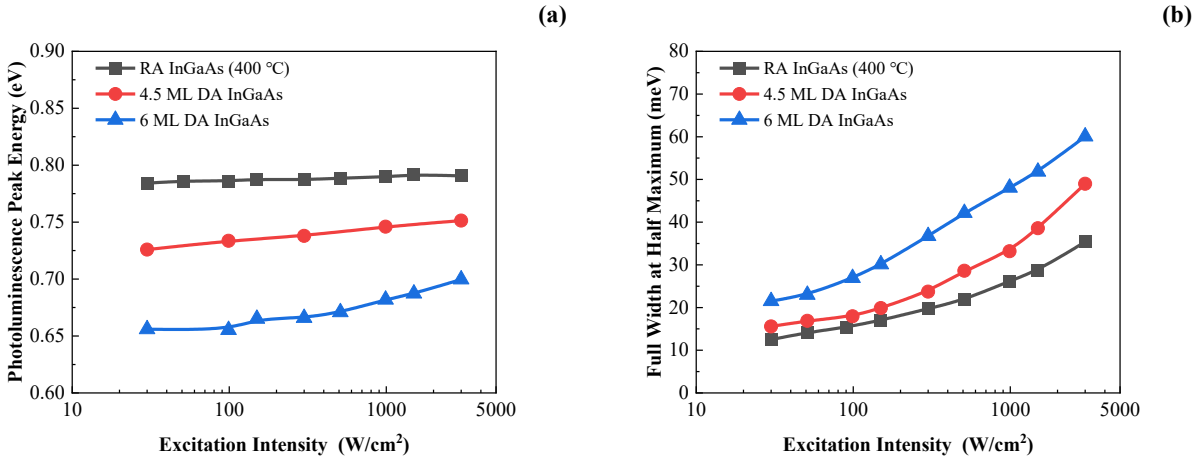

Figure 4.6. (a) PL peak energy and (b) FWHM measured under different laser excitation intensity at 7 K for RA InGaAs (400 ℃), 4.5 ML DA InGaAs, and 6 ML DA InGaAs samples.

The temperature-dependent PL spectra were measured to verify the carrier localization effect further. Figure 4.7 shows the temperature-dependent PL peak energy from 10 K to 280 K for RA InGaAs (400 ℃), 4.5 ML DA InGaAs, and 6 ML DA InGaAs samples. The symbols represent the measured PL peak positions, and they can be fitted by the Varshni equation.

A good agreement was obtained for the RA InGaAs (400 ℃) sample. For the 4.5 ML DA InGaAs sample, the measured and calculated bandgap curves match well down to 120 K, and the discrepancy occurs in the temperature range from 10 K to 120 K, where an “S” shape dependence of the PL peak energy on temperature can be observed. Such an “S” shape behavior is generally

regarded as a signature of strong carrier localization. A similar conclusion can be drawn for the 6 ML DA InGaAs sample, where the discrepancy occurs in the temperature range from 10 K to 150 K, demonstrating a stronger carrier localization effect than the 4.5 ML DA InGaAs sample. In summary, the carrier localization effect becomes more pronounced as the period thickness increases.

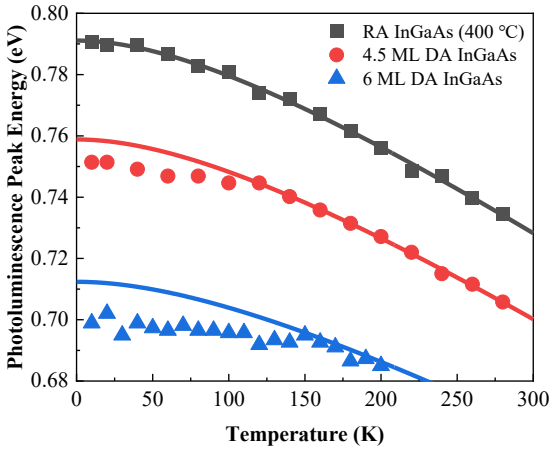

Figure 4.7. Temperature-dependent photoluminescence peaks (points) and the Varshni fitting curves (solid lines) for RA InGaAs (400 °C), 4.5 ML DA InGaAs, and 6 ML DA InGaAs samples.

4.2.3. Extraction of optical constants via ellipsometry

Variable-angle spectroscopic ellipsometry was employed to study the absorption coefficients and the complex refractive indices of DA InGaAs with different periodic structures. The DA InGaAs and RA InGaAs (400 °C) samples were measured with incident angles from 50° to 70° and 5° steps, and the measured ψ and Δ are shown in Fig. 4.8. Then, a multilayer model is built to analyze the polarization change of the reflected beam. As for the InP substrate, its optical constants come from the literature-based CompleteEASE library. As for the bottom 15-nm RA InGaAs layer grown at 485 °C, since this layer has similar optical properties as 200-nm DA/RA InGaAs (400 °C), it was essential to obtain precise optical constants of this 15-nm RA InGaAs layer to reduce the

fitting uncertainty. Therefore, a new sample with a 215-nm RA InGaAs layer grown at 485 ℃ on the InP substrate was grown, and the optical constants of RA InGaAs (485 ℃) was firstly obtained from this sample via the Kramers–Kronig consistent B-Spline fitting method.

After the investigation of RA InGaAs (485 ℃), its optical constants were substituted into multilayer models of RA InGaAs (400 ℃), 4.5 ML, 6 ML, 8 ML, and 10 ML DA InGaAs samples to represent the bottom 15-nm buffer layer. The 200-nm investigated DA/RA InGaAs layers were modeled via the B-Spline method. In addition, a thin RA InGaAs oxide layer on the top was added into the consideration due to the samples' surface oxidization effect. Finally, the simulated ψ and Δ curves agree well with measured ψ and Δ curves, as shown in Fig. 4.8.

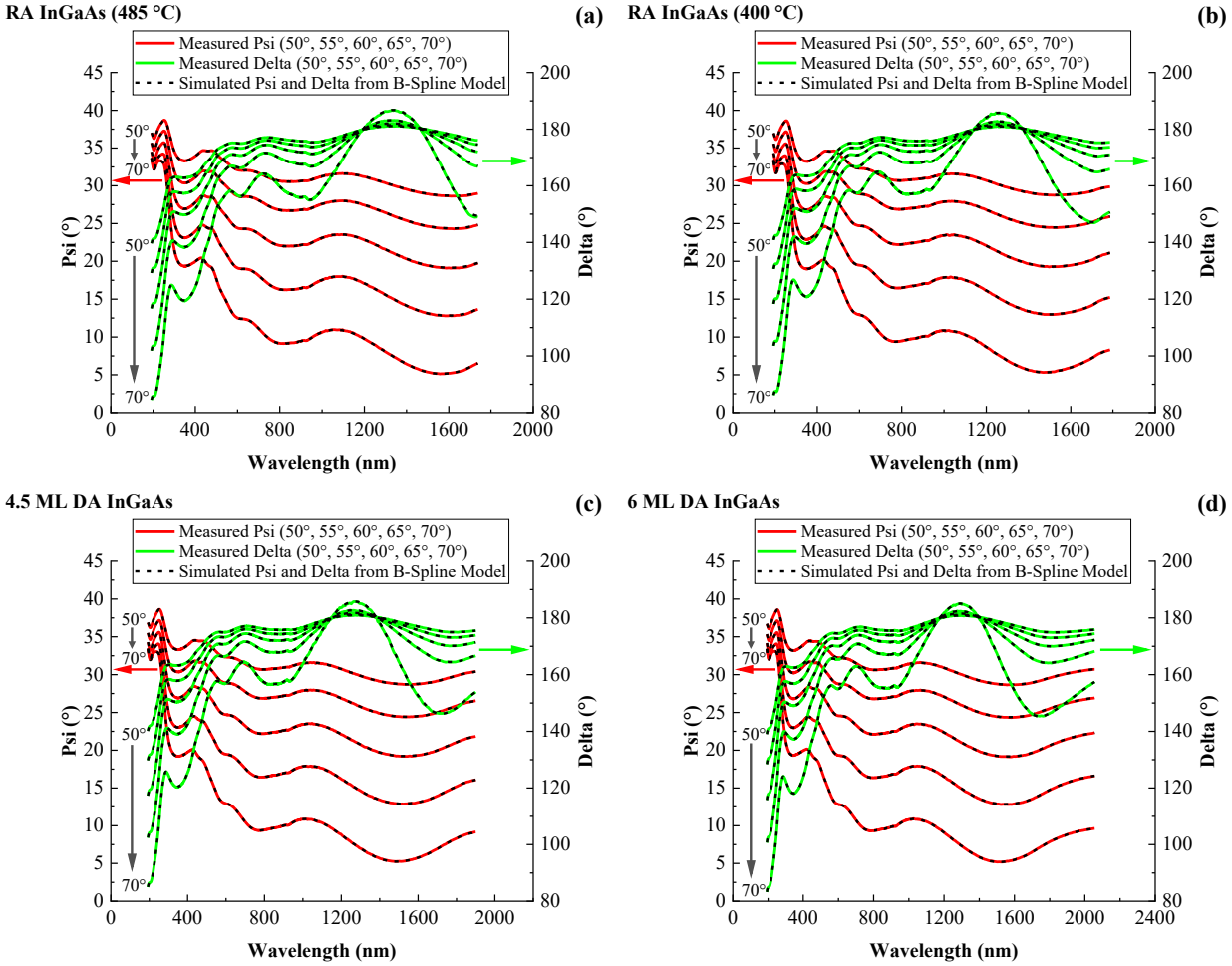

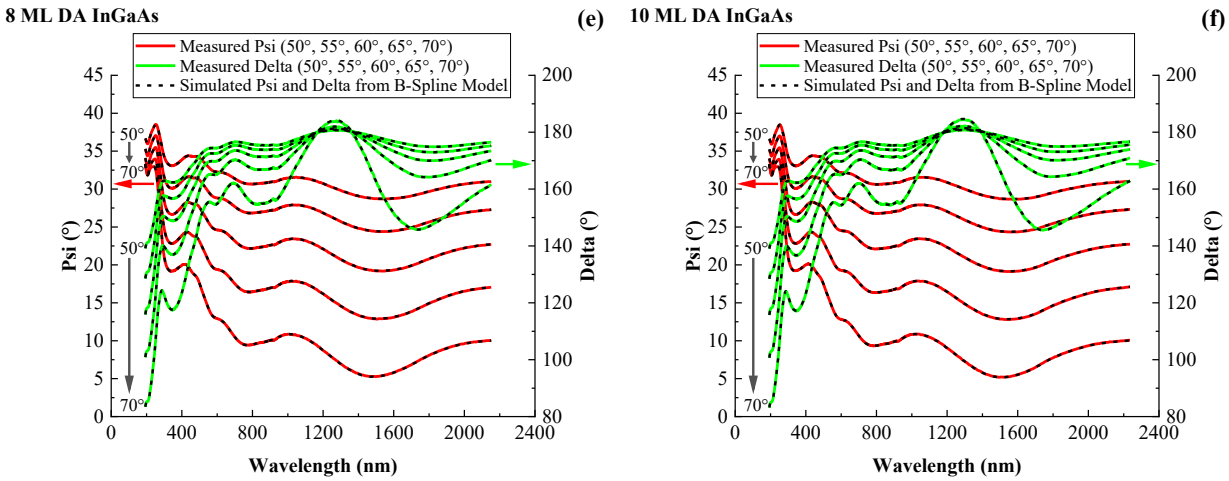

Figure 4.8. Variable-angle spectroscopic ellipsometry data with 50° - 70° incident angle of (a) RA InGaAs (485 ℃), (b) RA InGaAs (400 ℃), (c) 4.5 ML DA InGaAs, (d) 6 ML DA InGaAs, (e) 8 ML DA InGaAs, and (f) 10 ML DA InGaAs samples. Solid lines are measured ψ (red) and Δ (green), and black dash lines are simulated ψ and Δ based on the B-Spline fitting model.

The optical constants were successfully extracted from 193 nm to the region near the cut-off wavelength. The comparison of absorption coefficients between RA InGaAs (485 ℃), RA InGaAs (400 ℃), 4.5 ML DA InGaAs, 6 ML DA InGaAs, 8 ML DA InGaAs, and 10 ML DA InGaAs are shown in Fig. 4.9 as solid lines. The absorption coefficients were determined to be 398 cm^{-1}, 831 cm^{-1}, and 1230 cm^{-1} at 2 μm for 6 ML, 8 ML, and 10 ML DA InGaAs. The dark dashed line represents the literature-based absorption coefficient of the typical RA InGaAs [88]. There is a good agreement of absorption coefficients between measured RA InGaAs (485 ℃) and published RA InGaAs [88]. The absorption coefficient curve in the region near the cut-off wavelength progressively shifts to a longer wavelength (lower energy) with increasing period thickness, the same trend as the PL results shown in Fig. 4.5.

The absorption coefficient (α) and the extinction coefficient (κ) have the relationship of $\alpha = 4\pi\kappa/\lambda$, where λ is the wavelength, and the extinction coefficient and refractive index (n) have

Kramers–Kronig relations. The refractive indices and extinction coefficients were determined for RA/DA InGaAs samples, as shown in Fig. 4.10.

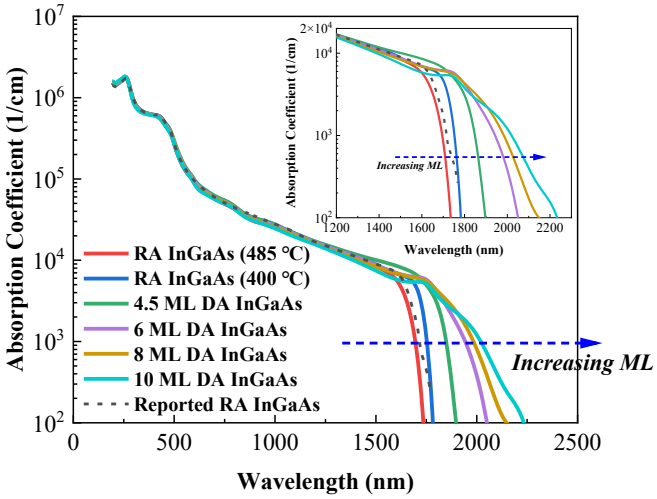

Figure 4.9. Comparison of absorption coefficients of RA InGaAs (485 °C), RA InGaAs (400 °C), 4.5 ML DA InGaAs, 6 ML DA InGaAs, 8 ML DA InGaAs, 10 ML DA InGaAs (solid lines), and literature-based RA InGaAs (dash line) [88]. The inset zooms in the absorption coefficient curves at the longer wavelength range.

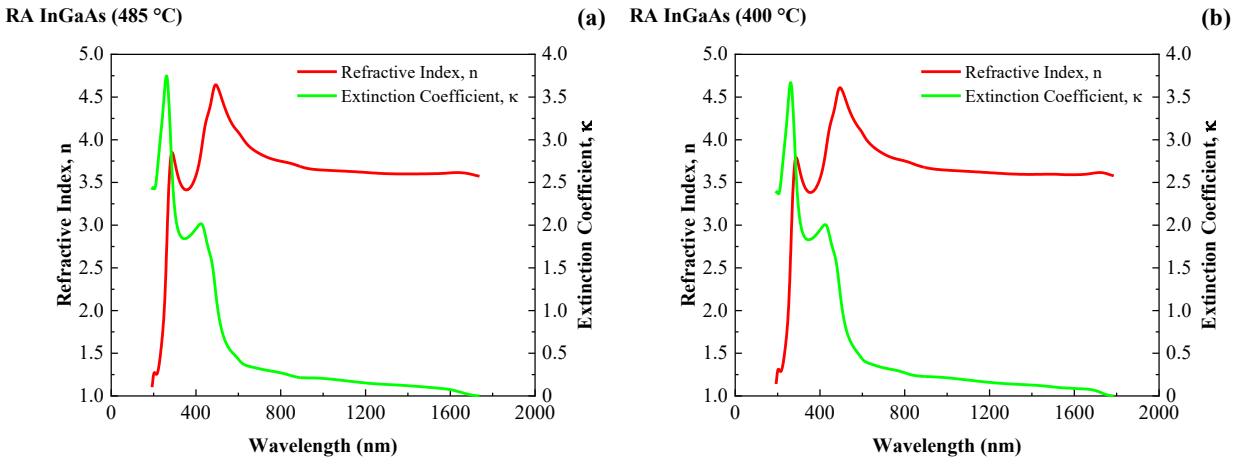

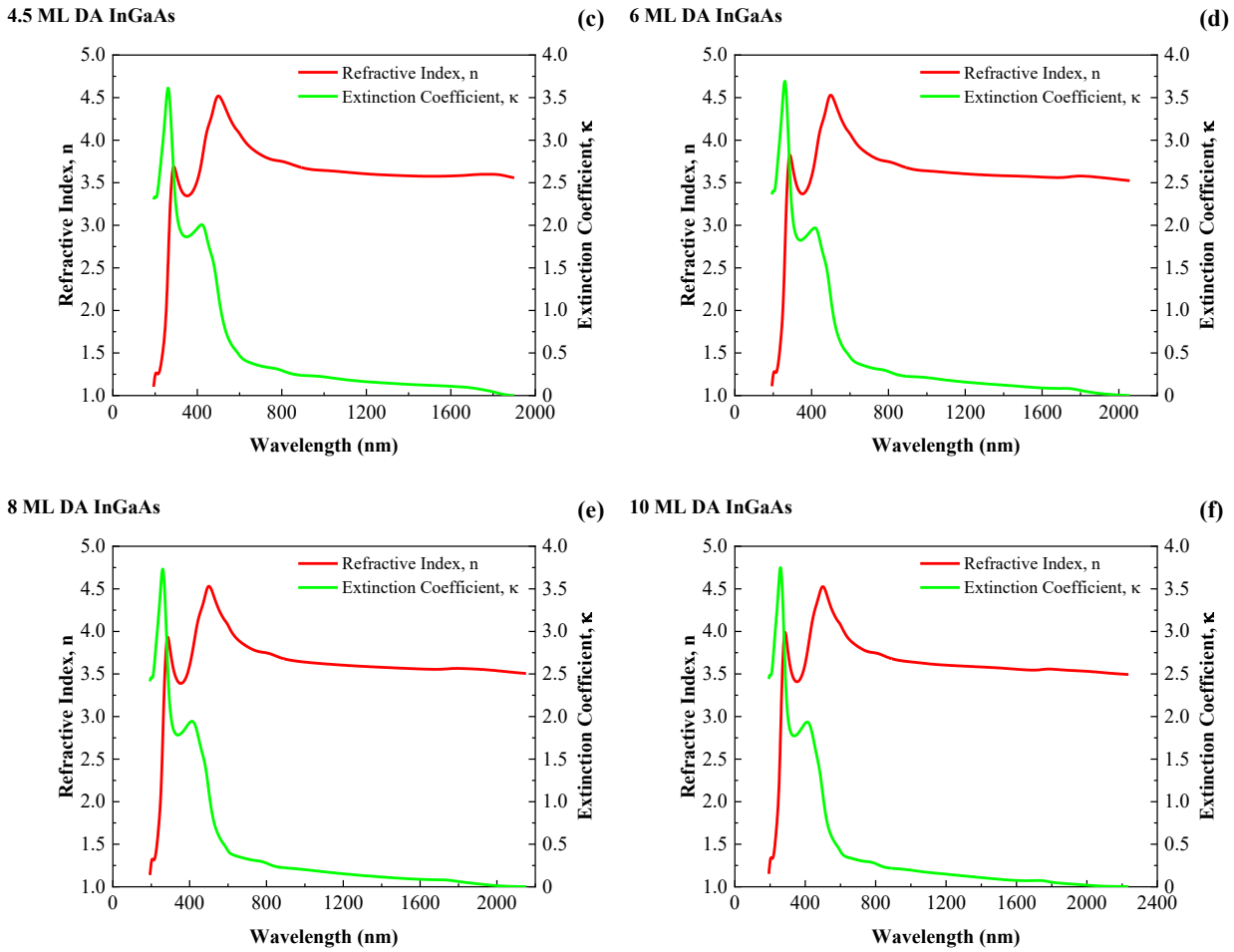

Figure 4.10. Refractive indices (red) and extinction coefficients (green) in a wide wavelength range of (a) RA InGaAs (485 °C), (b) RA InGaAs (400 °C), (c) 4.5 ML DA InGaAs, (d) 6 ML DA InGaAs, (e) 8 ML DA InGaAs, and (f) 10 ML DA InGaAs.

4.3. Band structure simulation

An accurate band structure spanning the full Brillouin zone is needed to understand the underlying physics of the InGaAs bandgap engineering. Our collaborator, Dr. Jiyuan Zheng, at Tsinghua University helped with the simulation. The environment-dependent tight binding (EDTB) model [89, 90] was utilized, which can accurately compute the band structure of alloys. Material chemistry at interfaces and surfaces cannot be handled well by traditional tight binding models since they are only calibrated to bulk band structure around the high symmetry points [90].

Thus, these models are not transferable to highly strained interfaces/surfaces that have strong impact from the surrounding environment on the material properties. However, the EDTB model parameters are directly environment-dependent. These are calibrated to state-of-the-art band structure generated using hybrid density functional theory [91] and their underlying orbital-resolved wavefunctions. The model incorporates environmental effects, like strain and interface-induced changes, by tracking neighboring atomic coordinates, bond angles, and bond lengths. Our model used an accurate band structure of unstrained and strained bulk III-V materials/alloys as fitting targets. We have previously demonstrated that our model can match hybrid functional band structures of bulk, strained, and superlattice systems [30, 89, 92].

The band structures of 4 ML, 6 ML, 8 ML, and 10 ML DA InGaAs were calculated based on the EDTB model, as shown in Fig. 4.11. The calculated bandgaps and measured PL peaks at room temperature agree well, as shown in Fig. 4.12. The band structure of DA InGaAs is affected by the strain caused by the lattice mismatch between InAs and GaAs, and the strain experienced by InAs and GaAs varies with the period thickness. As the period thickness decreases, GaAs experiences stronger tensile strain, and InAs experiences greater compressive strain.

The strain effects induced by the variation in period thickness play a vital role in determining the bandgap of DA InGaAs. A thinner period thickness leads to a broader bandgap overall, and this widening effect can be attributed to the increased tensile strain in GaAs. Our group's previous research indicates that the increased compressive strain in InAs has a relatively minimal impact on its band structure [31]. Therefore, the bandgap widens as period thickness decreases due to a stronger tensile strain experienced by GaAs. Conversely, increased thickness weakens the strain effect on both InAs and GaAs. As a result, the bandgap of DA InGaAs decreases. This reduction

occurs because the strain-induced bandgap widening effect diminishes when the period thickness exceeds a critical threshold.

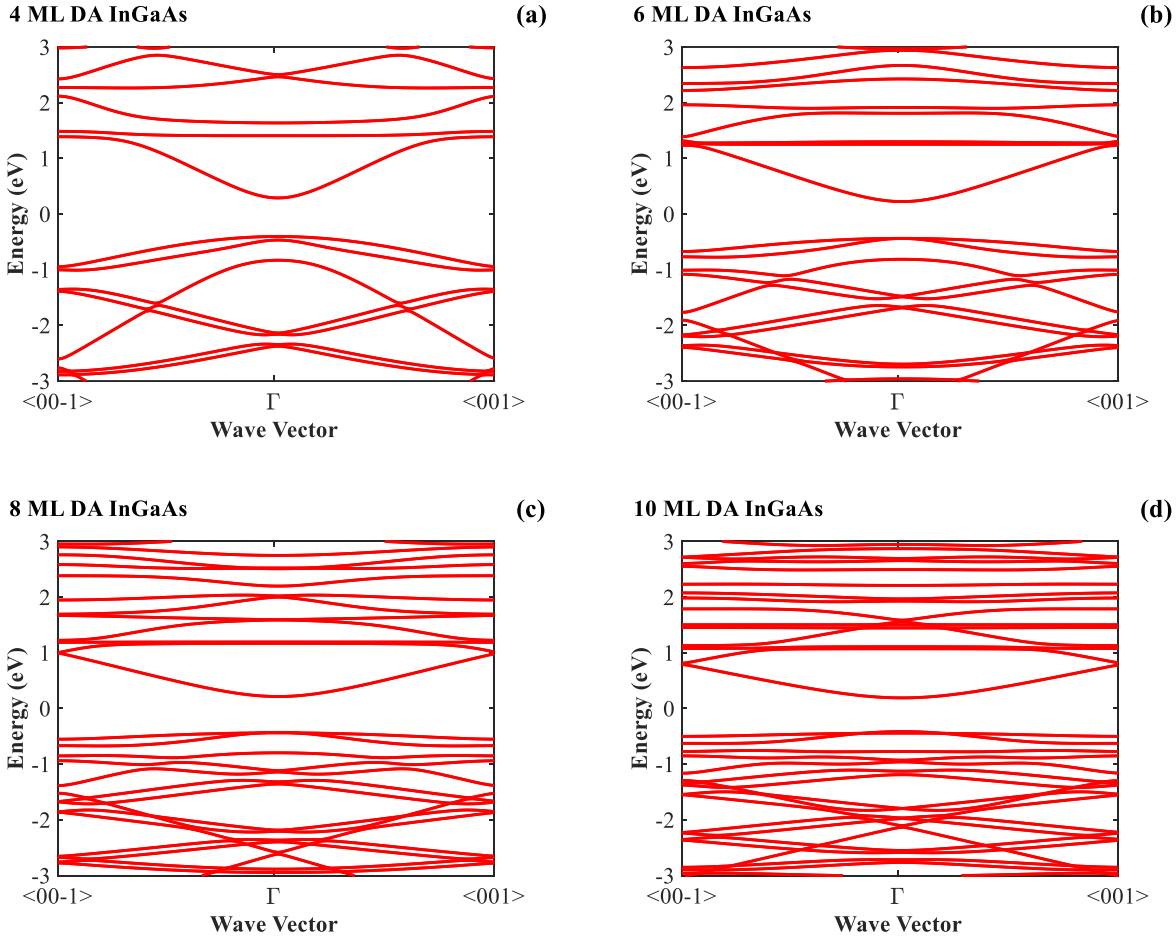

Figure 4.11. Band structures of (a) 4 ML, (b) 6 ML, (c) 8 ML, and (d) 10 ML DA InGaAs.

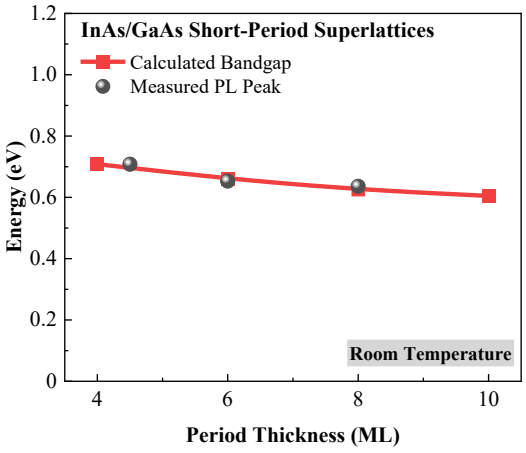

Figure 4.12. Comparison between calculated bandgaps and measured PL peaks at room temperature for DA InGaAs.

4.4. Conclusion

A series of DA-grown InAs/GaAs samples with different period thicknesses ranging from 4.5 to 10 ML have been investigated. AFM, HR-XRD, and STEM measurements were carried out to reveal the morphologic and structural characteristics. The PL results exhibit a wide bandgap tunability introduced by the DA structure. The optical constants of the DA InGaAs were extracted via ellipsometry based on the Kramers-Kronig consistent B-Spline fitting method, exhibiting the absorption coefficients of 398 cm^{-1}, 831 cm^{-1}, and 1230 cm^{-1} at 2 μm for 6 ML, 8 ML, and 10 ML DA InGaAs. The corresponding absorption edge is shifted to the longer wavelengths for DA InGaAs with a thicker periodic structure. The calculated bandgap via an environment-dependent tight-binding model of DA InGaAs agrees well with the measured PL peak, and the simulated band structures are beneficial for a physical understanding of the effect of the digital alloy structure on band structure engineering. In summary, systematic investigations have been carried out for the DA InGaAs material system, and its absorption spectral region has the potential to be effectively

extended to be more than 2 μm, paving the way for the future utilization of this conventional absorption material system grown by the digital alloy growth technique in SWIR applications.

5. Low-Noise, Strong-Temperature-Stability SACM APDs on InP Substrates

The Sb-based multipliers have been demonstrated with low excess noise and robust performance in a wide temperature range via a series of electrical and optical characterizations under room and cryogenic temperatures in Chapter 3. The DA InGaAs absorber has been demonstrated with the tunable absorption window at the extended SWIR spectral region via a series of material characterizations in Chapter 4. Due to the bandgap limitation of the investigated $Al_{0.85}Ga_{0.15}As_{0.56}Sb_{0.44}$ and $Al_{0.79}In_{0.21}As_{0.74}Sb_{0.26}$, these high-performance multipliers cannot be used for SWIR applications with the p^+-i-n^+ APD structure; instead, the SACM APD structure, paired with InP substrate-based absorbers, is utilized. In Chapter 5, RA InGaAs, GaAsSb, and DA InGaAs have been employed as the absorber materials, paired with Sb-based multipliers, in the SACM APD structures for applications in the SWIR and extended SWIR spectral regions.

5.1. InGaAs/AlInAsSb SACM APDs

5.1.1. Motivation

Under varying ambient conditions, a lower *k*-value and weaker temperature sensitivity are preferable for APDs. $Al_xIn_{1-x}As_ySb_{1-y}$ APDs lattice matched to GaSb have been demonstrated with low excess noise [16] comparable to Si and extremely weak temperature sensitivity. A high gain-bandwidth product is expected for these APDs, but the response speed is limited by the highly doped GaSb substrates, leading to a low RC-limited bandwidth [18]. To address the bandwidth limitation, p^+-i-n^+ $Al_{0.79}In_{0.21}As_{0.74}Sb_{0.26}$ APDs have been grown on semi-insulating InP substrates, and these APDs also exhibited low excess noise [40] and weak temperature dependence of avalanche breakdown [93], making $Al_xIn_{1-x}As_ySb_{1-y}$ lattice matched to InP a promising multiplier material. The advantages of InP-substrate-based APDs for SWIR applications have been widely reported [94-98].

The commonly used telecommunications APD structure consists of SACM regions. InGaAs is the material of choice for the absorption region [58, 98, 99] to obtain better material quality, although InGaAs/GaAsSb type-II superlattices have proved useful for operation at longer wavelengths, e.g., 2 μm [100]. Either InAlAs ($k \sim 0.2$) or InP ($k \sim 0.45$) are used as the multiplier in the SACM structure. However, their high excess noise and weak temperature stability impair APD performance. This section reports the first InGaAs/$Al_{0.7}In_{0.3}As_{0.79}Sb_{0.21}$ SACM APD structure on an InP substrate [101]. Although there is a slight Al variation between $Al_{0.7}In_{0.3}As_{0.79}Sb_{0.21}$ and $Al_{0.79}In_{0.21}As_{0.74}Sb_{0.26}$, it is anticipated that their excess noise and temperature dependence of avalanche breakdown are similar, and this section use AlInAsSb to represent $Al_{0.7}In_{0.3}As_{0.79}Sb_{0.21}$.

5.1.2. Epitaxial structure design

The structure details are shown in Fig. 5.1(a). The APD consists of a 1-μm AlInAsSb multiplier (with bandgap at ~ 1.29 eV [63]) and a 1-μm InGaAs absorber. Since phase separation remains a challenge for RA AlInAsSb growth on InP [39] with a predicted miscibility gap spanning nearly all lattice matched compositions [102], AlInAsSb was grown as a digital alloy [27] with a ten monolayer period comprised of AlAs, AlSb, and InAs layers. Furthermore, several SACM APDs were grown with different charge layer parameters to optimize the electric field distribution at the absorber and multiplier. The charge layer parameters in Fig. 5.1(a) were determined to provide a high electric field at the AlInAsSb multiplier for the impact ionization process while keeping a low electric field at the InGaAs absorber to suppress the tunneling effect.

Figure 5.1(b) shows the band diagram of InGaAs/AlInAsSb APDs at zero bias. The significant conduction band offset between InGaAs and AlInAsSb makes the design of the bandgap grading scheme important. The scheme used $In_{0.53}(Al_xGa_{1-x})_{0.47}As$ and $Al_xIn_{1-x}As_ySb_{1-y}$ lattice matched to

InP. A previous report of an InGaAs/$Al_{0.85}Ga_{0.15}As_{0.56}Sb_{0.44}$ SACM APD used a single $In_{0.53}(Al_xGa_{1-x})_{0.47}As$ step bandgap grading scheme, leaving a significant conduction band offset between the grading layer and the $Al_{0.85}Ga_{0.15}As_{0.56}Sb_{0.44}$ charge layer [58]. This work used a combination of $In_{0.53}(Al_xGa_{1-x})_{0.47}As$ and $Al_xIn_{1-x}As_ySb_{1-y}$ bandgap grading layers to assist carrier injection from the absorber to the multiplier. Figure 5.1(c) shows the HR-XRD pattern of the investigated APDs with the labeled fringe peaks of the InP substrate, InGaAs absorber, and AlInAsSb multiplier/charge layer.

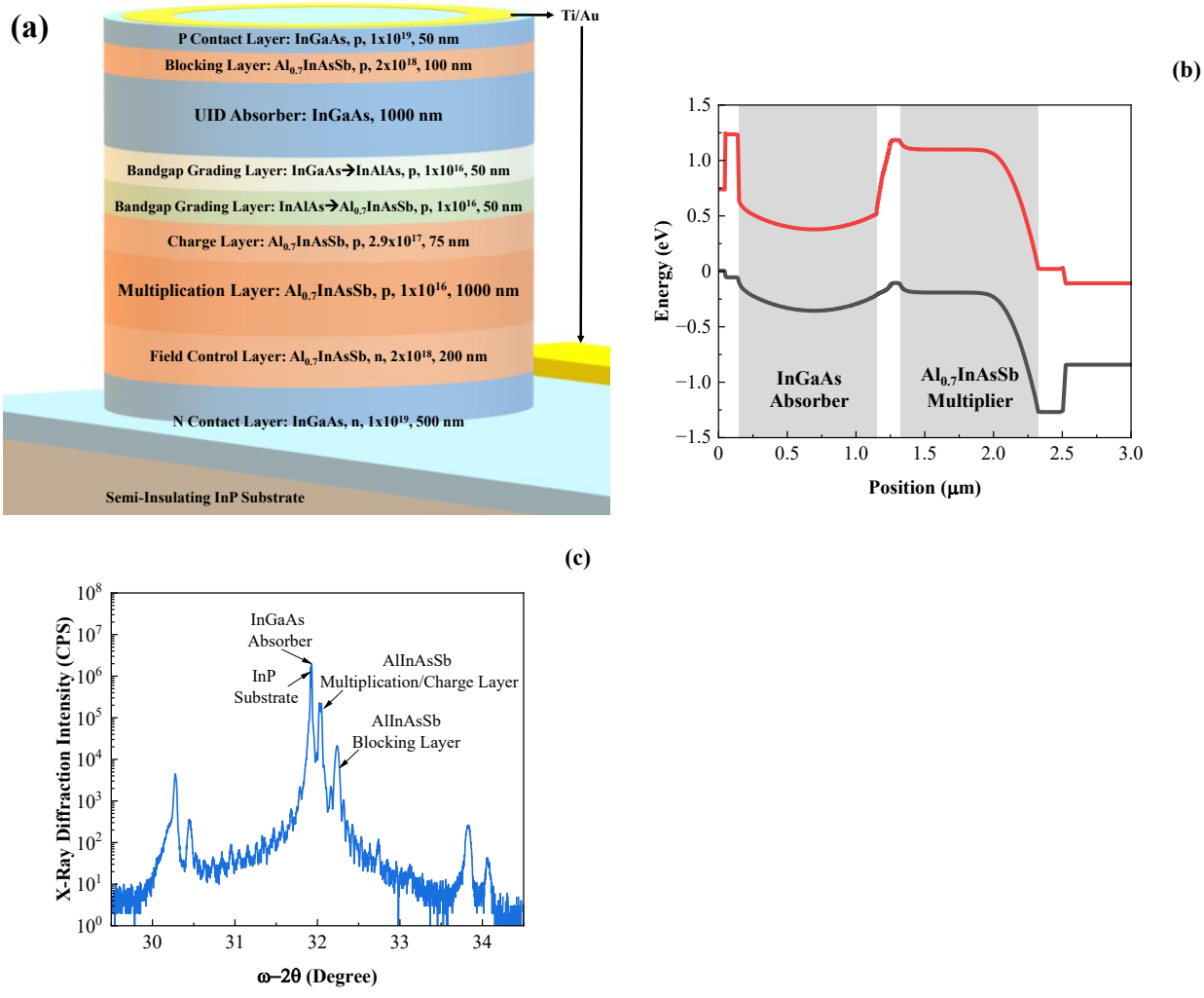

Figure 5.1. (a) Epitaxial structure of InGaAs/AlInAsSb SACM APDs. The AlInAsSb was grown as a digital alloy. (b) Band diagram at 0 V and (c) HR-XRD omega-2theta scans of InGaAs/AlInAsSb APDs.

5.1.3. Results

Figure 5.2(a) shows the current-voltage (I-V) characteristics under dark and 1550-nm illumination conditions of a 150-µm-diameter device at room temperature. The measured punch-through voltage is approximately 48 V. SACM APDs exhibit a step in the photocurrent when the depletion edge extends to the absorber. These InGaAs/AlInAsSb APDs show a second step at 55 V to 57.5 V in the photocurrent curve, which might result from the traps created during the growth of the bandgap grading layers. With increasing temperature, the second step gradually disappears. The following analysis of multiplication gain and excess noise is based on measurements above 57.5 V. The reverse bias at 57.5 V cannot be regarded as the unity gain point. Instead, the multiplication gain was determined by fitting the measured excess noise to the measured photocurrent at the reverse bias above 57.5 V [17, 22]. The maximum gain is approximately 17. Higher gain can be achieved with higher charge layer doping to suppress the onset of tunneling in the InGaAs absorber.

Figure 5.2(b) shows the excess noise characteristics under 1550-nm illumination. The dashed lines are plots using Eq. (1.2) for *k*-values ranging from 0 to 0.1. The measured *k*-value of the InGaAs/AlInAsSb APD is 0.02 to 0.04, consistent with previous excess noise measurements of $Al_{0.79}In_{0.21}As_{0.74}Sb_{0.26}$ p^+-i-n^+ APDs [40], comparable to Ge/Si SACM APDs [22, 103] and an order of magnitude lower than InGaAs/InP [43, 104] or InGaAs/InAlAs [105, 106] SACM APDs. The low excess noise in these APDs originates from the addition of the heavy Sb atom, introducing a high valence band spin-orbit splitting energy that restricts the hole impact ionization [107], similar to GaAsBi [66].

Figure 5.2(c) shows the external quantum efficiency at unity gain from 800 to 1900 nm. At 1064 nm, 1310 nm, and 1550 nm, the efficiencies are 73%, 61%, and 57%, respectively. Higher

responsivity at designated wavelengths could be realized with an anti-reflection coating or a photon-trapping structure [23].

Another important parameter of InGaAs/AlInAsSb APDs is the -3 dB bandwidth consisting of two components, the transit-time-limited and the RC-limited bandwidths. The transit-time-limited bandwidth has been calculated via the random path length (RPL) model [108], and the RC-limited bandwidth has been calculated for 40-µm-diameter devices. Figure 5.2(d) shows the simulated -3 dB bandwidth and the corresponding gain bandwidth product.

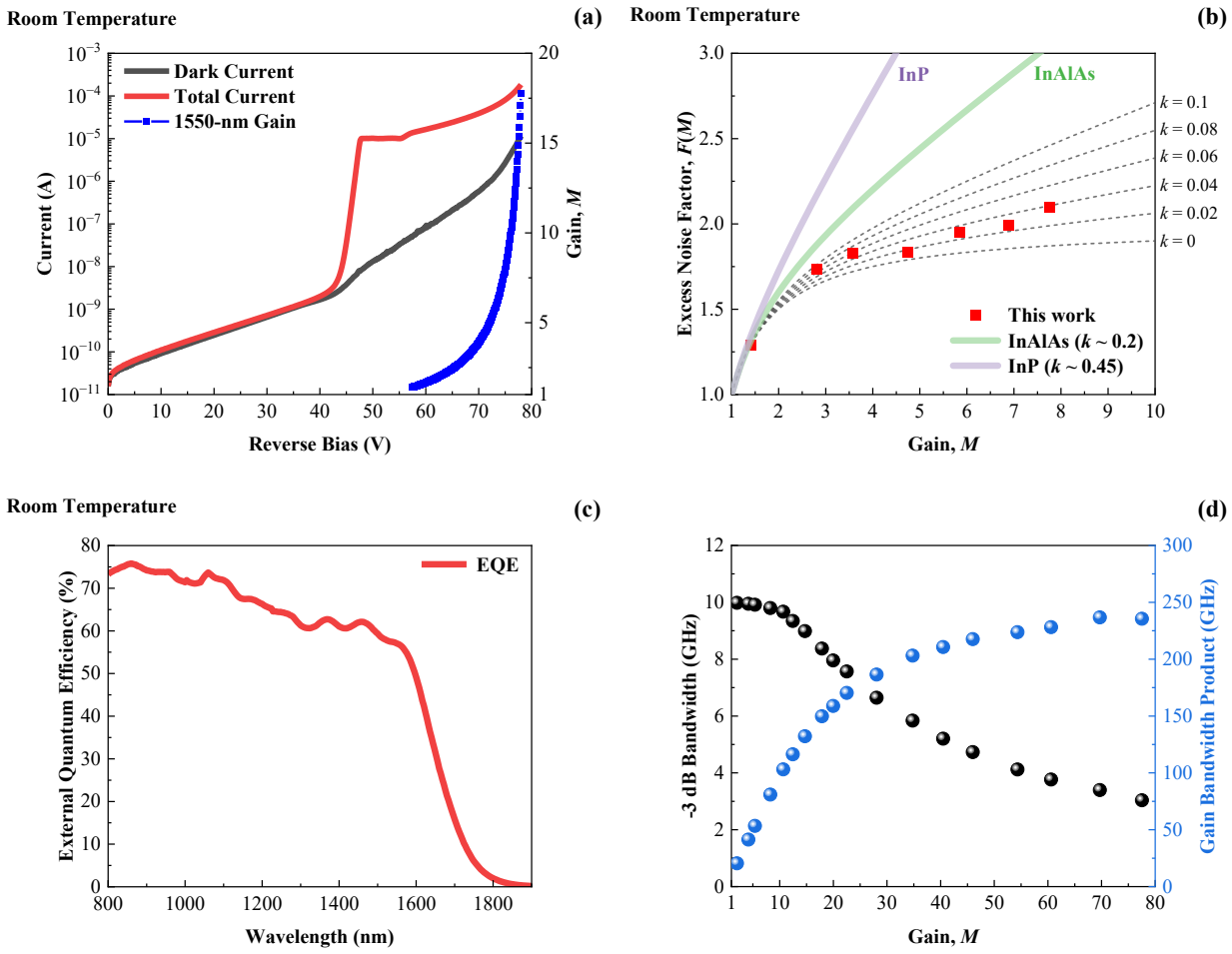

Figure 5.2. (a) Current-voltage (I-V) characteristics under dark and 1550-nm illumination conditions for 150-µm-diameter InGaAs/AlInAsSb SACM APDs at room temperature. (b) Excess noise factor versus gain. (c) External quantum efficiency versus wavelength. (d) Simulated -3 dB bandwidth and gain bandwidth product versus gain for 40-µm-diameter InGaAs/AlInAsSb SACM APDs.

The I-V characteristics of 150-µm-diameter SACM APDs were then measured from 200 to 340 K under dark and 1550-nm illumination conditions. Figure 5.3(a) shows the gain curves at various temperatures. The breakdown voltages were determined as the intercepts at $1/M = 0$, as shown in Fig. 5.3(b). The C_{bd} was determined to be (14.58 ± 0.63) mV/K via linear fitting regression. The gradient of C_{bd}, P, was used to compare the temperature sensitivity between different material-based APDs with different depletion layer thicknesses [61], and the value of P for the InGaAs/AlInAsSb SACM APD is 6.7 mV/K/µm. P values for InAlAs, InP, and Si APDs [74, 75] and AlAsSb APDs lattice matched to InP [61] are listed in Table 5.1. The temperature-dependent dark current is shown in Fig. 5.3(c). Dark current from tunneling is observed at high reverse biases, indicating that a higher gain can be obtained with a higher charge layer doping to suppress the high electric field at the InGaAs absorber.

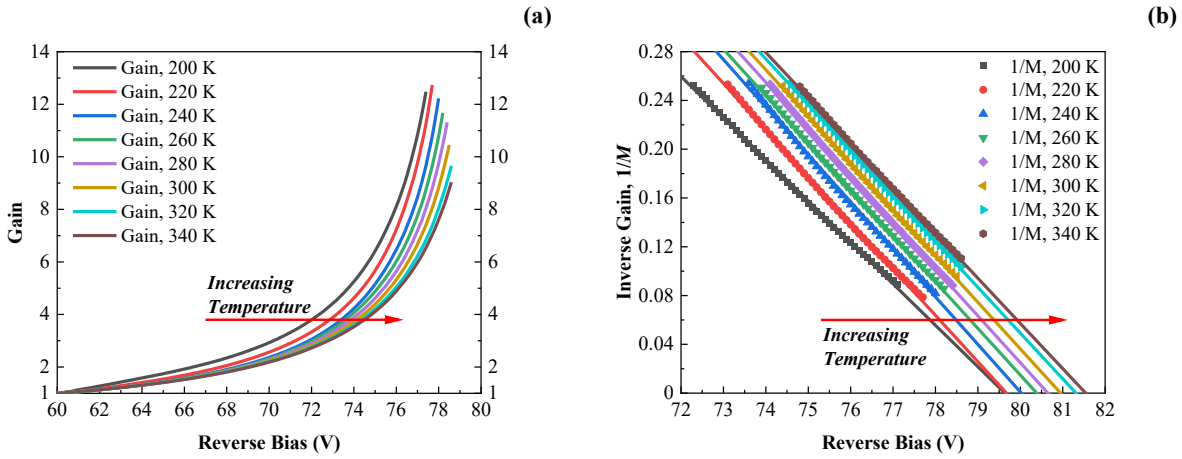

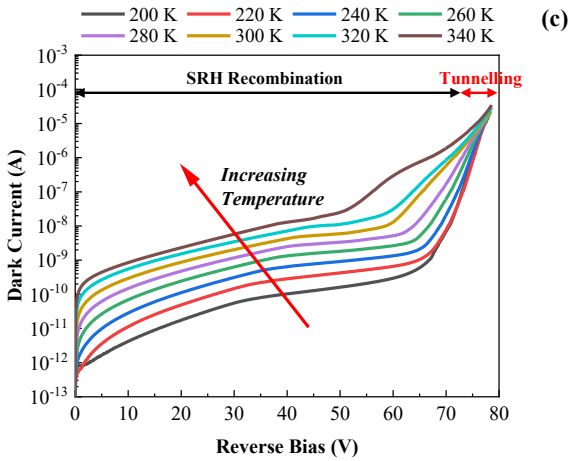

Figure 5.3. (a) Measured gain versus reverse bias, (b) inverse gain (symbols) and linear fitting (lines) under 1550-nm illumination, and (c) dark current as a function of reverse bias from 200 to 340 K with 20 K steps.

Table 5.1. Comparison of the gradient of C_{bd} between studied InGaAs/AlInAsSb APDs, AlAsSb APDs, InAlAs APDs, Si APDs, and InP APDs.

Material	Gradient of C_{bd} (mV/K/μm)
InGaAs/AlInAsSb APDs	**6.7**
AlAsSb APDs [61]	8.5
InAlAs APDs [74]	16.5
Si APDs [75]	25
InP APDs [74]	43

5.1.4. Discussion

The room-temperature and cryogenic-temperature electrical characterizations of the investigated InGaAs/AlInAsSb APD exhibit its high performance compared to commercially available APDs, making such an APD a promising candidate in SWIR applications. For example, currently available LiDAR systems in autonomous vehicles primarily utilize Si APDs operating at 905 nm. However, high-sensitivity APDs operating at longer wavelengths are preferable due to the improved detection range and resolution, and the longer operation wavelength is more eye-safe. At the same time, the strong temperature dependence of Si APDs complicates the optical

receiver design, and the increased receiver cost results in these LiDAR systems being less competitive in the market, making it necessary to employ an APD with strong temperature stability capable of operating in the changing temperatures. Furthermore, InGaAs/InP or InGaAs/InAlAs APDs are usually used for InP-substrate-based optical communications, but their noise performance is limited. A new multiplier lattice matched to InP with lower excess noise is beneficial. Therefore, the InGaAs/AlInAsSb APDs have the potential to be widely used in these applications as a promising replacement for the APDs in the current market.

5.1.5. Conclusion

We report low-noise, weak-temperature-sensitivity 1550-nm InGaAs/AlInAsSb SACM APDs on InP substrates. For APDs on InP substrates under 1550-nm illumination, the InGaAs/AlInAsSb SACM APD's excess noise is significantly lower than InAlAs- and InP-based APDs. The external quantum efficiency is 57% at 1550 nm without an anti-reflection coating. The weak temperature dependence of avalanche breakdown has been demonstrated, making these APDs promising candidates for photodetection under varying ambient conditions. Furthermore, the use of semi-insulating InP substrates is beneficial for high-speed operation.

5.2. GaAsSb/AlGaAsSb SACM APDs

5.2.1. Motivation

Both AlInAsSb and AlGaAsSb are promising InP-substrate-based multiplier materials. Section 5.1 have demonstrated RA InGaAs/AlInAsSb SACM APDs with advantageous performances. This section will investigate the AlGaAsSb-based SACM APDs. Previously, InGaAs/AlGaAsSb SACM APDs were demonstrated, where InGaAs was used for SWIR photodetection, and AlGaAsSb was used to provide low excess noise. A high gain-bandwidth product of 424 GHz was

obtained [58]. However, a significant conduction band offset exists between the InGaAs absorber and AlGaAsSb multiplier. Although the $In_{0.53}(Al_xGa_{1-x})_{0.47}As$ step bandgap grading scheme was used in Ref. [58], a relatively large conduction bandgap offset still exists between the AlGaAsSb charge layer and neighboring $In_{0.53}Al_{0.47}As$ bandgap grading layer. This may result in photo-generated carriers being trapped between these two layers.

To solve the significant conduction band offset issue, $GaAs_{0.51}Sb_{0.49}$ is employed as the absorber material in this work, and the $Al_{0\rightarrow0.85}Ga_{1\rightarrow0.15}As_{0.51}Sb_{0.49}$ bandgap grading scheme was used to realize the smooth conduction band transition from $GaAs_{0.51}Sb_{0.49}$ (GaAsSb) absorber to $Al_{0.85}Ga_{0.15}As_{0.51}Sb_{0.49}$ multiplier. Figure 5.4(a) shows the epitaxial structure of GaAsSb/AlGaAsSb SACM APDs, where a 500-nm GaAsSb absorber is used for SWIR photodetection, and a 1000-nm AlGaAsSb multiplier is used to obtain low excess noise.

The charge layer thickness and doping were optimized via iterative growth rounds to obtain proper electric field distribution in the absorber and the multiplier. Step bandgap grading scheme was employed here, comprising a 30-nm $Al_{0.25}Ga_{0.75}As_{0.51}Sb_{0.49}$ UID layer, a 30-nm $Al_{0.5}Ga_{0.5}As_{0.51}Sb_{0.49}$ UID layer, and a 30-nm $Al_{0.25}Ga_{0.75}As_{0.51}Sb_{0.49}$ UID layer), as an alternative to the linear bandgap grading scheme to simplify the growth procedure. The band diagrams were then simulated at 0 V, 42 V (around punch-through voltage), and 67 V (around breakdown voltage), as shown in Fig. 5.4(b).

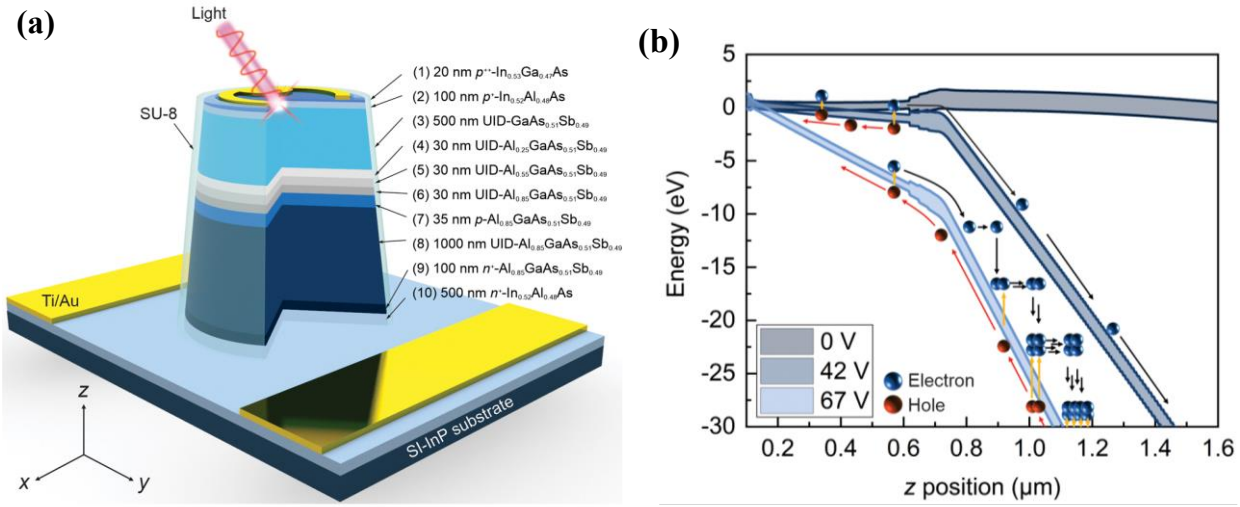

Figure 5.4. (a) Epitaxial structure of GaAsSb/AlGaAsSb SACM APDs. (b) Band diagram at 0 V, 42 V (around punch-through voltage), and 67 V (around breakdown voltage).

5.2.2. Results

5.2.2.1. Electrical characterizations

Figure 5.5(a) shows the current-voltage (I-V) characteristics under dark and 1550-nm illumination conditions of a 200-μm-diameter device at room temperature. The measured punch-through and breakdown voltages are approximately 45 V and 70 V, which vary slightly from the simulated ones due to the growth variation of charge layer parameters. It is noted that there is a second step at 53 V to 54 V in the photocurrent curve, and the trap in the bandgap grading scheme might cause this. Using a linear bandgap grading scheme is anticipated to address this trapping problem. The following analysis of multiplication gain and excess noise is based on measurements above 54 V. The reverse bias at 54 V cannot be regarded as the unity gain point, and the gain at 54 V was calculated to be 3.6 based on the simulated electric field at multiplier and impact ionization coefficients of AlGaAsSb [107]. The gain curve was then determined based on the measured photocurrent, and the maximum gain was about 278, an order of magnitude higher than the commercial 1550-nm APDs.

Figure 5.5(b) shows the excess noise characteristics under 1550-nm illumination. The dashed lines are plots using Eq. (1.2) for *k*-values ranging from 0 to 0.1. The measured *k*-value of the GaAsSb/AlGaAsSb APD is 0 to 0.02, consistent with previous excess noise measurements of AlGaAsSb p^+-i-n^+ APDs [28, 38], comparable to Ge/Si SACM APDs [22, 103], and an order of magnitude lower than InGaAs/InP [43, 104] or InGaAs/InAlAs [105, 106] SACM APDs. Figure 5.5(c) shows the external quantum efficiency at unity gain from 1000 to 1900 nm without an anti-reflection coating, and the efficiency is 21% at 1550 nm.

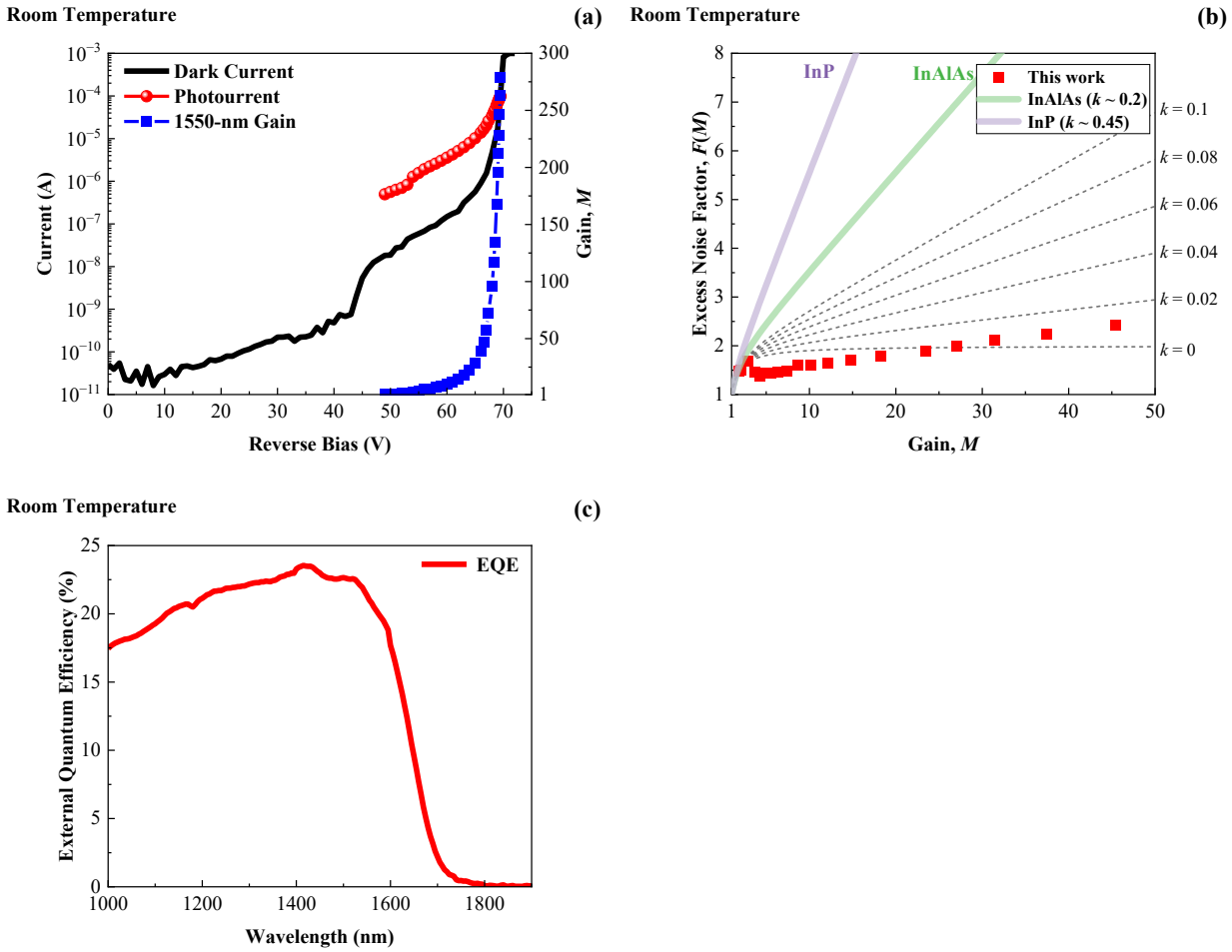

Figure 5.5. (a) Current-voltage (I-V) characteristics under dark and 1550-nm illumination conditions for 200-µm-diameter GaAsSb/AlGaAsSb SACM APDs at room temperature. (b) Excess noise factor versus gain. (c) External quantum efficiency versus wavelength.

5.2.2.2. Bandwidth characterization

The RF-frequency behavior has been characterized for 100-µm, 150-µm, and 200-µm GaAsSb/AlGaAsSb APDs. Large-diameter devices were investigated here since commercial APDs used in LiDAR systems require a large optical window to enhance the optical signal input. Figures 5.6(a) – (c) show the normalized frequency response for 100-µm, 150-µm, and 200-µm APDs under reverse bias from 60 V to 67 V in 1 V steps. The corresponding 3-dB bandwidth and gain-bandwidth product were then determined, as shown in Figs. 5.6(d) – (e). The maximum 3-dB bandwidth values were ~ 1.9 GHz, ~ 1 GHz, and ~ 0.7 GHz for 100-µm, 150-µm, and 200-µm APDs. The 3-dB bandwidth increases as the diameter decreases, indicating that the bandwidth is limited by the RC time constant instead of the carrier transit time. A higher bandwidth is anticipated for APDs with a smaller diameter. Additionally, by forward current-voltage (I-V) and capacitance-voltage (C-V) measurements, the RC-limited bandwidth is estimated to be 2.4 GHz, 1.2 GHz, and 0.85 GHz for 100-µm, 150-µm, and 200-µm APDs, indicating that the bandwidth is limited by the RC time constant. Moreover, the maximum gain-bandwidth product was determined to be ~ 100 GHz for 100-µm-diameter devices.

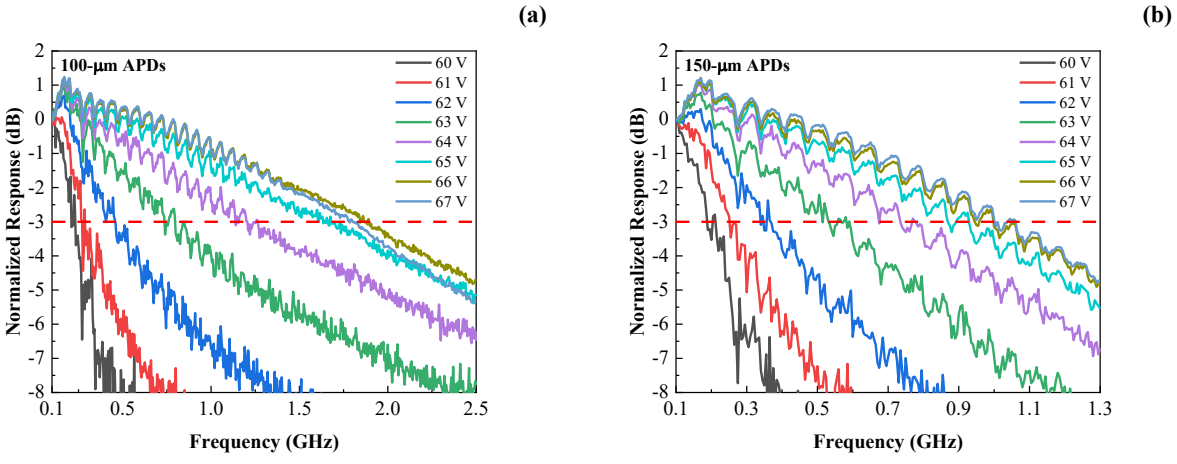

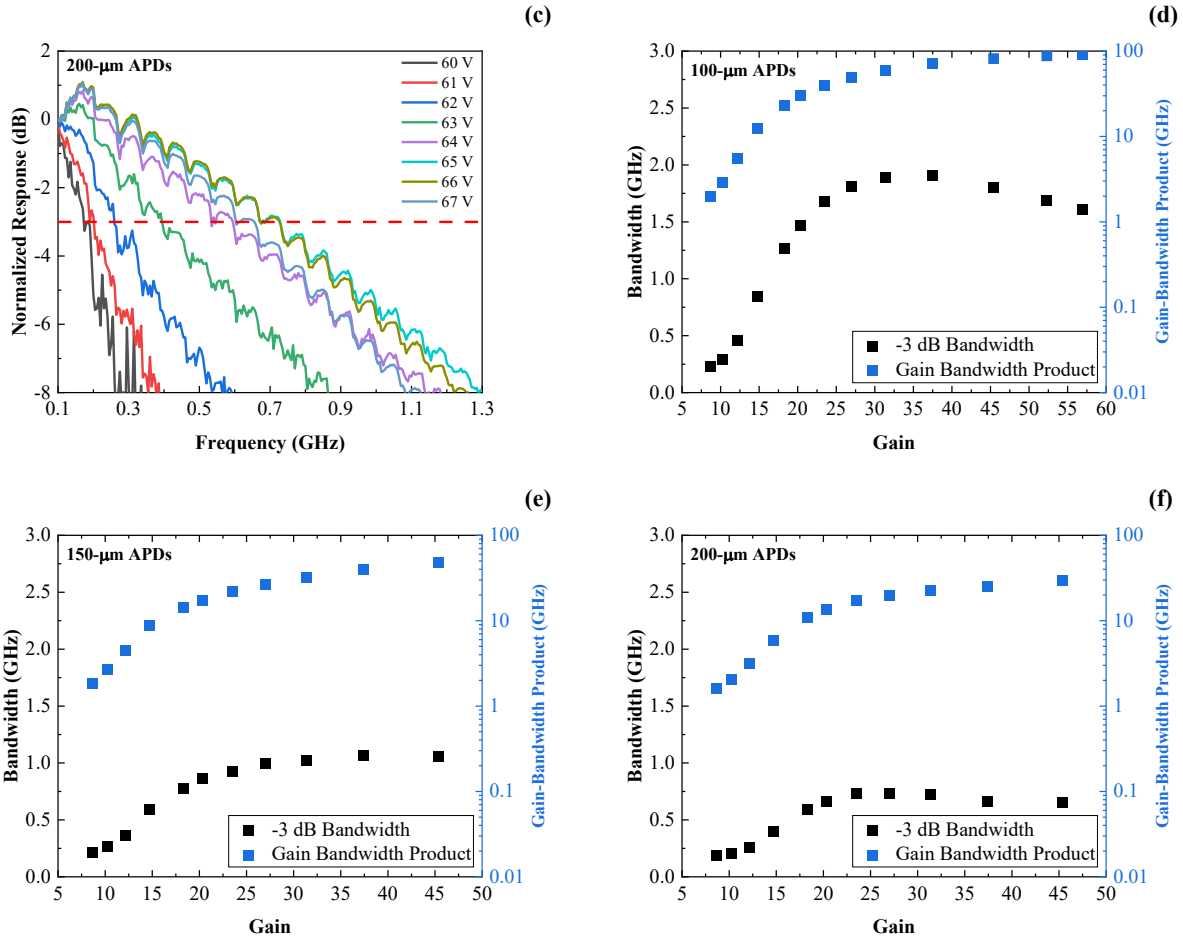

Figure 5.6. Measured normalized frequency response under different reverse biases for (a) 100-µm, (b) 150-µm, and (c) 200-µm GaAsSb/AlGaAsSb APDs. 3-dB bandwidth and gain-bandwidth product versus gain for (d) 100-µm, (e) 150-µm, and (f) 200-µm APDs.

5.2.3. Conclusion

GaAsSb/AlGaAsSb APDs have been demonstrated with high gain at 278 and extremely low excess noise ($k \sim 0 - 0.02$), indicating enhanced detection sensitivity in comparison to commercially available 1550-nm APDs including Ge/Si, InGaAs/InAlAs, and InGaAs/InP APDs. Compared to InGaAs/AlGaAsSb APDs, GaAsSb/AlGaAsSb APDs exhibit a smaller conduction band offset, beneficial for the carrier transit between the absorber and the multiplier. These APDs have the potential to be widely used in commercial and military SWIR applications where high photodetection sensitivity is required. For future investigation, the external quantum efficiency

could be further improved by adding an anti-reflection coating or a photon-trapping structure. The bandwidth could also be increased by a bandgap grading scheme to solve the carrier trap issue and fabricating smaller devices to increase the RC-limited bandwidth.

5.3. DA InGaAs/AlGaAsSb SACM APDs

5.3.1. Motivation

As discussed in Chapter 4, the digital alloy growth technique has been employed for the conventional InGaAs material system to realize bandgap engineering, and the DA InGaAs absorber could be utilized for extended SWIR applications. The bandgap of the DA InGaAs, and subsequently, the spectral response of the SACM APDs, can be tuned by changing the DA InAs/GaAs period thickness.

Similar to Sections 5.1 and 5.2, Sb-based SACM APDs were investigated with a DA AlGaAsSb multiplier and a DA InGaAs absorber to extend the absorption window. The room-temperature gain, excess noise, temperature-dependent dark current, and avalanche breakdown of the DA InGaAs/AlGaAsSb SACM APDs are presented in this section.

Figure 5.7 shows the epitaxial structure of InGaAs/AlGaAsSb SACM APDs. Two samples were grown with the same structure, but with the absorber grown as 5 ML DA InGaAs and RA InGaAs, respectively. The RA InGaAs/AlGaAsSb SACM APD sample was grown for comparison. The thicknesses of the InGaAs absorber and the AlGaAsSb multiplier are 500 nm and 200 nm, respectively.

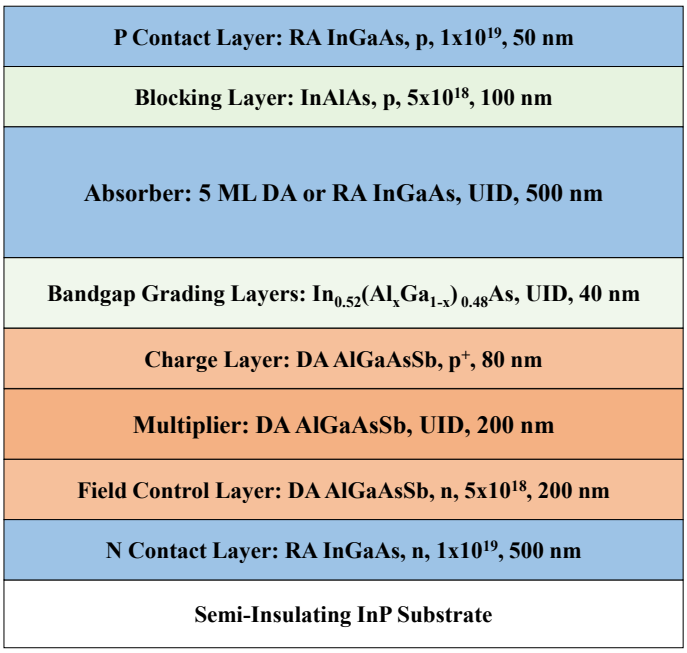

Figure 5.7. Epitaxial structure of InGaAs/AlGaAsSb SACM APDs.

5.3.2. Results

5.3.2.1. Electrical characterizations

Figure 5.8 shows the comparison of room-temperature EQE between 250-µm-diameter RA and DA InGaAs/AlGaAsSb APDs at the punch-through voltage. The cut-off wavelength of DA InGaAs/AlGaAsSb APDs was effectively extended to ~ 2 µm. To improve the EQE at the extended SWIR spectral region further, an anti-reflection coating or a photon-trapping structure [23] could be employed. The photon-trapping structure approach is discussed in Section 6.1.

Figure 5.9(a) shows the room-temperature current-voltage (I-V) characteristics under dark and 1550-nm illumination conditions for 150-µm-diameter DA InGaAs/AlGaAsSb SACM APDs. The maximum gain is determined to be above 30 [22]. Figure 5.9(b) shows the excess noise characteristics of DA InGaAs/AlGaAsSb SACM APDs, and the *k*-value is determined to be ~ 0.05, consistent with previously measured AlGaAsSb p^+-i-n^+ APDs [36] and comparable to Ge/Si SACM APDs [22, 103].

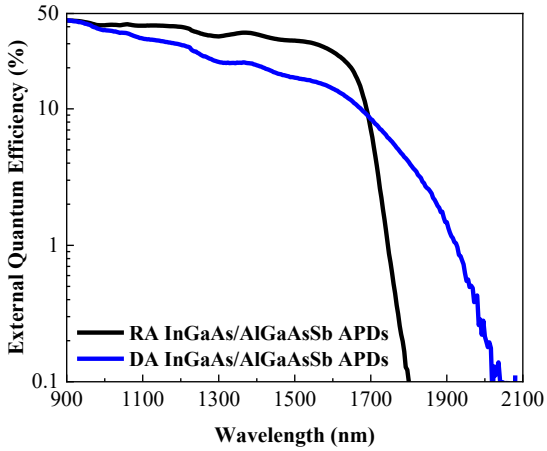

Figure 5.8. Comparison of room-temperature EQE between SACM APDs with RA and 5 ML DA InGaAs absorbers.

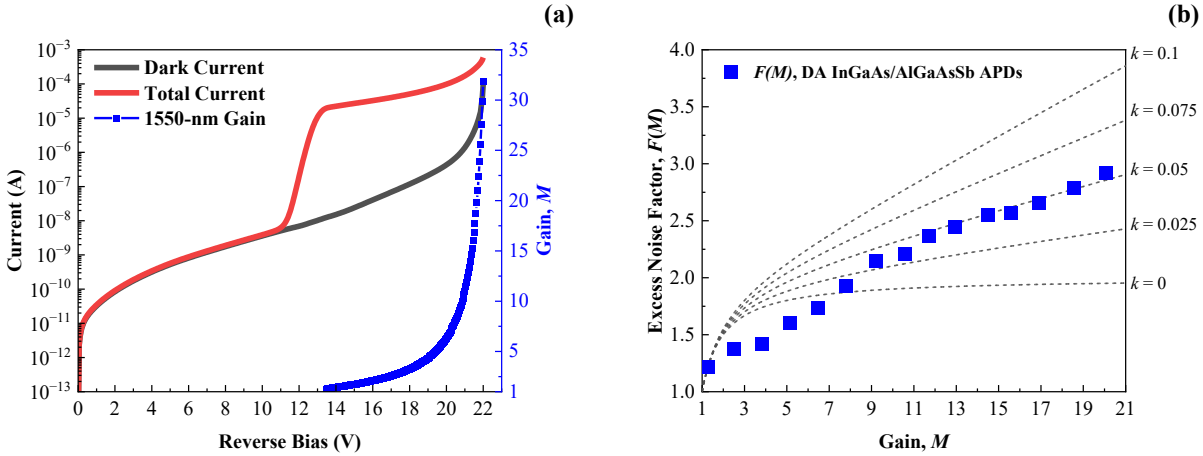

Figure 5.9. (a) Room-temperature current-voltage (I-V) characteristics under dark and 1550-nm illumination conditions and gain curves for 150-µm-diameter DA InGaAs/AlGaAsSb SACM APDs. (b) Room-temperature excess noise characteristics under 1550-nm illumination for DA InGaAs/AlGaAsSb SACM APDs.

Figure 5.10 shows the comparison of temperature-dependent dark current between RA and DA InGaAs/AlGaAsSb SACM APDs in a temperature range of 80 K to 360 K. Without considering the tunneling region originating from the lower charge layer doping for RA InGaAs/AlGaAsSb

SACM APDs, it is noted that the dark current is comparable between RA InGaAs- and DA InGaAs-based SACM APDs.

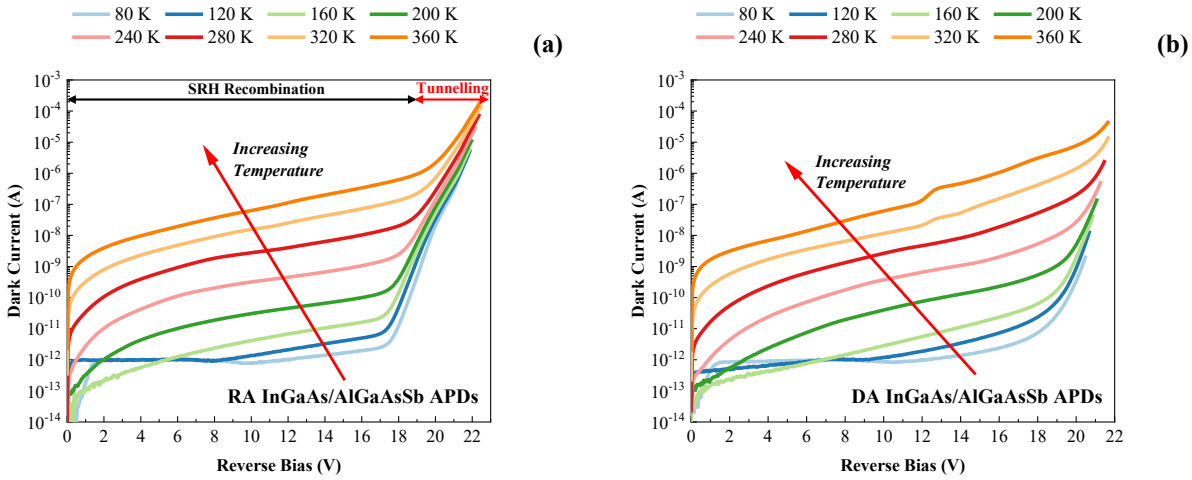

Figure 5.10. Temperature-dependent dark current characteristics of 150-µm-diameter (a) RA InGaAs/AlGaAsSb APDs and (b) DA InGaAs/AlGaAsSb APDs from 80 K to 360 K.

5.3.2.2. Temperature-dependent avalanche breakdown

To determine the temperature stability, the 1550-nm gain was measured from 80 K to 360 K for DA InGaAs/AlGaAsSb SACM APDs. Similar to investigations of the temperature-dependent avalanche breakdown for Sb-basd p^+-i-n^+ APDs, the temperature-dependent breakdown voltages were determined by the linear extrapolation of the inverse gain curves, $1/M$, to the reverse bias axis. As shown in Fig. 5.11, the C_{bd} value was determined to be (4.14 ± 0.16) mV/K for DA InGaAs/AlGaAsSb SACM APDs, and the gradient of C_{bd}, P, was calculated to be 5.0 mV/K/µm, indicating the weak temperature sensitivity of studied DA InGaAs/AlGaAsSb SACM APDs.

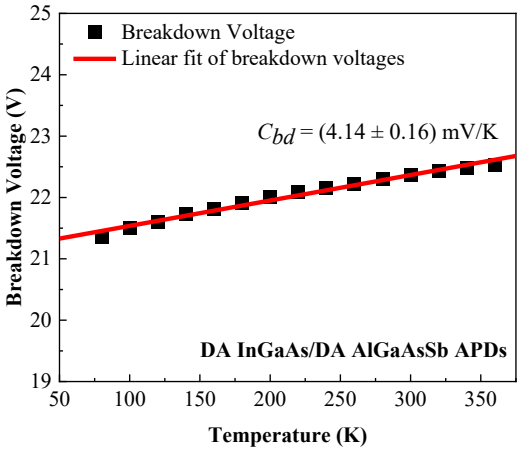

Figure 5.11. Temperature dependence of avalanche breakdown for DA InGaAs/AlGaAsSb SACM APDs from 80 K to 360 K. Symbols are measured breakdown voltages, and the solid line is the linear fitting curve.

5.3.3. Conclusion

InGaAs/AlGaAsSb SACM APDs with 5 ML DA InGaAs absorber and DA AlGaAsSb multiplier on semi-insulating InP substrates have been demonstrated. The absorption window was effectively extended to 2 μm due to the employment of DA InGaAs material system. The excess noise characteristics are comparable to Ge/Si SACM APDs with a k-value of ~ 0.05. The C_{bd} value was determined to be 4.14 mV/K for DA InGaAs/AlGaAsSb SACM APDs, significantly lower than that of InAlAs-, InP-, and Si-based APDs. Furthermore, the dark current levels are comparable between RA and DA InGaAs-based SACM APDs, meaning that the employment of DA InGaAs absorber does not increase the dark current level significantly. Therefore, DA InGaAs/AlGaAsSb APDs have the potential to be widely used for extended SWIR photodetection in conditions where temperatures can change rapidly.

6. Future Work

6.1. External quantum efficiency enhancement of DA InGaAs/AlGaAsSb APDs

As described in Chapter 4 and Section 5.3, Si and RA InGaAs photodetectors cannot satisfy the requirements of extended SWIR applications [17, 19, 20], and the digital alloy growth technique can be used for the InGaAs material system to realize the bandgap engineering [109]. The cut-off wavelength of DA InGaAs can be effectively extended compared to conventional RA InGaAs. However, the absorption coefficient of DA InGaAs is strongly limited at the extended SWIR spectral region due to the low material quality, making the EQE low. The absorption coefficients of 6 ML, 8 ML, and 10 ML DA InGaAs at 2 μm are only 398 cm^{-1}, 831 cm^{-1}, and 1230 cm^{-1}, respectively.

To solve the limited photoresponse issue of the DA InGaAs photodetectors, we could either investigate approaches to improve the material quality to obtain a higher absorption coefficient or employ a photon-trapping structure for photodetectors. Although the investigation of improvement of the DA InGaAs material quality is more straightforward, it is more complicated and costly since the digital alloy growth requires precise atomic-level control in the MBE system. Typically, numerous iterative growth rounds are needed to obtain better lattice matching. Therefore, the photon-trapping structure approach offers a more promising way to improve photodetection efficiency.

A series of optical and electrical simulations will be carried out using Lumerical software to design the photon trapping structures. In this work, one could investigate the DA InGaAs/AlGaAsSb SACM APD sample described in Section 5.3. To enhance the EQE of the DA InGaAs APDs, a photon-trapping structure based on a photonic crystal approach will be used. Figure 6.1(a) shows a triangular photonic crystal with air holes etched into the InGaAs absorber.

Photonic crystal parameters can be optimized to maximize the EQE, including spacing *a*, diameter *d*, and etching depth *h*. Two effects can explain the EQE enhancement via a photonic crystal structure. First, the photonic crystal diffracts the normal incident light and couples it into the photonic-crystal-slab mode, laterally propagating in the InGaAs absorber. This increases the effective optical absorption length. Second, in the vertical direction, the photonic-crystal-slab mode is confined by total internal reflection, leading to a standing wave in the absorber [45]. Figure 6.1(b) shows a scanning electron microscopy image of a fabricated photonic crystal array, demonstrating the fabrication feasibility. After the EQE enhancement demonstration via Lumerical simulation, the DA InGaAs/AlGaAsSb APDs will be fabricated with the photon-trapping structure to demonstrate enhanced EQE at the extended SWIR spectral region in the experiment.

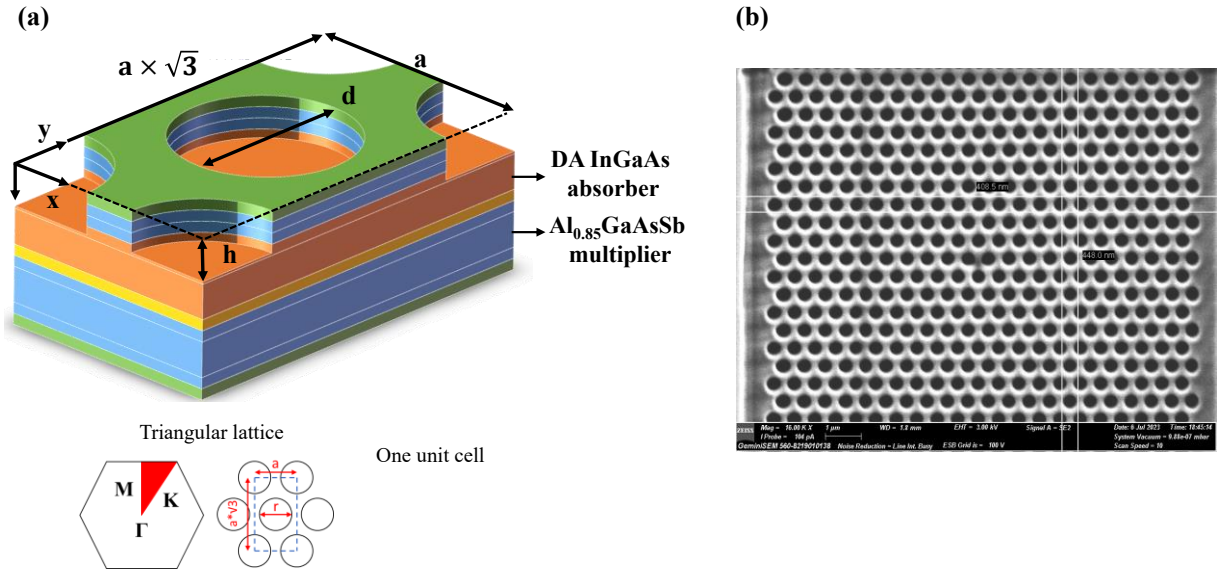

Figure 6.1. (a) A unit cell of the triangular photonic crystal used for EQE enhancement in DA InGaAs/AlGaAsSb APDs. (b) Scanning electron microscopy image of a fabricated photonic crystal array.

Compared to APDs with conventional InGaAs absorbers, DA InGaAs/AlGaAsSb SACM APDs with enhanced EQE are advantageous for various interdisciplinary applications. For example, the current non-invasive mammal imaging in the second near-infrared window is limited

by the absorption window of the commercial InGaAs photodetectors, and a photodetector operating at the extended SWIR spectral region is desired to push forward the imaging window for better imaging quality [19]. Therefore, photodetectors equipped with DA InGaAs absorbers hold significant potential for widespread applications, positioning them as strong contenders against traditional InGaAs photodetectors.

In summary, we aim to explore DA InGaAs/AlGaAsSb APDs incorporating a photon trapping structure to achieve low excess noise, strong temperature stability, and an extended absorption window with enhanced EQE, beneficial for weak optical signal detection under varying ambient conditions. Such APDs show great potential for being widely used in SWIR research and commercial applications, and the proposed photon trapping structure offers potential for adaptation to photodetectors across various spectral regions.

6.2. InGaAs/AlGaAsSb APDs on Si by heteroepitaxy

Heterogeneous silicon photonics is increasingly attracting research and commercial attention in applications such as telecommunication, data center, and sensing [110]. The active and passive components of heterogeneous silicon photonics have been widely reported, such as lasers [111, 112], modulators [113, 114], photodiodes [106, 115], waveguides [116, 117], couplers, multiplexers, and splitters [118]. As for the silicon photonics-compatible III-V photodetectors, APDs are advantageous owing to the capability of weak optical signal detection compared to conventional photodiodes, yet the research of APDs on Si has been limited. The integration of III-V APDs on Si can be accomplished by wafer bonding, micro-transfer-printing, or heteroepitaxial growth. We will choose the heteroepitaxial growth approach in the future work, since this is the only wafer-level solution, and the fabrication process is simpler.

The InGaAs/InP and InGaAs/InAlAs SACM APDs have been extensively developed on InP substrates, with their structural designs reaching a level of commercial maturity. Consequently, the initial APDs grown on Si through heteroepitaxy adopted an InGaAs/InAlAs SACM structure [106], where the InGaAs absorber is used to realize the 1550-nm absorption, and the InAlAs multiplier is used to provide multiplication gain. For InGaAs/InAlAs SACM APDs on Si, the *k*-value was determined to be ~ 0.2 (up to gain ~ 5), and the dark current was one order of magnitude higher than the InGaAs/InAlAs SACM APDs on InP due to the increased material defects. Additionally, due to a mistake in the growth of the bandgap grading layers, the photo-generated carriers were injected from the InGaAs absorber to the InAlAs multiplier before the punch-through voltage, and future design or growth optimization is required. With the foundational work on SACM APDs on Si using traditional materials, the exploration of AlGaAsSb as a multiplication material has the potential to reduce the excess noise and enhance temperature stability.

As shown in Fig. 6.2(a), a proposed design for the epitaxial structure is similar to the one discussed in Section 5.3. One InGaAs/AlGaAsSb SACM APD sample will be grown on a Si substrate, and another will be grown on an InP substrate as a control sample. As shown in Fig. 6.2(b), the InP/Si template consists of a Ge layer, a GaAs layer, a linearly graded metamorphic InAlAs buffer layer, and an InP layer. This approach has the advantage of growth on a full Si wafer. After the growth and the fabrication of InGaAs/AlGaAsSb SACM APDs on Si and InP substrates, characteristics of dark current, gain, excess noise, and temperature-dependence of avalanche breakdown will be studied. The gain, excess noise, and temperature stability of APDs on Si and InP substrates are anticipated to be similar. Additionally, the variation in dark current between APDs on Si and InP substrates is determined by specific growth conditions, such as the density of defects.

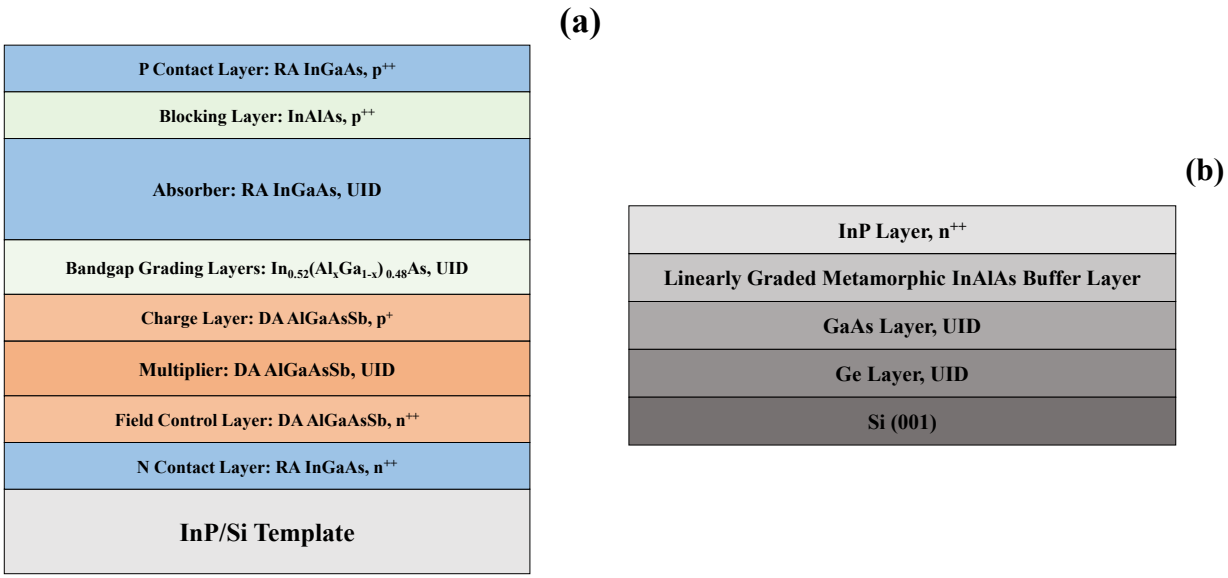

Figure 6.2. (a) Structure of InGaAs/AlGaAsSb SACM APDs on Si substrates. (b) Structure of the InP/Si template.

References

[1] J. C. Campbell, "Recent advances in avalanche photodiodes," *Journal of Lightwave Technology,* vol. 34, no. 2, pp. 278-285, 2016.

[2] J. C. Campbell, "Evolution of low-noise avalanche photodetectors," *IEEE Journal of Selected Topics in Quantum Electronics,* vol. 28, p. 3800911, 2021.

[3] B. Wang and J. Mu, "High-speed Si-Ge avalanche photodiodes," *PhotoniX,* vol. 3, no. 1, pp. 1-22, 2022.

[4] S. Krishna *et al.*, "Linear mode avalanche photodiodes with antimonide multipliers on InP substrates," *IEEE Journal of Quantum Electronics,* vol. 58, no. 4, p. 4500207, 2022.

[5] R. J. McIntyre, "Multiplication noise in uniform avalanche diodes," *IEEE Transactions on Electron Devices,* vol. ED-13, no. 1, pp. 164-168, 1966.

[6] J. C. Campbell, "Advances in photodetectors," in *Optical fiber telecommunications*: Academic Press, 2008, pp. 221-268.

[7] B. E. A. Saleh and M. C. Teich, *Fundamentals of photonics*. John Wiley & Sons, 2019.

[8] R. B. Emmons, "Avalanche-photodiode frequency response," *Journal of Applied Physics,* vol. 38, no. 9, pp. 3705-3714, 1967.

[9] S. A. Plimmer, J. P. R. David, and D. S. Ong, "The merits and limitations of local impact ionization theory," *IEEE Transactions on Electron Devices,* vol. 47, no. 5, pp. 1080-1088, 2000.

[10] S. D. March, A. H. Jones, J. C. Campbell, and S. R. Bank, "Multistep staircase avalanche photodiodes with extremely low noise and deterministic amplification," *Nature Photonics,* vol. 15, no. 6, pp. 468-474, 2021.

[11] X. Yi *et al.*, "Demonstration of large ionization coefficient ratio in AlAs $_{0.56}$Sb$_{0.44}$ lattice matched to InP," *Scientific Reports,* vol. 8, no. 1, pp. 1-6, 2018.

[12] C. A. Lee, R. A. Logan, R. L. Batdorf, J. J. Kleimack, and W. Wiegmann, "Ionization rates of holes and electrons in silicon," *Physical Review,* vol. 134, no. 3A, p. A761, 1964.

[13] V. M. Robbins, T. Wang, K. F. Brennan, K. Hess, and G. E. Stillman, "Electron and hole impact ionization coefficients in (100) and in (111) Si," *Journal of Applied Physics,* vol. 58, no. 12, pp. 4614-4617, 1985.

[14] X. Sun, J. B. Abshire, J. D. Beck, P. Mitra, K. Reiff, and G. Yang, "HgCdTe avalanche photodiode detectors for airborne and spaceborne lidar at infrared wavelengths," *Optics Express,* vol. 25, no. 14, pp. 16589-16602, 2017.

[15] P. J. Ker, J. P. R. David, and C. H. Tan, "Temperature dependence of gain and excess noise in InAs electron avalanche photodiodes," *Optics Express,* vol. 20, no. 28, pp. 29568-29576, 2012.

[16] M. Ren, S. J. Maddox, M. E. Woodson, Y. Chen, S. R. Bank, and J. C. Campbell, "Characteristics of $Al_xIn_{1-x}As_ySb_{1-y}$ (x: 0.3−0.7) avalanche photodiodes," *Journal of Lightwave Technology,* vol. 35, no. 12, pp. 2380-2384, 2017.

[17] A. H. Jones, S. D. March, S. R. Bank, and J. C. Campbell, "Low-noise high-temperature AlInAsSb/GaSb avalanche photodiodes for 2-μm applications," *Nature Photonics,* vol. 14, no. 9, pp. 559-563, 2020.

[18] A. H. Jones *et al.*, "Room-temperature bandwidth of 2-μm AlInAsSb avalanche photodiodes," *Optics Express,* vol. 29, no. 23, pp. 38939-38945, 2021.

[19] Z. Feng *et al.*, "Perfecting and extending the near-infrared imaging window," *Light: Science & Applications,* vol. 10, no. 1, p. 197, 2021.

[20] Y. Zou, S. Chakravarty, C.-J. Chung, X. Xu, and R. T. Chen, "Mid-infrared silicon photonic waveguides and devices," *Photonics Research,* vol. 6, no. 4, pp. 254-276, 2018.
[21] G. E. Stillman and C. M. Wolfe, "Avalanche photodiodes," in *Semiconductors and semimetals*, vol. 12: Elsevier, 1977, pp. 330-337.
[22] H.-D. Liu *et al.*, "Avalanche photodiode punch-through gain determination through excess noise analysis," *Journal of Applied Physics,* vol. 106, no. 6, p. 064507, 2009.
[23] D. Chen *et al.*, "Photon-trapping-enhanced avalanche photodiodes for mid-infrared applications," *Nature Photonics,* vol. 17, pp. 594-600, 2023.
[24] Y. Gao *et al.*, "Photon-trapping microstructures enable high-speed high-efficiency silicon photodiodes," *Nature Photonics,* vol. 11, no. 5, pp. 301-308, 2017/05/01 2017.
[25] K. Kato, S. Hata, K. Kawano, and A. Kozen, "Design of ultrawide-band, high-sensitivity pin protodetectors," *IEICE transactions on electronics,* vol. 76, no. 2, pp. 214-221, 1993.
[26] Y. Peng, K. Sun, Y. Shen, B. Guo, A. Beling, and J. C. Campbell, "High-Gain Ka-Band Analog Photonic Link Using High-Power Photodiode at 1064 nm," *Journal of Lightwave Technology,* vol. 39, no. 6, pp. 1724-1732, 2021.
[27] S. J. Maddox, S. D. March, and S. R. Bank, "Broadly tunable AlInAsSb digital alloys grown on GaSb," *Crystal Growth & Design,* vol. 16, no. 7, pp. 3582-3586, 2016.
[28] S. Lee *et al.*, "Low noise $Al_{0.85}Ga_{0.15}As_{0.56}Sb_{0.44}$ avalanche photodiodes on InP substrates," *Applied Physics Letters,* vol. 118, no. 8, p. 081106, 2021.
[29] J. Zheng *et al.*, "Digital alloy InAlAs avalanche photodiodes," *Journal of Lightwave Technology,* vol. 36, no. 17, pp. 3580-3585, 2018.
[30] S. Z. Ahmed, Y. Tan, J. Zheng, J. C. Campbell, and A. W. Ghosh, "Atomistic Transport Modeling, Design Principles, and Empirical Rules for Low-Noise III-V Digital-Alloy Avalanche Photodiodes," *Physical Review Applied,* vol. 17, no. 3, p. 034044, 2022.
[31] J. Zheng, Y. Tan, Y. Yuan, A. W. Ghosh, and J. C. Campbell, "Strain effect on band structure of InAlAs digital alloy," *Journal of Applied Physics,* vol. 125, no. 8, p. 082514, 2019.
[32] J. Yao *et al.*, "Large tunable bandgaps in the InAs/AlAs strain-compensated short-period superlattices grown by molecular beam epitaxy," *Applied Physics Letters,* vol. 118, no. 25, p. 252103, 2021.
[33] X. Yi *et al.*, "Extremely low excess noise and high sensitivity $AlAs_{0.56}Sb_{0.44}$ avalanche photodiodes," *Nature Photonics,* vol. 13, no. 10, pp. 683-686, 2019.
[34] X. Zhou, S. Zhang, J. P. R. David, J. S. Ng, and C. H. Tan, "Avalanche breakdown characteristics of $Al_{1-x}Ga_xAs_{0.56}Sb_{0.44}$ quaternary alloys," *IEEE Photonics Technology Letters,* vol. 28, no. 22, pp. 2495-2498, 2016.
[35] X. Zhou, L. L. G. Pinel, S. J. Dimler, S. Zhang, J. S. Ng, and C. H. Tan, "Thin $Al_{1-x}Ga_xAs_{0.56}Sb_{0.44}$ diodes with low excess noise," *IEEE Journal of Selected Topics in Quantum Electronics,* vol. 24, no. 2, pp. 1-5, 2018.
[36] L. L. G. Pinel *et al.*, "Effects of carrier injection profile on low noise thin $Al_{0.85}Ga_{0.15}As_{0.56}Sb_{0.44}$ avalanche photodiodes," *Optics Express,* vol. 26, no. 3, pp. 3568-3576, 2018.
[37] J. Taylor-Mew, V. Shulyak, B. White, C. H. Tan, and J. S. Ng, "Low excess noise of $Al_{0.85}Ga_{0.15}As_{0.56}Sb_{0.44}$ avalanche photodiode from pure electron injection," *IEEE Photonics Technology Letters,* vol. 33, no. 20, pp. 1155-1158, 2021.
[38] S. Lee *et al.*, "Random alloy thick AlGaAsSb avalanche photodiodes on InP substrates," *Applied Physics Letters,* vol. 120, no. 7, p. 071101, 2022.

[39] S. Tomasulo *et al.*, "Effect of molecular beam epitaxy growth conditions on phase separation in wide-bandgap InAlAsSb lattice-matched to InP," *Journal of Crystal Growth,* vol. 548, p. 125826, 2020.
[40] S. H. Kodati *et al.*, "AlInAsSb avalanche photodiodes on InP substrates," *Applied Physics Letters,* vol. 118, no. 9, p. 091101, 2021.
[41] C. Lenox *et al.*, "Thin multiplication region InAlAs homojunction avalanche photodiodes," *Applied Physics Letters,* vol. 73, no. 6, pp. 783-784, 1998.
[42] Y. L. Goh *et al.*, "Excess avalanche noise in $In_{0.52}Al_{0.48}As$," *IEEE Journal of Quantum Electronics,* vol. 43, no. 5-6, pp. 503-507, 2007.
[43] L. J. J. Tan, J. S. Ng, C. H. Tan, and J. P. R. David, "Avalanche noise characteristics in submicron InP diodes," *IEEE Journal of Quantum Electronics,* vol. 44, no. 4, pp. 378-382, 2008.
[44] M. E. Woodson, M. Ren, S. J. Maddox, Y. Chen, S. R. Bank, and J. C. Campbell, "Low-noise AlInAsSb avalanche photodiode," *Applied Physics Letters,* vol. 108, no. 8, p. 081102, 2016.
[45] D. Chen, K. Sun, A. H. Jones, and J. C. Campbell, "Efficient absorption enhancement approaches for AlInAsSb avalanche photodiodes for 2-μm applications," *Optics Express,* vol. 28, no. 17, pp. 24379-24388, 2020.
[46] Y. Yuan, J. Zheng, A. K. Rockwell, S. D. March, S. R. Bank, and J. C. Campbell, "AlInAsSb impact ionization coefficients," *IEEE Photonics Technology Letters,* vol. 31, no. 4, pp. 315-318, 2019.
[47] A. H. Jones, A. K. Rockwell, S. D. March, Y. Yuan, S. R. Bank, and J. C. Campbell, "High gain, low dark current $Al_{0.8}In_{0.2}As_{0.23}Sb_{0.77}$ avalanche photodiodes," *IEEE Photonics Technology Letters,* vol. 31, no. 24, pp. 1948-1951, 2019.
[48] J. S. Ng, C. H. Tan, J. P. R. David, G. Hill, and G. J. Rees, "Field dependence of impact ionization coefficients in $In_{0.53}Ga_{0.47}As$," *IEEE Transactions on Electron Devices,* vol. 50, no. 4, pp. 901-905, 2003.
[49] I. P. Herman, *Optical diagnostics for thin film processing*. Elsevier, 1996.
[50] H. Fujiwara, *Spectroscopic ellipsometry: principles and applications*. John Wiley & Sons, 2007.
[51] W. H. Press, H. William, S. A. Teukolsky, W. T. Vetterling, A. Saul, and B. P. Flannery, *Numerical recipes 3rd edition: The art of scientific computing*. Cambridge University Press, 2007.
[52] W. S. Weiglhofer, A. Lakhtakia, and B. Michel, "Maxwell Garnett and Bruggeman formalisms for a particulate composite with bianisotropic host medium," *Microwave and Optical Technology Letters,* vol. 15, no. 4, pp. 263-266, 1997.
[53] J. Mohrmann, T. E. Tiwald, J. S. Hale, J. N. Hilfiker, and A. C. Martin, "Application of a B-spline model dielectric function to infrared spectroscopic ellipsometry data analysis," *Journal of Vacuum Science & Technology B,* vol. 38, no. 1, p. 014001, 2020.
[54] B. Johs and J. S. Hale, "Dielectric function representation by B-splines," *physica status solidi (a),* vol. 205, no. 4, pp. 715-719, 2008.
[55] V. Lucarini, J. J. Saarinen, K.-E. Peiponen, and E. M. Vartiainen, *Kramers-Kronig relations in optical materials research*. Springer Science & Business Media, 2005.
[56] Y. L. Goh *et al.*, "Avalanche multiplication in InAlAs," *IEEE Transactions on Electron Devices,* vol. 54, no. 1, pp. 11-16, 2007.

[57] R. Van Overstraeten and H. De Man, "Measurement of the ionization rates in diffused silicon *p-n* junctions," *Solid-State Electronics,* vol. 13, no. 5, pp. 583-608, 1970.
[58] S. Xie *et al.*, "InGaAs/AlGaAsSb avalanche photodiode with high gain-bandwidth product," *Optics Express,* vol. 24, no. 21, pp. 24242-24247, 2016.
[59] D. S. Ong, K. F. Li, G. J. Rees, J. P. R. David, and P. N. Robson, "A simple model to determine multiplication and noise in avalanche photodiodes," *Journal of Applied Physics,* vol. 83, no. 6, pp. 3426-3428, 1998.
[60] H. I. J. Lewis *et al.*, "Impact ionization coefficients in $(Al_xGa_{1-x})_{0.52}In_{0.48}P$ and $Al_xGa_{1-x}As$ lattice-matched to GaAs," *IEEE Transactions on Electron Devices,* vol. 68, no. 8, pp. 4045-4050, 2021.
[61] X. Jin *et al.*, "Temperature dependence of the impact ionization coefficients in AlAsSb lattice matched to InP," *IEEE Journal of Selected Topics in Quantum Electronics,* vol. 28, no. 2, pp. 1-8, 2021.
[62] M. M. Hayat, B. E. A. Saleh, and M. C. Teich, "Effect of dead space on gain and noise of double-carrier-multiplication avalanche photodiodes," *IEEE Transactions on Electron Devices,* vol. 39, no. 3, pp. 546-552, 1992.
[63] B. Guo *et al.*, "Optical constants of $Al_{0.85}Ga_{0.15}As_{0.56}Sb_{0.44}$ and $Al_{0.79}In_{0.21}As_{0.74}Sb_{0.26}$," *Applied Physics Letters,* vol. 119, no. 17, p. 171109, 2021.
[64] M. H. Woods, W. C. Johnson, and M. A. Lampert, "Use of a Schottky barrier to measure impact ionization coefficients in semiconductors," *Solid-State Electronics,* vol. 16, no. 3, pp. 381-394, 1973.
[65] S. Z. Ahmed, "A multiscale study of P-I-N devices for computing and sensing applications," Ph.D. dissertation, School of Engineering and Applied Science, University of Virginia, 2021.
[66] Y. Liu *et al.*, "Valence band engineering of GaAsBi for low noise avalanche photodiodes," *Nature Communications,* vol. 12, no. 1, pp. 1-8, 2021.
[67] Y. Yuan *et al.*, "Temperature dependence of the ionization coefficients of InAlAs and AlGaAs digital alloys," *Photonics Research,* vol. 6, no. 8, pp. 794-799, 2018.
[68] B. K. Ng *et al.*, "Avalanche multiplication characteristics of $Al_{0.8}Ga_{0.2}As$ diodes," *IEEE Transactions on Electron Devices,* vol. 48, no. 10, pp. 2198-2204, 2001.
[69] K. Yeom, J. M. Hinckley, and J. Singh, "Theoretical study on threshold energy and impact ionization coefficient for electrons in $Si_{1-x}Ge_x$," *Applied Physics Letters,* vol. 64, no. 22, pp. 2985-2987, 1994.
[70] A. H. Jones, Y. Yuan, M. Ren, S. J. Maddox, S. R. Bank, and J. C. Campbell, "$Al_xIn_{1-x}As_ySb_{1-y}$ photodiodes with low avalanche breakdown temperature dependence," *Optics Express,* vol. 25, no. 20, pp. 24340-24345, 2017.
[71] Y. Yuan *et al.*, "Comparison of different period digital alloy $Al_{0.7}InAsSb$ avalanche photodiodes," *Journal of Lightwave Technology,* vol. 37, no. 14, pp. 3647-3654, 2019.
[72] S. Abdullah, C. H. Tan, X. Zhou, S. Zhang, L. Pinel, and J. S. Ng, "Investigation of temperature and temporal stability of AlGaAsSb avalanche photodiodes," *Optics Express,* vol. 25, no. 26, pp. 33610-33616, 2017.
[73] X. Zhou *et al.*, "Thin $Al_{1-x}Ga_xAs_{0.56}Sb_{0.44}$ diodes with extremely weak temperature dependence of avalanche breakdown," *Royal Society Open Science,* vol. 4, no. 5, p. 170071, 2017.
[74] L. J. J. Tan *et al.*, "Temperature dependence of avalanche breakdown in InP and InAlAs," *IEEE Journal of Quantum Electronics,* vol. 46, no. 8, pp. 1153-1157, 2010.

[75] D. J. Massey, J. P. R. David, and G. J. Rees, "Temperature dependence of impact ionization in submicrometer silicon devices," *IEEE Transactions on Electron Devices,* vol. 53, no. 9, pp. 2328-2334, 2006.
[76] J. S. L. Ong, J. S. Ng, A. B. Krysa, and J. P. R. David, "Temperature dependence of avalanche multiplication and breakdown voltage in $Al_{0.52}In_{0.48}P$," (in English), *Journal of Applied Physics,* vol. 115, no. 6, p. 064507, Feb 14 2014.
[77] J. W. Harrison and J. R. Hauser, "Alloy scattering in ternary III-V compounds," *Physical Review B,* vol. 13, no. 12, p. 5347, 1976.
[78] M. A. Littlejohn, J. R. Hauser, T. H. Glisson, D. K. Ferry, and J. W. Harrison, "Alloy scattering and high field transport in ternary and quaternary III–V semiconductors," (in English), *Solid-State Electronics,* vol. 21, no. 1, pp. 107-114, 1978, doi: Doi 10.1016/0038-1101(78)90123-5.
[79] S. Lee *et al.*, "Investigation of carrier localization in InAs/AlSb type-II superlattice material system," *Applied Physics Letters,* vol. 115, no. 21, p. 211601, 2019.
[80] Y. P. Varshni, "Temperature dependence of the energy gap in semiconductors," *Physica,* vol. 34, no. 1, pp. 149-154, 1967.
[81] I. Vurgaftman, J. R. Meyer, and L. R. Ram-Mohan, "Band parameters for III–V compound semiconductors and their alloys," *Journal of Applied Physics,* vol. 89, no. 11, pp. 5815-5875, 2001.
[82] M. Cardona and M. L. W. Thewalt, "Isotope effects on the optical spectra of semiconductors," *Reviews of Modern Physics,* vol. 77, no. 4, p. 1173, 2005.
[83] Y. Zhang, Z. Wang, J. Xi, and J. Yang, "Temperature-dependent band gaps in several semiconductors: From the role of electron–phonon renormalization," *Journal of Physics: Condensed Matter,* vol. 32, no. 47, p. 475503, 2020.
[84] L. Cheng *et al.*, "Multiple-quantum-well perovskites for high-performance light-emitting diodes," *Advanced Materials,* vol. 32, no. 15, p. 1904163, 2020.
[85] R. B. Laghumavarapu *et al.*, "GaSb/InGaAs quantum dot–well hybrid structure active regions in solar cells," *Solar Energy Materials and Solar Cells,* vol. 114, pp. 165-171, 2013.
[86] N. D. Foster, A. K. Rockwell, J. A. McArthur, B. S. Mendoza, S. R. Bank, and M. C. Downer, "A Study of second-order susceptibility in digital alloy-grown InAs/AlSb multiple quantum wells," *Advanced Optical Materials,* vol. 10, no. 15, p. 2102845, 2022.
[87] A. K. Rockwell *et al.*, "Toward deterministic construction of low noise avalanche photodetector materials," *Applied Physics Letters,* vol. 113, no. 10, p. 102106, 2018.
[88] S. Adachi, "Optical dispersion relations for GaP, GaAs, GaSb, InP, InAs, InSb, $Al_x Ga_{1-x}As$, and $In_{1-x}Ga_xAs_yP_{1-y}$," *Journal of Applied Physics,* vol. 66, no. 12, pp. 6030-6040, 1989.
[89] Y. Tan, M. Povolotskyi, T. Kubis, T. B. Boykin, and G. Klimeck, "Transferable tight-binding model for strained group IV and III-V materials and heterostructures," *Physical Review B,* vol. 94, no. 4, p. 045311, 2016.
[90] Y. P. Tan, M. Povolotskyi, T. Kubis, T. B. Boykin, and G. Klimeck, "Tight-binding analysis of Si and GaAs ultrathin bodies with subatomic wave-function resolution," *Physical Review B,* vol. 92, no. 8, p. 085301, 2015.
[91] J. Heyd, G. E. Scuseria, and M. Ernzerhof, "Hybrid functionals based on a screened Coulomb potential," *The Journal of Chemical Physics,* vol. 118, no. 18, pp. 8207-8215, 2003.
[92] S. Z. Ahmed, Y. Tan, D. S. Truesdell, B. H. Calhoun, and A. W. Ghosh, "Modeling tunnel field effect transistors—From interface chemistry to non-idealities to circuit level performance," *Journal of Applied Physics,* vol. 124, no. 15, p. 154503, 2018.

[93] B. Guo *et al.*, "Temperature dependence of avalanche breakdown of AlGaAsSb and AlInAsSb avalanche photodiodes," *Journal of Lightwave Technology,* vol. 40, no. 17, pp. 5934-5942, 2022.
[94] M. Nada, Y. Muramoto, H. Yokoyama, T. Ishibashi, and H. Matsuzaki, "Triple-mesa avalanche photodiode with inverted P-down structure for reliability and stability," *Journal of Lightwave Technology,* vol. 32, no. 8, pp. 1543-1548, 2014, doi: 10.1109/jlt.2014.2308512.
[95] M. Nada, H. Yokoyama, Y. Muramoto, T. Ishibashi, and H. Matsuzaki, "50-Gbit/s vertical illumination avalanche photodiode for 400-Gbit/s Ethernet systems," *Optics Express,* vol. 22, no. 12, pp. 14681-7, Jun 16 2014, doi: 10.1364/OE.22.014681.
[96] M. Nada, T. Yoshimatsu, Y. Muramoto, H. Yokoyama, and H. Matsuzaki, "Design and performance of high-speed avalanche photodiodes for 100-Gb/s systems and beyond," *Journal of Lightwave Technology,* vol. 33, no. 5, pp. 984-990, 2015, doi: 10.1109/jlt.2014.2377034.
[97] M. Nada, T. Yoshimatsu, F. Nakajima, K. Sano, and H. Matsuzaki, "A 42-GHz bandwidth avalanche photodiodes based on III-V compounds for 106-Gbit/s PAM4 applications," *Journal of Lightwave Technology,* vol. 37, no. 2, pp. 260-265, 2019, doi: 10.1109/jlt.2018.2871508.
[98] A. Beling, X. Xie, and J. C. Campbell, "High-power, high-linearity photodiodes," *Optica,* vol. 3, no. 3, pp. 328-338, 2016.
[99] F. Yu *et al.*, "High-power high-speed MUTC waveguide photodiodes integrated on Si_3N_4/Si platform using micro-transfer printing," *IEEE Journal of Selected Topics in Quantum Electronics,* vol. 29, no. 3: Photon. Elec. Co-Inte. and Adv. Trans. Print., pp. 1-6, 2022.
[100] D. S. G. Ong, J. S. Ng, Y. L. Goh, C. H. Tan, S. Zhang, and J. P. R. David, "InAlAs avalanche photodiode with type-II superlattice absorber for detection beyond 2 μm," *IEEE Transactions on Electron Devices,* vol. 58, no. 2, pp. 486-489, 2011.
[101] B. Guo *et al.*, "InGaAs/AlInAsSb avalanche photodiodes with low noise and strong temperature stability," *APL Photonics,* vol. 8, no. 11, p. 116112, 2023.
[102] A. N. Semenov, V. A. Solov'Ev, B. Y. Meltser, Y. V. Terent'ev, L. G. Prokopova, and S. V. Ivanov, "Molecular beam epitaxy of AlInAsSb alloys near the miscibility gap boundary," *Journal of Crystal Growth,* vol. 278, no. 1-4, pp. 203-208, 2005.
[103] Y. Kang *et al.*, "Monolithic germanium/silicon avalanche photodiodes with 340 GHz gain–bandwidth product," *Nature Photonics,* vol. 3, no. 1, pp. 59-63, 2009.
[104] N. Susa, H. Nakagome, O. Mikami, H. Ando, and H. Kanbe, "New InGaAs/InP avalanche photodiode structure for the 1-1.6 μm wavelength region," *IEEE Journal of Quantum Electronics,* vol. 16, no. 8, pp. 864-870, 1980.
[105] C. Lenox *et al.*, "Resonant-cavity InGaAs-InAlAs avalanche photodiodes with gain-bandwidth product of 290 GHz," *IEEE Photonics Technology Letters,* vol. 11, no. 9, pp. 1162-1164, 1999.
[106] Y. Yuan *et al.*, "III-V on silicon avalanche photodiodes by heteroepitaxy," *Optics Letters,* vol. 44, no. 14, pp. 3538-3541, Jul 15 2019.
[107] B. Guo *et al.*, "Impact ionization coefficients of digital alloy and random alloy $Al_{0.85}Ga_{0.15}As_{0.56}Sb_{0.44}$ in a wide electric field range," *Journal of Lightwave Technology,* vol. 40, no. 14, pp. 4758-4764, 2022.

[108] D. S. Ong, K. Li, G. J. Rees, J. P. R. David, and P. N. Robson, "A simple model to determine multiplication and noise in avalanche photodiodes," *Journal of Applied Physics,* vol. 83, no. 6, pp. 3426-3428, 1998.
[109] B. Guo *et al.*, "Digital Alloy-Grown InAs/GaAs Short-Period Superlattices with Tunable Band Gaps for Short-Wavelength Infrared Photodetection," *ACS Photonics,* vol. 11, no. 4, pp. 1419-1427, 2024/04/17 2024.
[110] C. Xiang *et al.*, "High-performance silicon photonics using heterogeneous integration," *IEEE Journal of Selected Topics in Quantum Electronics,* vol. 28, no. 3: Hybrid Integration for Silicon Photonics, pp. 1-15, 2021.
[111] D. Huang *et al.*, "High-power sub-kHz linewidth lasers fully integrated on silicon," *Optica,* vol. 6, no. 6, pp. 745-752, 2019.
[112] A. Y. Liu, R. W. Herrick, O. Ueda, P. M. Petroff, A. C. Gossard, and J. E. Bowers, "Reliability of InAs/GaAs quantum dot lasers epitaxially grown on silicon," *IEEE Journal of Selected Topics in Quantum Electronics,* vol. 21, no. 6, pp. 690-697, 2015.
[113] J. Sun, R. Kumar, M. Sakib, J. B. Driscoll, H. Jayatilleka, and H. Rong, "A 128 Gb/s PAM4 silicon microring modulator with integrated thermo-optic resonance tuning," *Journal of Lightwave Technology,* vol. 37, no. 1, pp. 110-115, 2018.
[114] L. Chen, Q. Xu, M. G. Wood, and R. M. Reano, "Hybrid silicon and lithium niobate electro-optical ring modulator," *Optica,* vol. 1, no. 2, pp. 112-118, 2014.
[115] K. Sun *et al.*, "Low dark current III–V on silicon photodiodes by heteroepitaxy," *Optics express,* vol. 26, no. 10, pp. 13605-13613, 2018.
[116] M. J. Heck, J. F. Bauters, M. L. Davenport, D. T. Spencer, and J. E. Bowers, "Ultra-low loss waveguide platform and its integration with silicon photonics," *Laser & Photonics Reviews,* vol. 8, no. 5, pp. 667-686, 2014.
[117] F. Xia, L. Sekaric, and Y. Vlasov, "Ultracompact optical buffers on a silicon chip," *Nature photonics,* vol. 1, no. 1, pp. 65-71, 2007.
[118] D. Dai and J. E. Bowers, "Silicon-based on-chip multiplexing technologies and devices for Peta-bit optical interconnects," *Nanophotonics,* vol. 3, no. 4-5, pp. 283-311, 2014.

List of Publications

Journals

[J1] **B. Guo**, B. Liang, J. Zheng, S. Ahmed, S. Krishna, A. W. Ghosh, and J. C. Campbell, "Digital alloy-grown InAs/GaAs short-period superlattices with tunable bandgaps for short-wavelength infrared photodetection," ***ACS Photonics*** 11, 1419-1427 (2024).

[J2] **B. Guo,** M. Schwartz, S. H. Kodati, K. M. McNicholas, H. Jung, S. Lee, J. Konowitch, D. Chen, J. Bai, X. Guo, T. J. Ronningen, C. H. Grein, J. C. Campbell, and S. Krishna, "InGaAs/AlInAsSb avalanche photodiodes with low noise and strong temperature stability," ***APL Photonics*** 8, 116112 (2023).

[J3] **B. Guo**, S. Z. Ahmed, X. Xue, A. K. Rockwell, J. Ha, S. Lee, B. Liang, A. H. Jones, J. A. McArthur, S. H. Kodati, T. J. Ronningen, S. Krishna, J. S. Kim, S. R. Bank, A. W. Ghosh, and J. C. Campbell, "Temperature dependence of avalanche breakdown of AlGaAsSb and AlInAsSb avalanche photodiodes," ***Journal of Lightwave Technology*** 40, 5934-5942 (2022).

[J4] **B. Guo**, X. Jin, S. Lee, S. Z. Ahmed, A. H. Jones, X. Xue, B. Liang, H. I. J. Lewis, S. H. Kodati, D. Chen, T. J. Ronningen, C. H. Grein, A. W. Ghosh, S. Krishna, J. P. R. David, and J. C. Campbell, "Impact ionization coefficients of digital alloy and random alloy $Al_{0.85}Ga_{0.15}As_{0.56}Sb_{0.44}$ in a wide electric field range," ***Journal of Lightwave Technology*** 40, 4758-4764 (2022).

[J5] **B. Guo**, A. H. Jones, S. Lee, S. H. Kodati, B. Liang, X. Xue, N. A. Pfiester, M. Schwartz, M. Winslow, C. H. Grein, T. J. Ronningen, S. Krishna, and J. C. Campbell, "Optical constants of $Al_{0.85}Ga_{0.15}As_{0.56}Sb_{0.44}$ and $Al_{0.79}In_{0.21}As_{0.74}Sb_{0.26}$," ***Applied Physics Letters*** 119, 171109 (2021).

[J6] S. Lee, **B. Guo**, S. H. Kodati, H. Jung, M. Schwartz, A. H. Jones, M. Winslow, C. Grein, T. J. Ronningen, J. C. Campbell, and S. Krishna, "Random alloy thick AlGaAsSb avalanche photodiodes on InP substrates," ***Applied Physics Letters*** 120, 071101 (2022).

[J7] S. Lee, S. H. Kodati, **B. Guo**, A. H. Jones, M. Schwartz, M. Winslow, C. H. Grein, T. J. Ronningen, J. C. Campbell, and S. Krishna, "Low noise $Al_{0.85}Ga_{0.15}As_{0.56}Sb_{0.44}$ avalanche photodiodes on InP substrates," ***Applied Physics Letters*** 118, 081106 (2021).

[J8] S. H. Kodati, S. Lee, **B. Guo**, A. H. Jones, M. Schwartz, M. Winslow, N. A. Pfiester, C. H. Grein, T. J. Ronningen, J. C. Campbell, and S. Krishna, "AlInAsSb avalanche photodiodes on InP substrates," ***Applied Physics Letters*** 118, 091101 (2021).

[J9] H. I. J. Lewis, X. Jin, **B. Guo**, S. Lee, H. Jung, S. H. Kodati, B. Liang, S. Krishna, D. S. Ong, J. C. Campbell, and J. P. R. David, "Anomalous excess noise behavior in thick $Al_{0.85}Ga_{0.15}As_{0.56}Sb_{0.44}$ avalanche photodiodes," ***Scientific Reports*** 13, 9936 (2023).

[J10] Y. Peng, K. Sun, Y. Shen, **B. Guo**, A. Beling, and J. C. Campbell, "High-gain Ka-band analog photonic link using high-power photodiode at 1064 nm," ***Journal of Lightwave Technology*** 39, 1724-1732 (2021).

[J11] S. Lee, X. Jin, H. Jung, H. Lewis, Y. Liu, **B. Guo**, S. H. Kodati, M. Schwartz, C. Grein, T. J. Ronningen, J. P. R. David, J. C. Campbell, and S. Krishna, "High gain, low noise 1550 nm GaAsSb/AlGaAsSb avalanche photodiodes," ***Optica*** 10, 147-154 (2023).

[J12] D. Chen, S. D. March, A. H. Jones, Y. Shen, A. A. Dadey, K. Sun, J. A. McArthur, A. M. Skipper, X. Xue, **B. Guo**, J. Bai, S. R. Bank, and J. C. Campbell, "Photon trapping enhanced avalanche photodiodes for mid-infrared applications" ***Nature Photonics*** 17, 594-600 (2023).

[J13] X. Guo, L. Shao, L. He, K. Luke, J. Morgan, K. Sun, J. Gao, T. Tzu, Y. Shen, D. Chen, **B. Guo**, F. Yu, Q. Yu, M. Jafari, M. Lončar, M. Zhang, and A. Beling, "High-performance modified uni-traveling carrier photodiode integrated on a thin-film lithium niobate platform," ***Photonics Research*** 10, 1338-1343 (2022).

[J14] T. Ronningen, S. Kodati, X. Jin, S. Lee, H. Jung, X. Tao, H. Lewis, M. Schwartz, N. Gajowski, P. Martyniuk, **B. Guo**, A. H. Jones, J. C. Campbell, C. H. Grein, J. P. R. David, and S. Krishna, "Ionization coefficients and excess noise characteristics of AlInAsSb on an InP substrate," ***Applied Physics Letters*** 123, 13110 (2023).

[J15] J. Bai, Y. Shen, P. Yao, D. Chen, M. Konkol, **B. Guo**, X. Guo, V. Carey, J. C. Campbell, and D. Prather, "Thermal dissipation enhancement in flip-chip bonded uni-traveling carrier photodiodes," ***Optics Letters*** 48, 5157-5160 (2023).

[J16] S. Krishna, S. Lee, S. H. Kodati, M. Schwartz, H. Jung, T. J. Ronningen, **B. Guo**, A. H. Jones, M. Winslow, J. C. Campbell, and C. H. Grein, "Linear mode avalanche photodiodes with antimonide multipliers on InP substrates," ***IEEE Journal of Quantum Electronics*** 58, 4500207 (2022).

[J17] D. Chen, K. Sun, Y. Shen, A. H. Jones, A. A. Dadey, **B. Guo**, J. A. McArthur, S. R. Bank, and J. C. Campbell, "Frequency behavior of AlInAsSb nBn photodetectors and the development of an equivalent circuit model," ***Optics Express*** 30, 25262-25276 (2022).

Conferences

[C1] **B. Guo**, B. Liang, S. Z. Ahmed, S. Krishna, and J. C. Campbell, "Optical constants of digital alloy InGaAs," in ***Physics and Simulation of Optoelectronic Devices XXXII***, (SPIE, 2024), 75-78.

[C2] **B. Guo**, M. Schwartz, S. H. Kodati, K. M. McNicholas, H. Jung, S. Lee, J. Konowitch, D. Chen, J. Bai, X. Guo, T. J. Ronningen, C. H. Grein, J. C. Campbell, and S. Krishna, "Low-noise InGaAs/AlInAsSb avalanche photodiodes on InP substrates," in ***2023 IEEE Photonics Conference (IPC)***, (IEEE, 2023), 1-2.

[C3] J. Bai, Y. Shen, P. Yao, D. Chen, M. Konkol, X. Guo, **B. Guo**, V. Carey, J. C. Campbell, and D. Prather, "Improvement of thermal dissipation of high-power photodiodes," in ***2023 IEEE Photonics Conference (IPC)***, (IEEE, 2023), 1-2.

[C4] Y. Liu, X. Jin, S. Lee, H. Jung, H. Lewis, **B. Guo**, S. Kodati, M. Schwartz, C. H. Grein, T. J. Ronningen, J. C. Campbell, S. Krishna, and J. David, "Very high gain and low noise GaAsSb/AlGaAsSb avalanche photodiodes for 1550nm detection at room temperature," in ***Optical Components and Materials XXI***, (SPIE, 2024), 135-142.

[C5] X. Jin, **B. Guo**, H. I. J. Lewis, S. Lee, B. Liang, S. Krishna, J. C. Campbell, and J. P. R. David, "Excess noise measurements in $Al_{0.85}Ga_{0.15}As_{0.56}Sb_{0.44}$ avalanche photodiodes," in ***Optical Sensing and Detection VII***, (SPIE, 2022), 59-66.

[C6] J. P. R. David, X. Jin, **B. Guo**, S. Lee, H. I. J. Lewis, H. Jung, S. H. Kodati, and J. C. Campbell, "Avalanche multiplication and excess noise characteristics in antimony-based avalanche photodiodes," in ***Emerging Imaging and Sensing Technologies for Security and Defence VII***, (SPIE, 2022), 54-65.

[C7] H. Jung, S. Lee, M. Schwartz, **B. Guo**, C. H. Grein, J. C. Campbell, and S. Krishna, "Growth and characterization of InGaAs/GaAsSb type II superlattice absorbers for 2 μm avalanche photodiodes," in ***Infrared Technology and Applications XLVIII***, (SPIE, 2022), 96-104.

[C8] S. Lee, S. H. Kodati, **B. Guo**, A. H. Jones, M. Schwartz, H. Jung, N. Pfiester, M. Winslow, C. H. Grein, T. J. Ronningen, J. C. Campbell, and S. Krishna, "Thick

$Al_{0.85}Ga_{0.15}As_{0.56}Sb_{0.44}$ avalanche photodiodes on InP substrate," in ***Infrared Technology and Applications XLVII***, (SPIE, 2021), 9-18.

[C9] S. H. Kodati, S. Lee, **B. Guo**, A. H. Jones, M. Schwartz, M. Winslow, N. A. Pfiester, C. Grein, T. J. Ronningen, J. C. Campbell, and S. Krishna, "Low noise AlInAsSb avalanche photodiodes on InP substrates for 1.55 μm infrared applications," in ***Infrared Technology and Applications XLVII***, (SPIE, 2021), 382-389.

[C10] R. H. El-Jaroudi, A. A. Dadey, X. Xue, A. H. Jones, **B. Guo**, J. C. Campbell, and S. R. Bank, "Reducing III-V avalanche photodiode noise through the introduction of boron," in ***Device Research Conference***, (IEEE, 2021).